



Delft University of Technology

Nanophotonics with Diamond Color Centers Quantum Optics and Entanglement Protocols

Pasini, M.

DOI

[10.4233/uuid:9a88bb0a-a1d8-4291-ac3d-040201a743ab](https://doi.org/10.4233/uuid:9a88bb0a-a1d8-4291-ac3d-040201a743ab)

Publication date

2024

Document Version

Final published version

Citation (APA)

Pasini, M. (2024). *Nanophotonics with Diamond Color Centers: Quantum Optics and Entanglement Protocols*. [Dissertation (TU Delft), Delft University of Technology]. <https://doi.org/10.4233/uuid:9a88bb0a-a1d8-4291-ac3d-040201a743ab>

Important note

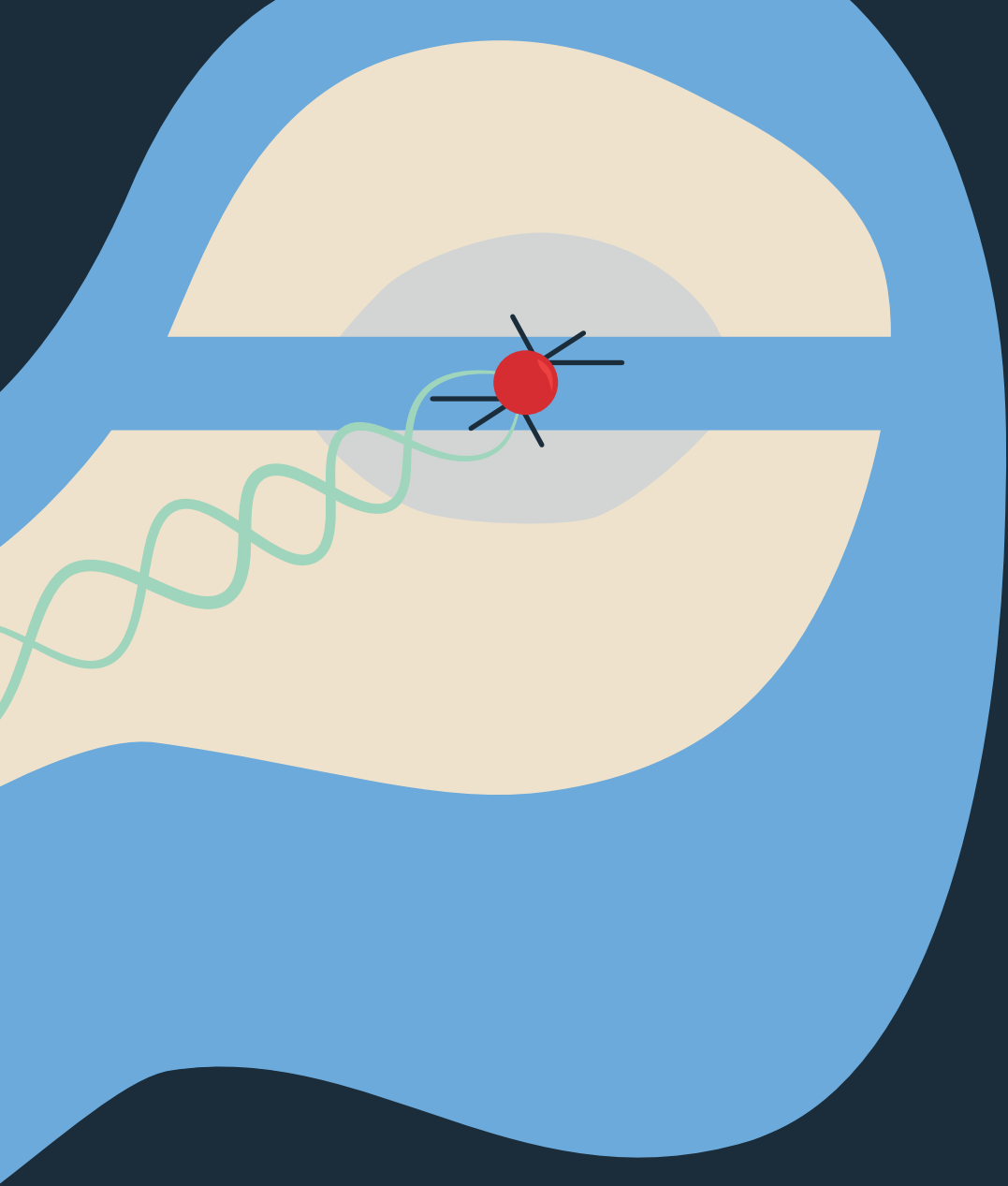
To cite this publication, please use the final published version (if applicable).
Please check the document version above.

Copyright

Other than for strictly personal use, it is not permitted to download, forward or distribute the text or part of it, without the consent of the author(s) and/or copyright holder(s), unless the work is under an open content license such as Creative Commons.

Takedown policy

Please contact us and provide details if you believe this document breaches copyrights.
We will remove access to the work immediately and investigate your claim.



NANOPHOTONICS WITH DIAMOND COLOR CENTERS
QUANTUM OPTICS AND ENTANGLEMENT PROTOCOLS

*M*ATTEO PASINI

NANOPHOTONICS WITH DIAMOND COLOR CENTERS
QUANTUM OPTICS AND ENTANGLEMENT PROTOCOLS

Dissertation

for the purpose of obtaining the degree of doctor
at Delft University of Technology,
by the authority of the Rector Magnificus, Prof. dr. ir. T.H.J.J. van der Hagen,
Chair of the Board for Doctorates,
to be defended publicly on
Friday May 17th 2024 at 10:00 o'clock

by

Matteo PASINI

Master of Science in Physics,
Università di Trento, Italy,
born in Lugo, Italy.

This dissertation has been approved by the promotor.

Composition of the doctoral committee:

Rector Magnificus
Prof. dr. ir. R. Hanson
Dr. C. Errando-Herranz

Chairperson
Delft University of Technology, Promotor
Delft University of Technology, Copromotor

Independent members:

Prof. dr. T. Schröder
Prof. dr. Y. Chu
Dr. M. Blaauboer
Prof. dr. L. Kuipers
Prof. dr. A. F. Otte

Humboldt University of Berlin, Germany
ETH Zürich, Switzerland
Delft University of Technology
Delft University of Technology
Delft University of Technology, Reserve member



Copyright © 2024 by Matteo Pasini
Printed by: Gildeprint - Enschede

Cover design: Matteo Pasini

ISBN 978-94-6384-579-3

An electronic version of this dissertation is available at
<http://repository.tudelft.nl/>.

CONTENTS

| | |
|--|------------|
| Summary | vii |
| Samenvatting | ix |
| 1 Introduction | 1 |
| 1.1 Spin, Meet Photon. Photon, Meet Spin | 2 |
| 1.2 Browsing The Quantum Internet | 4 |
| 1.3 Diamonds Are Quantum's Best Friend. | 5 |
| 1.4 Thesis Overview. | 7 |
| Bibliography | 8 |
| 2 Spin-Photon Interface with Color Centers in Diamond | 11 |
| 2.1 Spin-Photon Interfaces in Diamond | 12 |
| 2.1.1 Spin-Photon Interfaces for Entanglement Generation | 12 |
| 2.1.2 The NV, State of the Art. | 14 |
| 2.1.3 Group-IV Vacancy centers | 14 |
| 2.2 The Tin-Vacancy center | 16 |
| 2.2.1 The Defect | 16 |
| 2.2.2 Spin-Photon Interface | 17 |
| 2.2.3 Phonons | 21 |
| 2.2.4 Strain | 23 |
| 2.2.5 Prospects and Trade-offs. | 25 |
| 2.3 Waveguide and Cavity QED with Group-IV Centers | 26 |
| 2.3.1 Nanophotonic Integration in Diamond | 26 |
| 2.3.2 Cavity QED with Group-IV centers. | 27 |
| 2.3.3 Waveguide QED with Group-IV centers | 30 |
| Bibliography | 33 |
| 3 From Bulk Diamond to SnVs in Waveguides | 39 |
| 3.1 Sample: SnV Fabrication | 40 |
| 3.1.1 High Energy Implantation | 41 |
| 3.1.2 Shallow Ion Implantation and Growth | 42 |
| 3.1.3 Challenges for SnV Generation. | 42 |
| 3.2 Fingerprint: SnV Optical Characterisation | 43 |
| 3.2.1 SnV in the Crystal | 43 |
| 3.2.2 Spectrum and Inhomogeneous Distribution | 44 |
| 3.2.3 Single SnV Optical Fingerprint | 46 |
| 3.2.4 Phonon Induced Linewidth Broadening | 47 |
| 3.2.5 Stability and Repumping Methods | 48 |

| | | |
|----------|--|-----------|
| 3.3 | Integration: SnV in Waveguides | 50 |
| 3.3.1 | Effects of Waveguide-QED | 50 |
| 3.3.2 | SnV-Waveguide Coupling | 53 |
| 3.3.3 | Setup and Fiber Coupling | 54 |
| 3.3.4 | Characterisation of SnV in Waveguides | 56 |
| 3.4 | Conclusions. | 57 |
| | Bibliography | 58 |
| 4 | Nonlinear Quantum Photonics with a SnV Center in a Waveguide | 61 |
| 4.1 | Introduction | 62 |
| 4.2 | Device and Experiment | 63 |
| 4.3 | Optical Transition Stability | 64 |
| 4.4 | Spectroscopy of the Waveguide-SnV System | 64 |
| 4.5 | Photon Statistics of Transmitted Field. | 66 |
| 4.6 | Reflected Signal and Photon Statistics. | 69 |
| 4.7 | Conclusions. | 70 |
| 4.8 | Methods | 70 |
| 4.8.a | Sample and device fabrication | 70 |
| 4.8.b | Measurement sequences. | 72 |
| 4.8.c | Lifetime measurement from resonant $g^{(2)}_{pp}(\tau)$ | 73 |
| 4.8.d | Input Polarization | 74 |
| 4.8.e | Simulations of SnV-Waveguide coupling | 75 |
| 4.8.f | Theoretical models. | 76 |
| | Bibliography | 79 |
| 5 | Remote-Entanglement Protocols for Qubits with Photonic Interfaces | 83 |
| 5.1 | Introduction | 84 |
| 5.2 | Remote-entanglement-protocol framework | 85 |
| 5.3 | Logical Building Blocks and Topology. | 88 |
| 5.3.1 | Topology of the protocol | 88 |
| 5.3.2 | Spin-Photon-Interface blocks | 90 |
| 5.3.3 | Photon blocks | 92 |
| 5.3.4 | Spin blocks. | 93 |
| 5.3.5 | Other logical building blocks. | 93 |
| 5.3.6 | Combining topology and Logical Building Blocks | 93 |
| 5.4 | Encoding | 93 |
| 5.4.1 | Photonic encoding. | 93 |
| 5.4.2 | Spin encoding | 96 |
| 5.5 | Physical building blocks | 97 |
| 5.5.1 | Photon operations | 97 |
| 5.5.2 | Spin operations | 99 |
| 5.5.3 | Spin-photon interface | 100 |
| 5.6 | Quantum optical modeling | 105 |
| 5.6.1 | Emitter. | 105 |
| 5.6.2 | Photonic cavity | 107 |
| 5.6.3 | Quantum channel description of PBB | 110 |

| | | |
|----------|--|------------|
| 5.7 | Software implementation of the framework. | 113 |
| 5.8 | Simulating and Benchmarking Entanglement Protocols | 114 |
| 5.9 | Conclusions. | 118 |
| 5.10 | Methods | 119 |
| 5.10.a | Nomenclature | 119 |
| 5.10.b | Notation and simulation parameters | 120 |
| 5.10.c | Modeling conditional reflection spin-photon interface with uni- taries. | 121 |
| 5.10.d | Quantum Modeled Physical Parameters | 122 |
| 5.10.e | Simulations parameter sweep and details | 123 |
| | Bibliography | 123 |
| 6 | Conclusions and Outlook | 131 |
| 6.1 | Summary | 132 |
| 6.2 | Hardware: SnV Centers in Diamond | 132 |
| 6.2.1 | The Open Challenges | 133 |
| 6.2.2 | The Opportunities | 134 |
| 6.3 | An Integrated Spin-Photon Interface | 135 |
| 6.3.1 | Challenges and Prospects for Diamond Nanophotonics | 135 |
| 6.3.2 | Hybrid Photonic Integration | 136 |
| 6.3.3 | Cavity or Waveguide-Based Quantum Nodes | 137 |
| 6.4 | Find the Best Entanglement Protocol | 138 |
| 6.4.1 | Comparing Protocols | 138 |
| 6.5 | Conclusions. | 139 |
| | Bibliography | 140 |
| | Acknowledgements | 145 |
| | List of Publications | 151 |
| | Curriculum Vitae | 153 |



SUMMARY

A large-scale quantum network, where many nodes are connected via entanglement and can share and process quantum information, will allow applications that are now unattainable. While some are known, ranging from distributed quantum computing to enhanced quantum sensing and quantum communication, the full potential of such a fundamentally new technology is yet to be discovered. Color centers in diamond, with their excellent optical properties, long spin coherence times, and versatile control over local nuclear spins, are a leading platform for building quantum network nodes and recently allowed crucial proof-of-principle experiments. Going beyond experiments and towards a large and functional network requires faster entanglement generation and a scalable architecture. Integration of color centers in nanophotonic structures paves the way to solving these challenges, enhancing the interface between the spins and photons that carry quantum information across the network. Furthermore, combining diamond nanophotonic devices with integrated photonic and electronic circuits is a promising way to realize a large-scale quantum system. This thesis is about integrated spin-photon interfaces in diamonds and how to generate entanglement between them and includes experimental and theoretical results toward this goal.

First, we introduce the Group-IV color centers in diamond, which thanks to their symmetry properties are robust against electric field noise and compatible with integration in nano-scale structures. Focusing on the tin-vacancy (SnV) center, we discuss the main features and effects that play a role in its use as a spin-photon interface. We then present experimental results going from the fabrication and characterization of bulk diamond samples with SnV centers to the integration in nanophotonic waveguides, where we show stable and coherent optical lines and measure the extinction of the transmission signal caused by a single SnV center with contrast up to 35%.

Then, we investigate the interaction between a single SnV center and a weak coherent light field in a single-mode waveguide. We perform spectroscopy of the transmitted and reflected signals, and demonstrate the single-photon nature of the interaction by measuring the effect on the photon statistics in both fields.

Finally, we introduce a theoretical framework for photon-mediated entanglement generation protocols between spin-based quantum systems. This allows us to understand, categorize, and construct entanglement protocols in terms of abstract building blocks, that can be combined with hardware modeling for a more detailed description of the protocols. To showcase the framework, we analyze three different entanglement protocols, considering silicon-vacancy (SiV) centers coupled to photonic crystal cavities as the hardware, and we quantitatively compare them using a software package built to match the structure of the framework.



SAMENVATTING

Een grootschalig kwantumnetwerk waarin vele knooppunten via verstrengeling verbonden zijn en kwantuminformatie met elkaar kunnen delen en verwerken, zal toepassingen mogelijk maken die tot op heden onhaalbaar zijn. Hoewel sommige al bekend zijn, van gedistribueerde kwantumberekeningen tot verbeterde kwantumsensoren en kwantumcommunicatie, moet het volledige potentieel van zo'n fundamenteel nieuwe technologie nog ontdekt worden. 'Kleurencentra' in diamant, met hun uitstekende optische eigenschappen, lange spincoherentietijden en veelzijdige controle over lokale atoomkernspins, zijn een toonaangevend platform voor het bouwen van kwantumnetwerkknooppunten en hebben onlangs cruciale 'proof-of-principle' experimenten mogelijk gemaakt. Om verder te gaan dan experimenten en een groot en functioneel netwerk te bouwen, zijn een versnelling in het genereren van verstrengeling en een schaalbare architectuur nodig. Integratie van 'kleurencentra' in nanofotonische structuren baant de weg hiernaartoe, door het verbeteren van de 'interface' tussen spins en de fotonen die de kwantuminformatie over het netwerk transporteren. Verder is het combineren van nanofotonische diamantstructuren met fotonische en elektronische geïntegreerde schakelingen een veelbelovende manier om een grootschalig kwantumsysteem te realiseren. Dit proefschrift gaat over geïntegreerde spin-foton-interfaces in diamant en hoe daartussen verstrengeling te genereren, en omvat experimentele en theoretische resultaten om dit doel te bereiken.

Allereerst introduceren we groep-IV 'kleurencentra' in diamant, die dankzij hun symmetrieën bestand zijn tegen elektromagnetische veldruis en compatibel zijn met integratie in nanostructuren. We focussen op het 'tin-holte-centrum' (SnV-centrum) en bespreken de belangrijkste eigenschappen en effecten die een rol spelen bij het gebruik daarvan als spin-foton-interface. Daarna presenteren we experimentele resultaten, van fabricage en karakterisering van SnV-centra in bulk diamantmonsters tot de integratie in nanofotonische golfgeleiders, waarin we stabiele en coherente optische lijnen laten zien en we tot 35 procent uitdoving van het doorgelaten licht meten, veroorzaakt door een enkel aanwezig SnV-centrum.

Vervolgens onderzoeken we de interactie tussen een enkel SnV-centrum en een zwak coherent lichtveld in een golfgeleider die maar één modus toelaat. We voeren spectroscopie uit van de doorgelaten en gereflecteerde signalen, en tonen de enkelfotonische aard van de interactie aan door het effect ervan op de fotonstatistieken van beide signalen te meten.

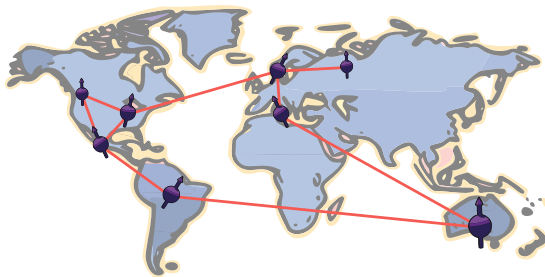
Tot slot introduceren we een theoretisch kader voor protocollen die via fotonen verstrengeling genereren tussen op spin gebaseerde kwantumsystemen. Dit maakt het mogelijk om verstrengelingsprotocollen te begrijpen, te categoriseren en te construeren in ter-

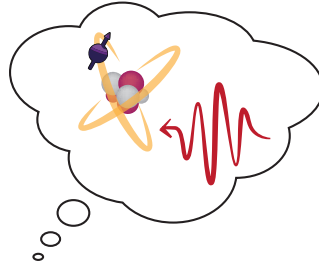
men van abstracte bouwstenen, die gekoppeld kunnen worden aan hardwaremodellen voor een gedetailleerdere beschrijving van die protocollen. Om een beeld te geven van de werking van dit kader, beschouwen we drie verschillende verstrengelingsprotocollen, met silicium-holte-centra (SiV-centra) gekoppeld aan fotonische kristalresonators als hardware, en vergelijken die kwantitatief met een softwarepakket gebouwd voor de structuur van dit kader.

1

INTRODUCTION

The interaction of light and matter at the level of single photons and atoms lies at the foundations of quantum science. On the way toward a large-scale quantum network, where nodes can share and process quantum information and enable unprecedented applications, harnessing and enhancing this interaction to efficiently connect remote quantum systems is essential. A promising platform for this task is color centers in diamond.





1.1. SPIN, MEET PHOTON. PHOTON, MEET SPIN

FROM THOUGHT EXPERIMENTS TO LAB REALITY

How do light and matter interact at their most fundamental level: single photons and atoms? It is a question that served for decades as a playground for thought experiments on the basic theory of quantum physics [1]. That was, at least, until the 90s and early 2000s. At that point, researchers were able to experimentally isolate and control single atoms and photons well enough to witness their interaction and manipulate their quantum state, with groundbreaking results that were worth a Nobel prize for S. Haroche and D.J. Wineland in 2012 [2]. The study of light-matter interaction now forms the foundation of quantum optics and it is a crucial tool for developing technologies based on quantum science.

The very first experiments used cavities to measure the effect of a weak electromagnetic field on atoms, marking the birth of cavity-quantum electrodynamics [3]. More than a mere practical tool, the need for a cavity is a consequence of the elusive nature of light-matter interaction in free space. In a simple picture, if many photonic modes are available the probability that the atom reversibly interacts with a specific one is low. Our photon, prepared in that mode, is unlikely to meet the atom. Or, if it does, it will be the quick handshake of spontaneous emission before they go separate ways in the vast continuum of electromagnetic field modes. Confining light in photonic structures changes the density of photonic states available to the atom and makes the atom preferentially interact with one mode. As a result, the atomic emission can be enhanced or suppressed depending on whether we increase or decrease the available photonic modes, but most interestingly it makes it more likely that once the photon is emitted, it will re-interact with the atom, and it becomes a reversible interaction.

THE AGE OF QUANTUM INFORMATION

Around the same time, following the lead of another thought experiment, the Einstein-Podolsky-Rosen paradox [4] which introduced the idea of quantum entanglement, seminal experiments were carried on to test the foundations of quantum mechanics. In par-

ticular, the earlier experiments based on entangled photons (another Nobel prize in 2022 to A. Aspect, J. Clauser, and A. Zeilinger) not only verified the non-local nature of quantum mechanics using the inequalities formulated by John Bell [5], but also served as the starting point for a new field of physics: quantum information science. The basic idea is to use the quantum properties of elementary systems, such as the superposition principle and entanglement, to develop new ways of processing and sharing information. This is enabled by encoding information in the quantum state of the system and realizing a "qubit" (quantum-bit). Quantum information science promises to address challenges and applications that are unmanageable with classical tools, and they are commonly divided into three categories: quantum computing, quantum communication, and quantum sensing.

FLYING QUBITS

The practical requirements for making qubits were described by David DiVincenzo in five Criteria [6]. They mainly focus on quantum computation and describe what properties a *stationary qubit* platform should have to be used for quantum information processing. The stationary qubit is the elementary physical unit that can be used to build a quantum processor and should be reliable, controllable, and long-lived. However, two additional criteria introduce what is called a *flying qubit*, which allows to transfer quantum information. These two criteria require

- 7. *the ability faithfully to transmit flying qubits between specified locations*

and, most importantly for the scope of this thesis,

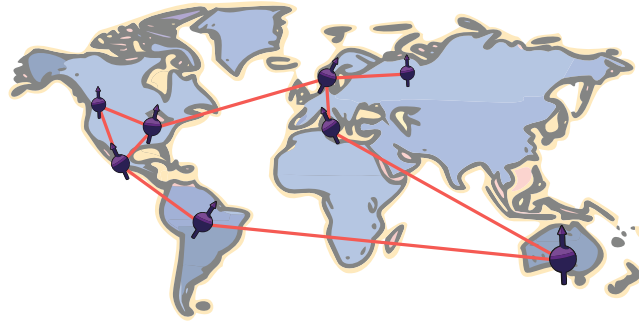
- 6. *the ability to interconvert stationary and flying qubits.*

THE SPIN-PHOTON INTERFACE

Stationary qubits can be based on several material platforms, ranging from quantum dots to trapped ions to superconducting devices, each with different advantages and challenges and often each with a better-suited target application. In this thesis, we consider qubits encoded in the spin states of a single atom or an atom-like system. This includes trapped ions and cold atoms, quantum dots, color centers, and other solid-state defects. The pool of competitors for the role of flying qubit is less crowded, and only one candidate stands out as an optimal quantum information carrier. Surprisingly (or not) it is the same used for classical information: light. Or, in the quantum realm, photons. Using photons in the optical domain as quantum information carriers allows to rely on decades-long knowledge, technology, and infrastructure that was developed for classical telecommunication. From a fundamental point of view, photons provide a flexible and reliable platform, as qubits can be encoded in different degrees of freedom, they can be converted between different frequencies which allows to interface with different stationary platforms, and they weakly interact with the surrounding meaning that they preserve well their quantum state (until they get lost!). The fact that they only weakly interact, however, makes the "interconversion" between stationary and flying qubits challenging. What we need is a way to connect the spin qubit with a photonic flying qubit: a *spin-photon interface*. An optical transition that involves the spin state used as a qubit can fulfill this task.

ENTANGLING SPINS AND PHOTONS

Here is where the concepts of entanglement and quantum information tie to the interest in the fundamental interaction between single photons and single atoms. By exploiting single photon interaction with the optical transition of an atom it is possible to entangle the quantum state of the two systems. The possibility to realize *spin-photon entanglement* is a key feature for a system to be used in quantum information.

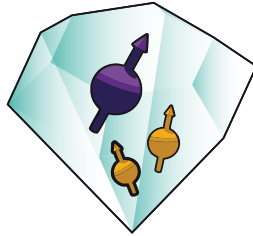


1.2. BROWSING THE QUANTUM INTERNET

Similarly to what the internet is to classical information, the vision for quantum science is to have a large-scale network that allows to transfer quantum information and connect remote quantum systems by using entanglement. A *quantum internet* [7], as we call this kind of network, would facilitate scaling up quantum computing by interconnecting smaller processors (distributed quantum computing [8]), and at the same time enable applications that are beyond the possibilities of the classical internet [9]. As for many radically new technologies, it is hard to imagine the full potential of a future full-fledged quantum network, but some applications are already being studied and proposed, such as secure communication [10] and quantum-enhanced metrology [11, 12]. To entangle the nodes of a quantum network one needs to bridge the distance between them with quantum information carriers, and as we have seen optical photons are a promising platform that. Photons, each entangled with a quantum node, can travel through optical fibers or free-space channels and be used to generate entanglement between the nodes. While optically-active stationary qubit platforms [13] are natively suited for this task, ongoing work on microwave-to-optical coherent photon conversion holds high hopes to extend this approach also to superconducting circuits and other platforms [14, 15]. Optically-mediated entanglement is not only advantageous for long-distance quantum links, where the low loss and flexibility of optical photons are unrivaled, but also interesting for locally creating connectivity between quantum processors.

Apart from entanglement generation between distant systems [16, 17], other key operations required for a quantum internet have recently been demonstrated, including a non-local quantum gate between two qubits [18], entanglement swapping [19] and unconditional teleportation [20] in a three-node network. However, the low efficiency of

state-of-the-art quantum nodes and excess photon losses when increasing the link distance have limited the results to one-kilometer distance [16], up to three nodes [19] and entanglement generation rates in the range between mHz and kHz depending on the platforms [16, 21]. Compensating for photon losses in distant links cannot be done with classical tools such as amplification or classical repeaters, as they would alter the quantum state. For this task the use of quantum repeaters [22] is necessary.



1.3. DIAMONDS ARE QUANTUM'S BEST FRIEND

Several optically active systems have been used or proposed for realizing quantum network nodes. In particular, artificial atoms in solid-state materials [23], which usually consist of point-like defects such as interstitial or substitutional impurities, offer a scalable and robust platform. Atom-like systems in solid-state materials can inherit a lot of their properties from the host [24, 25]. In the large band-gap of diamond, around 5.5eV, the electronic levels of defects can be well defined and isolated and therefore more stable, while allowing for a broad wavelength range. Additionally, its highly symmetric crystalline structure can translate to the symmetry of the defect's electronic orbitals, which is desirable as it can boost the optical properties and the stability of the system. These are among the reasons for which diamond can host excellent defects, or color centers. Diamond also has the practical advantage that it is a well studied material. Aside from the extensive knowledge of defects spectroscopy in diamond, research and industrial efforts over time have led to the commercial availability of diamond substrates with extremely low concentrations of impurities (Boron and Nitrogen concentrations of less than a few parts per billion), and good crystalline structure. In recent years, with the emergence of diamond as one of the leading quantum science platforms, further effort is being invested into improving the tools available, such as chemical vapor deposition (CVD) of high-quality diamond which is possible with controllable levels of impurities and concentration of Carbon isotopes (^{13}C), methods for doping and incorporating other atomic species. Most importantly, the scientific community has advanced significantly in the development of fabrication recipes allowing the realization of nanometer-scale features. Challenges are still present: for example the lack of heteroepitaxial growth or other methods for integrating diamond with other materials, the limited dimension of the substrates (usually few mm^2) that prevents large-scale fabrication, and the challenge of controlling the local strain and electronic

environments and their effect on the photo- and electro-physic of the color centers. Nevertheless, the maturity of diamond as a host material combined with its favorable properties holds great promise for the development of quantum devices based on solid-state defects.

The cornerstone of color centers in diamond for quantum science is the nitrogen-vacancy (NV) center [26], formed by a substitutional nitrogen and a carbon vacancy. Several key experiments and proof-of-principles for quantum science applications involving diamond, including many of the ones mentioned in the previous section, are based on the NV. However, two drawbacks of the NV affect its scalability hindering its use for large multi-node quantum networks: the optical transition used as a spin-photon interface is inefficient and very sensitive to electric field noise. Recently, a family of color centers based on a Group-IV atom (Si, Ge, Sn, Pb) and a vacancy [27] attracted a lot of attention. Color centers of this family have a more efficient spin-photon interface, and due to the high symmetry of the defect structure, they lack a permanent electric dipole and are thus more robust against electric field noise. The latter also means that these color centers can be integrated into nanophotonic structures where the proximity to the diamond surface results in significant charge noise. This paves the way to a whole new set of devices and designs, which can potentially lead to a new generation of quantum network nodes [28, 29].

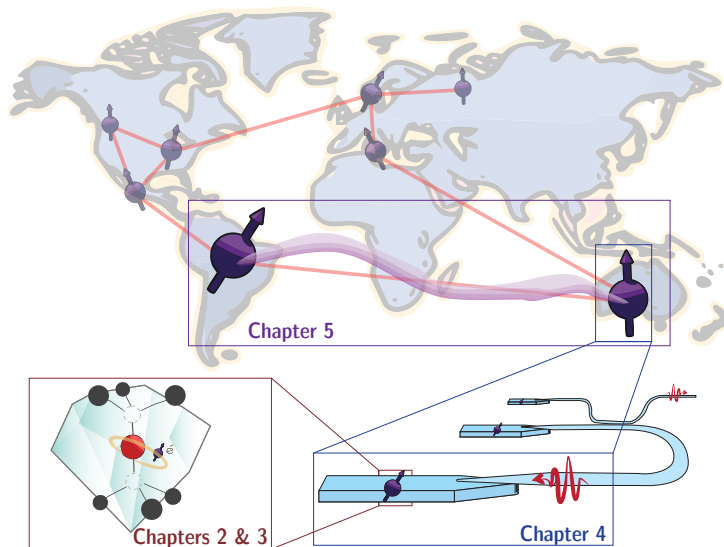


Figure 1.1: **Overview of this Thesis.**

1.4. THESIS OVERVIEW

This thesis is about spin-photon interfaces based on diamond nanophotonic devices, and how to generate entanglement between them. We go about this by combining experimental results on a promising color center, the tin-vacancy (SnV) center in diamond, and a high-level discussion on protocols for entanglement generation, which ultimately shows different approaches on how to generate entanglement with diamond-based nanophotonic devices. The thesis is organized as follows:

- In **Chapter 2** we introduce the basic concepts on the platform of interest: Group-IV Vacancy centers in diamond, in particular the tin-vacancy (SnV) center, and their implementation in Cavity- and Waveguide-QED systems.
- **Chapter 3** will focus on the fabrication of SnV centers, including measurements and characterization of the optical transition, and their integration in nanophotonic diamond waveguides.
- In **Chapter 4** we investigate the nonlinear photonic interaction between a weak coherent light field and a single SnV center in a single-mode waveguide.
- The goal of **Chapter 5** is to introduce a modular theoretical framework for understanding, categorizing, and modeling protocols for remote entanglement generation of optically-interfaced qubits. To give an example of its application, we simulate and compare the performance of different entanglement protocols based on silicon-vacancy centers in diamond nanophotonic cavities.
- Finally, in **Chapter 6** we summarize the findings of this thesis and outline the prospects for using SnV centers as the next generation of diamond-based quantum devices.

BIBLIOGRAPHY

- [1] E. Schrödinger, *Are There Quantum Jumps ?* British Journal for the Philosophy of Science **3**, 233 (1952).
- [2] I. Georgescu, *Nobel Prize 2012: Haroche & Wineland*, Nature Physics **8**, 777 (2012).
- [3] S. Haroche and D. Kleppner, *Cavity Quantum Electrodynamics*, Physics Today **42**, 24 (1989).
- [4] A. Einstein, B. Podolsky and N. Rosen, *Can Quantum-Mechanical Description of Physical Reality Be Considered Complete?* Physical Review **47**, 777 (1935).
- [5] J. S. Bell, *On the Einstein Podolsky Rosen paradox*, Physics Physique Fizika **1**, 195 (1964).
- [6] D. P. DiVincenzo, *The Physical Implementation of Quantum Computation*, Fortschritte der Physik **48**, 771 (2000).
- [7] H. J. Kimble, *The quantum internet*, Nature **453**, 1023 (2008).
- [8] N. H. Nickerson, J. F. Fitzsimons and S. C. Benjamin, *Freely Scalable Quantum Technologies Using Cells of 5-to-50 Qubits with Very Lossy and Noisy Photonic Links*, Physical Review X **4**, 041041 (2014).
- [9] S. Wehner, D. Elkouss and R. Hanson, *Quantum internet: A vision for the road ahead*, Science **362** (2018), 10.1126/science.aam9288.
- [10] A. Ekert and R. Renner, *The ultimate physical limits of privacy*, Nature **507**, 443 (2014).
- [11] D. Gottesman, T. Jennewein and S. Croke, *Longer-Baseline Telescopes Using Quantum Repeaters*, Physical Review Letters **109**, 070503 (2012).
- [12] P. Kómár *et al.*, *A quantum network of clocks*, Nature Physics **10**, 582 (2014).
- [13] D. D. Awschalom, R. Hanson, J. Wrachtrup and B. B. Zhou, *Quantum technologies with optically interfaced solid-state spins*, Nature Photonics **12**, 516 (2018).
- [14] Y. Chu and S. Gröblacher, *A perspective on hybrid quantum opto- and electromechanical systems*, Applied Physics Letters **117**, 150503 (2020).
- [15] M. Mirhosseini, A. Sipahigil, M. Kalaei and O. Painter, *Superconducting qubit to optical photon transduction*, Nature **588**, 599 (2020).
- [16] B. Hensen *et al.*, *Loophole-free Bell inequality violation using electron spins separated by 1.3 kilometres*, Nature **526**, 682 (2015).
- [17] C. M. Knaut *et al.*, *Entanglement of Nanophotonic Quantum Memory Nodes in a Telecommunication Network*, (2023), arxiv:2310.01316 [quant-ph] .

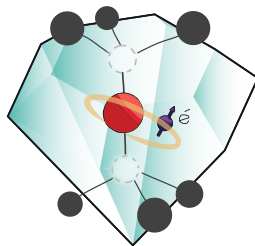
- [18] S. Daiss *et al.*, *A quantum-logic gate between distant quantum-network modules*, *Science* **371**, 614 (2021).
- [19] M. Pompili *et al.*, *Realization of a multinode quantum network of remote solid-state qubits*, *Science* **372**, 259 (2021).
- [20] S. Hermans, *Quantum Networks Using Spins in Diamond*, Ph.D. thesis, Delft University of Technology (2022).
- [21] R. Stockill *et al.*, *Phase-Tuned Entangled State Generation between Distant Spin Qubits*, *Physical Review Letters* **119**, 010503 (2017).
- [22] H.-J. Briegel, W. Dür, J. I. Cirac and P. Zoller, *Quantum Repeaters: The Role of Imperfect Local Operations in Quantum Communication*, *Physical Review Letters* **81**, 5932 (1998).
- [23] M. Atatüre, D. Englund, N. Vamivakas, S.-Y. Lee and J. Wrachtrup, *Material platforms for spin-based photonic quantum technologies*, *Nature Reviews Materials* **3**, 38 (2018).
- [24] L. C. Bassett, A. Alkauskas, A. L. Exarhos and K.-M. C. Fu, *Quantum defects by design*, *Nanophotonics* **8**, 1867 (2019).
- [25] G. Wolfowicz *et al.*, *Quantum guidelines for solid-state spin defects*, *Nature Reviews Materials* **6**, 906 (2021).
- [26] F. Jelezko and J. Wrachtrup, *Single defect centres in diamond: A review*, *physica status solidi (a)* **203**, 3207 (2006).
- [27] C. Bradac, W. Gao, J. Forneris, M. E. Trusheim and I. Aharonovich, *Quantum nanophotonics with group IV defects in diamond*, *Nature Communications* **10**, 5625 (2019).
- [28] A. Sipahigil *et al.*, *An integrated diamond nanophotonics platform for quantum-optical networks*, *Science* **354**, 847 (2016).
- [29] N. H. Wan *et al.*, *Large-scale integration of artificial atoms in hybrid photonic circuits*, *Nature* **583**, 226 (2020).



2

SPIN-PHOTON INTERFACE WITH COLOR CENTERS IN DIAMOND

Color centers in diamond have proven to be a valuable hardware platform on the way toward a practical and scalable application of quantum technologies, from networking to sensing to simulations. The family of Group-IV centers, and in particular the tin-vacancy (SnV), is a promising candidate for realizing efficient and scalable spin-photon interfaces. Here we discuss the electronic structure and the effects that play a role in the use of the SnV as a spin-photon interface. Finally, we introduce the basic concepts of cavity- and waveguide-QED with diamond color centers.



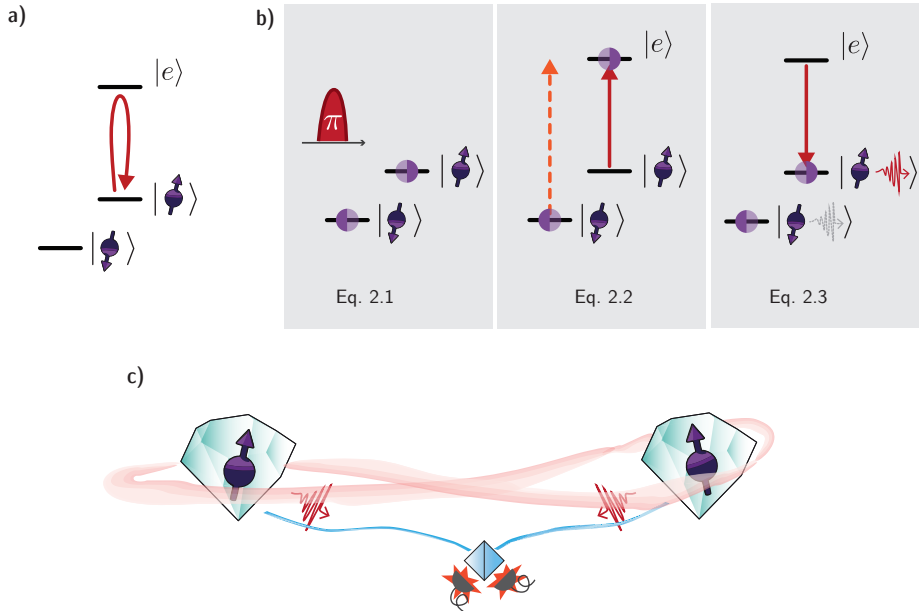


Figure 2.1: **Spin-Photon Interface** (a) Schematic of a simple spin photon interface with one spin-dependent optical transition. (b) Generating spin-photon entanglement through spin-dependent photon emission. (c) Two spin-photon entangled systems can lead to spin-spin entanglement by measuring the photons after removing the path information.

2.1. SPIN-PHOTON INTERFACES IN DIAMOND

2.1.1. SPIN-PHOTON INTERFACES FOR ENTANGLEMENT GENERATION

Using photons as a mediator to generate entanglement between solid-state qubits is an established approach [1, 2] that is necessary for long-distance entanglement links, but can be advantageous also at a smaller scale, such as entangling devices in an on-chip architecture. Solid-state systems rarely have a long-range interaction that can be scalably leveraged for this task, and photon routing allows flexible connectivity. Therefore, an enabling element for a candidate quantum node is an interface that can be used to generate entanglement between photons and a spin-based qubit. Then, entanglement between a spin and a photon can be used to generate spin-spin entanglement. Chapter 5 will discuss many ways to realize this. Here we will just give a brief basic example.

Picture a simple spin-photon interface with the level scheme in Fig. 2.1(a). We have a qubit which is encoded in two spin states of the system. One of the states is coupled to an optical transition. This level scheme can be used to entangle the spin with a photon using a spin-dependent operation on the photon state. One option is to use photon emission, with the sequence depicted in Fig. 2.1(b): we start with the spin in an equal

superposition, here s denotes the spin state and p the photon state, while $|\text{vac}\rangle_p$ is the photonic vacuum state:

$$|\psi\rangle = |\text{vac}\rangle_p \otimes \frac{1}{\sqrt{2}}(|\uparrow\rangle_s + |\downarrow\rangle_s). \quad (2.1)$$

We can drive the optical transition with an external laser pulse to excite the system to the $|e\rangle$ state, but only if it is in $|\uparrow\rangle$. The result is

$$|\text{vac}\rangle_p \otimes \frac{1}{\sqrt{2}}(|e\rangle_s + |\downarrow\rangle_s). \quad (2.2)$$

The system can then spontaneously decay from the excited state emitting a photon, and yielding the state

$$\frac{1}{\sqrt{2}}(|\uparrow\rangle_s |1\rangle_p + |\downarrow\rangle_s |\text{vac}\rangle_p), \quad (2.3)$$

where now the spin state is entangled with the photon number.

The photon number is not a very reliable way of encoding information in the photon, as loss of the photon will change the state causing an error that cannot be detected. We can choose to encode the state in some other degree of freedom of the photon, for example, a temporal mode (or *time-bin*). In this case, we send two excitation pulses delayed in time, at a *Early* and a *Late* time, applying a π rotation on the spin state in between. The resulting spin-photon entangled state will be

$$\frac{1}{\sqrt{2}}(|\downarrow\rangle_s |E\rangle_p + |\uparrow\rangle_s |L\rangle_p), \quad (2.4)$$

where there is always exactly one photon, either in the $|E\rangle$ or $|L\rangle$ state. If the photon is not detected, this will herald an error in the protocol which can be due, for example, to photon loss or an excited state decay through a different channel than the desired transition. The latter happens in solid-state emitters like color centers in diamond because they are not ideal two-level systems. De-excitation from $|e\rangle$ only happens with a photon emission in the transition of interest with a finite probability. This affects the efficiency of the spin-photon interface.

The use of photon emission as a spin-dependent operation is just an example. Another interaction that can change the photon state conditioned on being in $|\uparrow\rangle$ or $|\downarrow\rangle$ can be used to realize the same scheme. This interaction can be, for example, conditional reflection or transmission of an incoming photon, a phase shift, or photon absorption.

Having created spin-photon entanglement, it is possible to use it to generate remote spin-spin entanglement. In our example, measuring the combined state of the photons, each entangled with a spin, can project the total state into spin-spin entanglement. If we have generated spin-photon entangled states from two remote systems, detecting a photon at a time *Early* and one at a time *Late* will project the system in the entangled state

$$|\psi\rangle = \frac{1}{\sqrt{2}}(|\uparrow\downarrow\rangle + |\downarrow\uparrow\rangle). \quad (2.5)$$

This only works if we do not know what spin each photon is entangled with. We can erase the information on where the photon is coming from ("*which-path information*") by using a beam splitter (schematic in Fig. 2.1(c)). To remove the path information, or to interfere the photons, they need to be indistinguishable. This results in strict requirements on the coherence and frequency of the optical transition used, which in turn pose requirements on the properties of the spin-photon interface.

2.1.2. THE NV, STATE OF THE ART

The Nitrogen-vacancy center was the first diamond defect to be employed for quantum technology applications. This color center appears naturally in diamond, where nitrogen is a common impurity. It allowed milestone experiments for quantum networking, quantum sensing, and quantum simulations, leveraging its coherent spin-photon interface, its excellent spin coherence properties, and the sensible coupling to nearby nuclear spins in diamond such as ^{13}C isotopes.

The key results with the NV on remote entanglement generation range from the first demonstration of a loophole-free Bell test [3], to the realization of a three-node quantum network [4] and teleportation between non-neighboring qubits [5]. At the same time, seminal work on controlling and using the surrounding spins as a quantum register [6] allowed the realization of fault-tolerant operations [7] and quantum simulation of a discrete time crystal [8].

The NV is widely considered a cornerstone of solid-state defects experiments, and other emerging candidates naturally end up being benchmarked against the NV's features and results. However, this color center has two evident drawbacks. First, the spin-photon interface is not efficient, with only 2.5% of photon emission happening in the narrow and coherent zero-phonon line (ZPL) transition, and the rest through spectrally broad phonon-assisted transitions that form the phonon side-band (PSB). This means that generating spin-photon entanglement with the scheme in Fig. 2.1(b) will fail most of the times because the emitted photon is not coherent. Second, the optical transition is very sensitive to electric fields, causing large spectral noise when the NV is located close to a noisy electronic charge environment, for example, the diamond surface. This limits the range of devices that can be developed based on the NV.

2.1.3. GROUP-IV VACANCY CENTERS

The family of so-called Group-IV (GIV) vacancy color centers [9], formed by an impurity atom of Group IV of the periodic table (or Group 14 in current IUPAC nomenclature) and two carbon vacancies, has gathered a lot of attention and experimental effort in the last decade, as a possible enabling color center for the next generation of diamond-based quantum nodes.

DEFECT SYMMETRY

In this class of defects the impurity, which can be a Si, Ge, Sn, or Pb atom, sits in an interstitial position in the diamond lattice between the two carbon vacancies, in what is commonly called a *split-vacancy configuration* (Fig. 2.2(a)). The resulting structure has a D_{3d} symmetry, which is an inversion symmetry with the central point

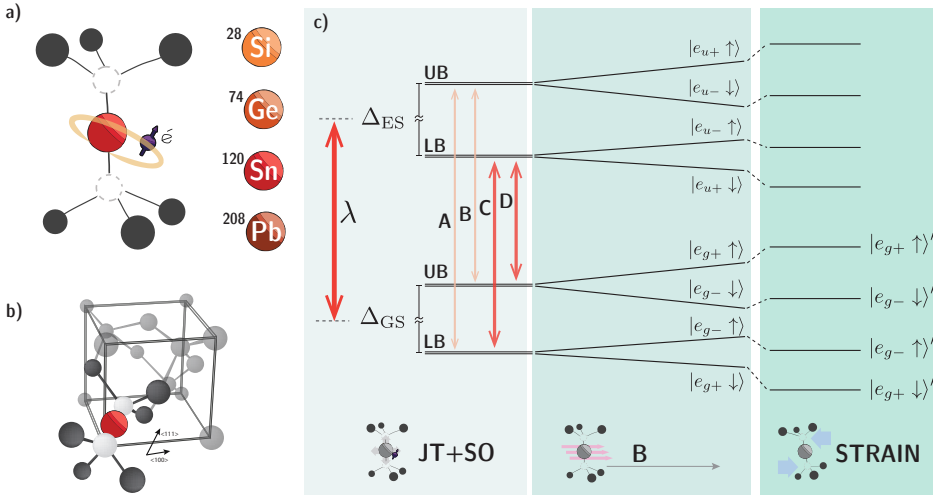


Figure 2.2: **Group-IV Vacancy Centers.** (a) Defect configuration and the atoms that can form Group-IV vacancy centers, with the most abundant isotope. (b) Schematic of the Group-IV structure in the diamond unit cell. The symmetry axis is along the $\langle 111 \rangle$ diamond crystallographic direction. (c) Electronic structure of the Group-IV under the effect of Jahn-Teller (JT) and Spin-Orbit (SO) effects (left), Magnetic field B (center), and strain (right).

located at the atom position. The hypothesis of this structure is supported by *ab initio* and density functional theory (DFT) calculations [10] and confirmed by experimental results. Figure 2.2(b) shows how this structure looks like in the diamond unit cell.

A consequence of the inversion symmetry is that the permanent electric dipole vanishes, making the level structure in first-order insensitive to electric fields. This in turn results in a defect that is very resilient to fluctuating charges in the surroundings, and does not suffer from spectral diffusion as much as the NV center. This holds also when the centers are integrated in nanometer-scale structures, like nanodiamonds or nanophotonic devices. Due to the sub-wavelength dimensions and the heavy fabrication processes, these devices host a very noisy charge environment close to the emitter. The opportunity of nanoscale integration enables a wide range of devices to be developed, with the potential to drastically enhance the efficiency of spin-photon interfaces and pave the way for scalable systems.

ELECTRONIC STRUCTURE

The electronic charge state of interest for quantum applications (and usually quite stable in undoped diamond) is the negatively charged Group-IV (Si/Ge/Sn/PbV⁻) center. We will omit the ⁻ from this point on. Its electronic structure, which has spin $\frac{1}{2}$, features a ground and an excited state with opposite wavefunction parity, even (g) for the ground state (GS) and odd (u) for the excited state (ES). Each has at least two spin-degenerate orbital branches (Fig. 2.2(c)) which are split by Jahn-Teller effect and spin-orbit coupling [11]. We refer to them as Lower Branch (LB) and Upper Branch (UB).

Figure 2.2 shows the level scheme, with the relevant parameters reported in Table 2.1. The strength of the spin-orbit coupling $\lambda_{GS}(\lambda_{ES})$ is mostly what determines the energy splitting between branches in the ground (excited) states, $\Delta_{GS}(\Delta_{ES})$. In general, the splitting scales as $\Delta = \sqrt{\lambda^2 + 4Y^2}$, where Y is the magnitude of the Jahn-Teller effect [12] and λ is the spin-orbit coupling factor. For different atoms, the strength of Jahn-Teller and spin-orbit coupling is different [10]. The exact electronic structure of the heavier GIV centers, SnV and PbV, is still a matter of open research.

Under an external magnetic field, the Zeeman effect lifts the spin degeneracy in each branch, and the electronic structure reveals eight spin-orbital energy levels. Natively, these levels have both opposite spin and orbital components. External crystal strain can change the orbital content of the states and shift them in energy.

| Color Center | λ [nm] | τ [ns] | $\Delta_{GS} / \Delta_{ES}$ [GHz] | $QE \times DW$ |
|------------------|----------------|--------------|-----------------------------------|--------------------------------------|
| SiV ⁻ | 737 | 1.8 [13] | 50/260 [11] | $(0.1 \sim 0.3) \times 0.7$ [13, 14] |
| GeV ⁻ | 602 | 5 [9] | 152/1120 [15] | $\sim 0.2 \times 0.6$ [16] |
| SnV ⁻ | 619 | 4.5 ~ 8 [17] | 830/2900 [17] | $\sim 0.8 \times 0.57$ [18] |
| PbV ⁻ | 552 | 4.4 [19] | 3800 [19] / 6900* | ? |

Table 2.1: **Main properties of Group-IV centers.** λ : ZPL wavelength (C-transition). τ : excited state lifetime. $\Delta_{GS, ES}$: Splitting of the ground and excited states orbital branches in unstrained centers. QE : Quantum efficiency. DW : Debye-Waller factor. *Theoretical value from *ab-initio* calculations [10]. ?: Unknown.

STATE OF THE ART

The SiV is the most experimentally advanced of the GIV centers. Its integration in nanophotonic cavities and the development of high-fidelity control over the electron and isotope nuclear spin recently allowed the first demonstration of remote entanglement with a GIV center [20]. At the other end of the periodic table, not much is known about the PbV. Spectroscopy experiments showed coherent and stable optical emission and confirmed the expected parameters from DFT calculations [19]. However, the experimental results are to date limited to optical spectroscopy. The GeV does not have the same level of maturity as the SiV, but several experiments have been realized, including coupling to nanophotonic waveguides [21, 22].

The SnV has recently and quickly gained attention as a potentially promising alternative to the SiV. The motivations for that will be more clear as we dive into the properties of this color center.

2.2. THE TIN-VACANCY CENTER

2.2.1. THE DEFECT

The defect structure of the SnV is essentially the same as the other GIV centers: a Sn atom occupies the interstitial position between two Carbon vacancies. As for the other GIV centers, we focus on the optically active negatively charged state, SnV⁻, with the

electronic structure in Fig. 2.2(c). The zero-strain energy splitting is 830 GHz in the Ground State (GS), mostly determined by λ_{GS} [23], and 2900 GHz in the Excited State (ES).

SYMMETRY AXIS AND POLARIZATION

The symmetry axis of Group-IV defects is along the $\langle 111 \rangle$ crystallographic direction of the diamond, as shown in Fig. 2.2(b). This axis sets the reference for the direction of external perturbations, like magnetic field and strain. We refer to off-axis field to indicate a magnetic field that is not aligned with the $\langle 111 \rangle$ axis, and transverse strain to indicate strain in the plane perpendicular to the $\langle 111 \rangle$.

The electric transition dipole is oriented along the $\langle 111 \rangle$ axis for the C and B transitions, which are linearly polarized, and in the perpendicular plane for the D and A transitions, which are circularly polarized.

MAGNETIC FIELD

The spin quantization axis is pinned by spin-orbit interaction to the symmetry axis of the emitter, but an off-axis magnetic field tends to change its orientation. The result is that the spin axis is oriented in between the two, depending on the magnetic field strength compared to the spin-orbit coupling. However, each orbital branch experiences different spin-orbit interaction strengths, which causes the spin quantization axis to be slightly different in every branch. This effect is enhanced with a stronger off-axis component of the magnetic field. A different spin quantization axis results in overlap between the spin states in the branches, relaxing the selection rules of the optical and orbital transitions.

ORBITAL BRANCHES POPULATION

The full level scheme is reduced in practical applications to the simplified structure in Figure 2.3. At cryogenic temperatures the population of the Excited State UB is negligible, and any excitation quickly decays to the LB. As a result, the optical transitions taking place from that branch are suppressed at temperatures $\lesssim 100$ K [17]. The population of the Ground State UB depends on the operation temperature, for temperatures $\lesssim 10$ K the rate of phonon transitions to this state is negligible compared to the fast phonon decay to the LB. In general, the short lifetime of this state makes it impractical to use.

ELECTRIC FIELD

As introduced in 2.1.3, the inversion symmetry typical of Group-IV defects makes the SnV first-order insensitive to electric fields. Experiments on Stark effect in SnV centers [24, 25] confirmed this, showing a quadratic response to an external electric field. The SnV centers have proven to maintain good optical coherence properties even when the color center is located in the vicinity of the diamond surface [26].

2.2.2. SPIN-PHOTON INTERFACE

With an external magnetic field, the Zeeman effect lifts the spin degeneracy of the SnV electronic states and the defect can be used as a spin-photon interface.

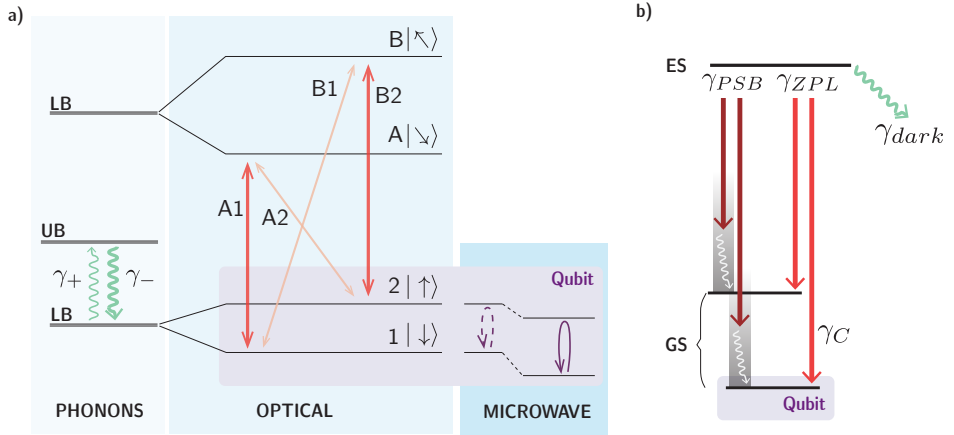


Figure 2.3: **SnV-based Spin-Photon Interface.** (a) Schematic of the relevant phonon (left), optical (center), and microwave (right) transitions for using the SnV as a spin-photon interface. The microwave transition is allowed when there is mixing between the orbital components of the states (indicated here by the shifted energy states). (b) Possible decay channels from the excited state.

A qubit can be defined in the spin-split states of the Lower Branch of the ground state. The energy level structure of interest for the SnV spin-photon interface involves the 619 nm C-transition and is composed of the four-level scheme in the Voigt configuration shown in Fig. 2.3(a). While the two spin-conserving transitions A1 and B2 are always present, the spin-flipping transitions A2 and B1 are only allowed when an off-axis component of the magnetic field is present, due to the different quantization axis which creates an overlap of the spin states. The cyclicity of the transitions is dependent on this overlap and can be controlled to some extent with the magnetic field angle and magnitude [27]. Crystal strain can also affect the cyclicity [28].

The lifetime of the excited state has been measured in the range between 5 and 7 ns in bulk diamond [9], with values above 7 ns reported in nanostructures [29] or close to the diamond surface [17]. This corresponds to a Fourier transform limited optical transition linewidth between 20 and 30 MHz. Lifetime-limited transitions have been measured for SnV both in bulk [23] and in nanophotonic structures [26], where also the generation of indistinguishable photons from a single SnV was demonstrated [29].

Due to a different electronic g -factor in the ground and excited states, lifting the degeneracy of the spin states also splits the optical transitions. Generally one seeks a splitting of the optical transitions with the magnetic field, in particular A1 and B2, that is significantly larger than the linewidth, to have well-resolved and singularly addressable transitions. This is possible in the SnV with magnetic fields in the order of a few tens or hundred of mT, depending on the orientation.

EFFICIENCY OF THE OPTICAL TRANSITION

One of the features that make the SnV promising compared to other color centers is the combination of both the high quantum efficiency (QE) and Debye-Waller (DW) factor. Figure 2.3(b) shows the relevant decay paths for the spin-photon interface. The quantum efficiency is defined as the radiative decay rate over the total decay rate:

$$QE = \frac{\gamma_{\text{rad}}}{\gamma_{\text{rad}} + \gamma_{\text{dark}}}. \quad (2.6)$$

It is an intrinsic property of the color center and its surrounding environment. The balance between different radiative and non-radiative (dark) decay channels is strongly influenced by the molecular-like electronic orbitals of the defect, which set properties such as the strength of the optical dipole moment, the selection rules, electron-phonon coupling, presence of metastable dark states and so on. Even though density functional theory (DFT) calculations can provide information on the expected orbitals, exact knowledge is elusive for most defects. In addition, the radiative decay rate also depends on the local density of states (LDOS). This is influenced by the effective refractive index in the surroundings of the color center, for example in nanodiamonds compared to bulk, or by cavities and other devices.

Within the radiative channels, the decay can happen through a direct transition (or zero phonon line, ZPL) or via a phonon-assisted process, from which a spectrally broad phonon sideband (PSB) originates. The ratio of ZPL decays compared to the combined ZPL and PSB is defined as the Debye-Waller factor:

$$DW = \frac{\gamma_{\text{ZPL}}}{\gamma_{\text{ZPL}} + \gamma_{\text{PSB}}}. \quad (2.7)$$

Finally, when more than one ZPL transition is present, as is the case for the SnV center, we can define a branching ratio (BR) of decays in a ZPL of interest (in our case the C-transition) compared to the total ZPL decay:

$$BR = \frac{\gamma_{\text{C}}}{\gamma_{\text{ZPL}}}. \quad (2.8)$$

The product of these three numbers is an important figure of merit for the efficiency of a spin-photon interface. From the values in table 2.1 the SnV shows a significant improvement in ZPL emission of around 20 times over the NV and more than two times better than the SiV in the most conservative estimate. The BR of SnV in the C transition is still unclear, but experimental estimates suggest a value of 0.8 [30]. The total efficiency of the SnV spin-photon interface can be quantified in one parameter [31]

$$\zeta = QE \times DW \times BR = 0.36 \pm 0.03. \quad (2.9)$$

SPIN CONTROL

Apart from a coherent optical transition, a spin-photon interface requires coherence and control of the spin. Precise and efficient control of the spin qubit is not trivial in the SnV center. Encoding the qubit within an orbital branch results in the two states having

both opposite spin and orbital components. This makes a direct transition between the two qubit states theoretically non-allowed. In practice, there are three approaches to solving this challenge: mixing either the orbital or spin component to relax the selection rules and make the transition allowed, or using two fields to drive the transition through a common third (virtual) state. A review of methods for spin control in diamond can be found in Ref. [32].

By mixing the orbital components of the qubit states, driving the spin transition with a microwave-frequency electromagnetic field becomes possible. The orbital character of the states can be altered by crystal strain, either naturally present in the diamond or induced with fabricated structures. In the presence of strong transverse strain, which acts on the E_x and E_y symmetry of the center with factors β and α respectively, the orbital part of the qubit states changes as [33]:

$$|e_{\pm}\rangle \rightarrow |e_{\pm}'\rangle = \cos(\theta/2) |e_x\rangle \pm \sin(\theta/2) |e_y\rangle, \quad (2.10)$$

with $\theta = \arctan(\beta/\alpha)$. The effect of strain on the mixing scales compared to the strength of spin-orbit coupling, which can be written as a condition on the magnitude of the transverse strain

$$\xi_{\text{strain}\perp} = \sqrt{\beta^2 + \alpha^2} \gtrsim \lambda_{\text{GS}}. \quad (2.11)$$

In the SnV, this means that significant strain is needed to create orbital mixing, which makes microwave spin control possible in some experimental conditions. This will be discussed more in section 2.2.4. Nevertheless, high fidelity and relatively fast spin control using microwaves was shown both in moderately [27] and highly strained [34] SnVs. A very recent theoretical study [35] investigated in detail the interplay between strain and the orientations of the static and driving magnetic fields and their effect on microwave spin control. In the particular case where the static bias field is perpendicular to the SnV symmetry axis and the driving field is parallel to it, the efficiency of the microwave control is optimal, especially for low strain. Working in this regime could relieve the need for strain and make spin control significantly faster. However, a strong off-axis field affects the cyclicity of the optical transitions which can be detrimental in some applications.

A similar approach is to mix the spin states with a strong off-axis magnetic field, exaggerating the difference in spin quantization axis between the two states. In this regime, the transition can be coherently driven by phonons. This was realized for SiV centers using a surface acoustic waves (SAW) device on the diamond surface [36].

The third approach consists of coherently driving with two fields. This can be done optically, making use of a "Lambda scheme" between the two qubit states and a common (virtual) excited state with allowed transitions. A two-photon process allows to coherently transfer the population from one qubit state to the other. This is commonly referred to as all-optical control. This technique can be used in principle even in the absence of strain but requires an off-axis magnetic field to allow the spin-flipping transition. All-optical control of the SnV spin has been demonstrated [28].

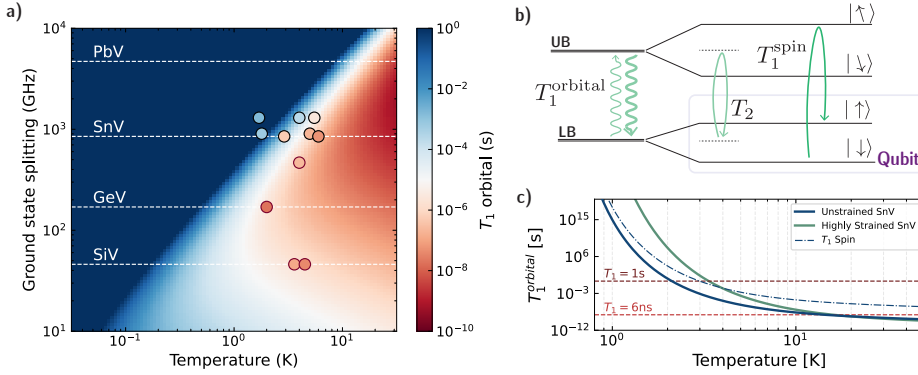


Figure 2.4: **Dephasing Induced by Direct Phonon Transitions.** (a) Orbital relaxation time, T_1^{orbital} , caused by direct phonon transitions at varying temperature and ground state splitting. To normalise this figure, a factor $f = \chi\rho \approx 4.6 \times 10^{-9} \text{GHz}^{-2}$ is extracted from T_2^* measurements performed in our lab at $T \sim 4 \text{K}$ [37]. For comparison we report with the same colorbar the experimental measurements of T_2 , T_2^* and T_1^{orbital} found in literature for SnV (circles with black edge, [23, 27, 34]) and SiV or GeV (circles with red edge [38–41]). Note that T_2^* and T_2 measurements, especially at low temperatures, can be limited by something other than phonon transitions. (b) Level scheme and schematic of the different timescales of relaxation and dephasing. (c) Simulations of orbital relaxation for SnV at no strain ($\Delta_{\text{GS}} = 830 \text{GHz}$) and high strain ($\Delta_{\text{GS}} = 1300 \text{GHz}$). The dashed lines indicate relaxation times of 1s and 6ns to mark the different regimes, and the dash-dotted line indicates spin relaxation for the unstrained case (assuming spin cyclicity of 1200, which has been reported for coarsely aligned magnetic field [34]). Note that here we do not take into account second-order phonon processes that become the limiting mechanism for relaxation at low temperatures.

SUMMARY

Overall, the SnV provides all elements for an efficient and flexible spin-photon interface. The Voigt scheme of Fig. 2.3, where the parameters of the transitions can be to some extent controlled by the angle and strength of the magnetic field, offers a platform where all main elements needed are present:

- spin control can be realized either all-optically or via the weakly allowed direct microwave transition,
- a non-cycling spin flipping transition (B1 or A2) can be used for pumping the population in a specific spin state and therefore initializing the qubit,
- a cycling transition (A1 or B2) can be used for non-destructive spin state readout and (spin-dependent) single photon generation.

In addition to that, the high QE and DW factors make the emission of coherent ZPL photons efficient.

2.2.3. PHONONS

The main spin and optical dephasing mechanism for the SnV center, as well as for the other Group-IV, is phonon transitions. Phonons can change the system state between orbital branches within the ground and excited states. This orbital relaxation mechanism

can cause dephasing of both the optical transition and the coherent spin state, as well as spin relaxation. The main contribution is given by direct phonon transitions, which can only happen if phonons are present in the environment that have energy matching the transition frequency. As the orbital branches of the SnV have well-defined energy splittings ($\Delta_{\text{GS}} = 830$ GHz and $\Delta_{\text{ES}} = 2900$ GHz), a straightforward way to reduce direct phonon transitions is to lower the temperature so that the phonon population with matching energy to the transition is suppressed. The limiting phonon transition for the operation of SnV as a spin-photon interface is the one between the LB and UB of the ground state. The phonon transition rates from lower to upper branch γ_+ and from upper to lower branch γ_- are given by [42]:

$$\gamma_+ = 2\pi\chi\rho\Delta_{\text{GS}}^3 n(\Delta_{\text{GS}}, T), \quad (2.12)$$

$$\gamma_- = 2\pi\chi\rho\Delta_{\text{GS}}^3 [n(\Delta_{\text{GS}}, T) + 1], \quad (2.13)$$

where χ and ρ are constants related to the electron-phonon interaction frequency and phononic density of states, respectively, and $n(\Delta_{\text{GS}}, T)$ is the thermal population of phonons with frequency Δ_{GS} following a Bose-Einstein distribution. One can see that while the decay rate γ_- is always present, and scales with the cube of the energy splitting so it is faster for larger Δ_{GS} , the upwards transition rate γ_+ is suppressed by the vanishing phonon population at decreasing temperatures or increasing Δ_{GS} . Thus, given a ground state splitting, this sets the maximum allowed operation temperatures for the color center. This is where the SnV has one of its advantages compared to SiV and GeV. Figure 2.4(a) shows the phonon-induced orbital relaxation time, which is given by

$$T_1^{\text{orbital}} = 1/\gamma_+, \quad (2.14)$$

as a function of temperature and ground state splitting. Here we neglect the contribution of γ_- which at low phonon population is much faster than γ_+ . The white dashed lines indicate the value of Δ_{GS} for the unstrained Group-IV centers. A steep transition marks the regime where, thanks to the suppressed phonon processes, the orbital T_1 becomes long. In this regime, direct phonon transitions stop being the limiting dephasing mechanism. While for SiV and GeV these conditions are met at temperatures of hundreds of mK, already between 1 and 2 K the SnV can operate without being limited by direct phonon transitions. Commercial closed-cycle cryostats can reach temperatures down to 1.7 K, other helium cryostats can provide cooling to ~ 500 mK without the need for dilution-based systems. This lowers the cost and complexity of experimental setups for SnV, with a positive impact on potential scalability.

TEMPERATURE REGIMES

We can highlight three interesting temperature regimes for the SnV, which correspond to optical coherence, spin coherence, and spin relaxation time.

When the orbital relaxation is faster than the excited state lifetime τ it causes pure dephasing of the optical transition. This makes a less stringent temperature requirement than what is usually needed for spin coherence. The transition linewidth including dephasing induced by population transfer scales as [43]

$$\gamma = \gamma_0 + \gamma_{\text{deph}}, \quad (2.15)$$

around the range where γ_+ is on the order of the spontaneous decay rate γ_0 , the dephasing rate is given by [42] $\gamma_{\text{deph}} \approx \gamma_+$. The linewidth approaches the transform-limited value already for temperatures $\lesssim 6$ K, where $T_1^{\text{orbital}} \gg \tau$. At higher temperatures, where higher-order phonon processes become relevant, the linewidth scales as a third or fourth-order polynomial of the temperature [42]. Consequently, experiments with the SnV where only optical coherence is needed have a relaxed temperature constraint.

In the case of spin coherence, however, the goal is to not be limited by phonon transitions at all. Therefore, the orbital relaxation time should be as long as possible, or at least longer than other decoherence sources. For this, the temperature operation point has to be in the regime where $n(\Delta_{\text{GS}}, T) \ll 1$. As anticipated, this is around 1 K for SnVs. Spin coherence is directly limited by orbital relaxation, rather than spin relaxation, because of the different energy splitting of the spin states in the lower and upper branches of the ground state. The time evolution in the two branches is different and even though the spin state is conserved after an orbital transition going to the upper branch and back, there will be an unknown phase factor. Ultimately, this means that the coherence is lost as soon as a phonon transition to the upper branch happens. Or, more explicitly,

$$T_2^* \leq T_2 \leq T_1^{\text{orbital}} \leq T_1^{\text{spin}}. \quad (2.16)$$

The decoherence induced by orbital relaxation cannot be mitigated using decoupling techniques, this is why it not only marks the limit for T_2^* but also for T_2 .

Orbital transitions can also lead to the relaxation of the spin state. This is again due to the slightly different spin quantization axes in the orbital branches. The spin overlap, which is determined by the orientation and magnitude of the magnetic field and by strain, leads to a finite cyclicity of the orbital transition η_{orb} . The spin relaxation time is determined by $T_1^{\text{spin}} = \eta_{\text{orb}} T_1^{\text{orbital}}$, which leads to the right-most relation of Eq. 2.16. When the magnetic field is moderate and not strongly off-axis the cyclicity can be high, and therefore the spin relaxation time can be much longer than the orbital relaxation.

From this information, we can identify the temperature range for the three operation regimes. At temperatures $\lesssim 6$ K the SnV maintains optical coherence. This can be enough in some applications, for example for using the color center as a single photon source. At temperatures $\lesssim 1.5$ K the spin coherence is not limited by direct orbital transitions. This is the required regime for operating the spin as a qubit. In between these two regimes, it is possible to have both optical coherence and long spin relaxation times. This might be a useful regime, e.g., for realizing spin-controlled photonic operations, where good fidelity of the spin state is needed but not coherence of the quantum state. An example is single photon switches [44], or single photon sources realized using a Raman scheme between the two spin states [45].

2.2.4. STRAIN

Strain plays an important role for Group-IV centers and especially for the SnV. The orbital content of the electronic states is largely determined by spin-orbit coupling, in-

trinsic to each color center, but external strain can modify their character and alter the electronic behavior, with a limit at high strain where the electron behaves similarly to a free electron. For the strain to be considered high, its magnitude has to be comparable to or bigger than the strength of spin-orbit coupling in the ground state (Equation 2.11). Additionally, with Group-IV centers being insensitive to electric fields, strain is the main external perturbation that the defect couples to. Here we focus on three effects that make strain an interesting tool for using the SnV as a quantum system: strain tuning, high-temperature operation, and microwave spin driving.

STRAIN TUNING

DC Stark effect induced by static electric fields is a common frequency tuning mechanism, it is used for NV centers and other defects. With the SnV being first-order insensitive to electric fields, Stark tuning becomes less efficient. Although electric field tuning of the SnV has been demonstrated [24, 25], as a second-order effect it requires high electric fields and the range is practically limited to only a few GHz. However, Group-IV centers are sensitive to strain, which by mixing the orbital character of the states and shifting them in energy, modifies the frequency of the optical transitions. Strain-based tuning of SiV centers in an electrically actuated nanophotonic cantilever [46] has been shown to allow tuning of the *C* transition up to 0.3 nm. An integrated platform for strain-based tuning has also recently been realized for SnV, allowing on average 2 GHz (with a maximum of 25 GHz) tuning range [47].

HIGH TEMPERATURE OPERATION

Figure 2.4(a) gives an insight: at a fixed temperature, increasing the ground state splitting can slow down the orbital relaxation. Strain can increase Δ_{GS} and make the emitter less sensitive to the surrounding phonon bath. Results on both controlled tunable strain on SiV [40] and on naturally highly strained emitters with SiV at 1.5 K [48] and SnV at 4 K [34] have shown how strain-induced increase of Δ_{GS} allows improving the spin coherence at temperatures higher than the usual operation regime.

STRAIN FOR MICROWAVE DRIVING

We have already seen in 2.2.2 the challenge of driving the spin transition with microwaves, generally, some strain is necessary for this task. What strain regime is optimal for practical applications, which require fast and high-fidelity microwave driving, is still unclear. Recent results show microwave driving in both high strain ($\Delta_{GS} \sim 1500$ GHz, corresponding to 0.075% crystal strain [34]) and moderate strain ($\Delta_{GS} \sim 900$ GHz [27]) with similar gate fidelities $\approx 99\%$ and Rabi frequencies in the few MHz range. Note that the device used for the delivery of the microwave signal is very different in the two realizations.

INDUCING STRAIN

Given the relevance of strain for applications of the SnV and Group-IV in general, it is worth reviewing the main methods to get strain in the system.

The host device itself often provides a strained environment for the SnV. Bulk diamond samples can have inherent strain originating from dislocations and other crystal imperfections. In nanophotonic fabricated devices, strain can just be a consequence of the device geometry or stress from fabrication. In addition to these, the implantation of SnV adds crystal damage, defects, and inactive Sn atoms which in turn can increase the naturally present crystal strain. The SnV is susceptible to variations of the local strain environment, resulting in a slightly different emission frequency. The variation of SnV frequency due to the surrounding strain environment is referred to as inhomogeneous distribution. While allowing for some inherent defect strain that can be useful, inhomogeneous distribution also leads to the challenge of finding emitters with the same emission frequency, and the more spectrally broad is the distribution, the bigger the tuning range required to get two arbitrary emitters at the same frequency.

Toward developing a more scalable and deterministic platform, it is important to reliably and reproducibly apply strain to the color centers. In literature there are several experimental demonstrations of devices that can apply strain in a static [34, 49] or dynamically controlled way [22, 46]. While control over the strain is needed to use it as a frequency tuning device, the possibility of reproducibly applying high strain statically is sufficient if the goal is to enable high-temperature operation or improve microwave susceptibility.

2.2.5. PROSPECTS AND TRADE-OFFS

The SnV comes with excellent optical properties and a flexible spin-photon interface, where different parameters can be tuned or leveraged for use in different applications. However, this results in constraints and choices to be made as the interplay between strain, ground-state splitting, and magnetic field can lead to conflicting requirements and different operation regimes. One example is how different strain regimes and different magnetic field alignment and strength can make a SnV center more suited for microwave or all-optical driving of the spin, both with high fidelity [34].

Overall, the SnV shows clear advantages over other known Group-IV centers. The high efficiency of the C-transition offers the valuable advantage of allowing high cooperativity with lower requirements on device fabrication, which means relaxed constraints for cavity quality factors and possibly operation in waveguides.

The larger ground state splitting allows operation at Helium-4 temperatures, without the need for a dilution refrigerator. Experiments on highly strained SnVs [34] also pose the prospect of high-temperature operation, above 4K where the practical complexity of cryostats becomes less and the cooling power available is more.

With SiV centers, the encoding of the qubit in the nuclear spin state with non-zero spin isotopes (^{29}Si) proved to offer longer coherence times and higher operation temperatures compared to the use of the electron as a qubit [48]. Work on the SnV isotopes with nuclear spin, such as ^{117}Sn and ^{119}Sn [50, 51], shows that they possess similar properties and offer an interesting possible way of improving the flexibility of the SnV platform.

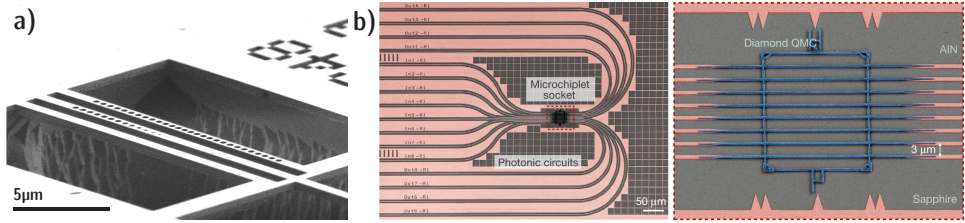


Figure 2.5: **Nanophotonics in Diamond.** (a) SEM image of a photonic crystal cavity device etched in bulk diamond. Adapted from [52]. (b) Hybrid integration of a diamond chip in a photonic circuit. Reproduced with permission from [22].

2.3. WAVEGUIDE AND CAVITY QED WITH GROUP-IV CENTERS

With the inversion symmetry of GIV centers and their resilience in a noisy charge environment comes an opportunity: integrating these color centers in nanophotonic structures such as photonic crystal cavities and waveguides. Here we introduce the basic concepts and review the state of the art for cavity-QED and waveguide-QED experiments with SiV, GeV, and SnV centers.

2.3.1. NANOPHOTONIC INTEGRATION IN DIAMOND

Fabrication of suspended nanostructures in diamond is a technically difficult challenge, but it is necessary to realize photonic structures with a high level of confinement of the optical modes in the diamond itself [53, 54]. Most established material platforms for integrated photonics (e.g. silicon or silicon-nitride) rely on high-quality thin films that can be grown or deposited on a material with different optical and chemical properties. If the refractive index contrast between the two adjacent materials is enough to support confined optical modes, it is possible to create monolithic integrated waveguiding devices. Alternatively, leveraging the different chemistry (i.e. selectivity to wet etch chemical solutions) it is possible to nanofabricate the photonic structures on the deposited layer, with subsequent wet etch of the underlying sacrificial layer. Heteroepitaxial growth of high-quality diamond thin films at wafer scale is still elusive and with it a straightforward fabrication method for diamond photonic structures. While some efforts towards diamond heteroepitaxial growth are present [55], the process introduces many impurities and crystal dislocations, ultimately making it unsuitable for quantum applications. Recently, promising results on diamond-on-insulator through smart-cut and direct bonding of diamond membranes have been shown [56]. Generally, given the diamond material has high etch resistance to any wet chemical solutions, the most frequently used approach to nanofabrication of suspended devices relies on the dry etch methods: the patterned devices are undercut in bulk diamond using typically oxygen-based etch recipes. This can be done either with angled directional inductive-coupled plasma (ICP) reactive ion etch (RIE) [57] or with a quasi-isotropic etch method, which relies on different etch rates for diamond crystallographic planes [58], which

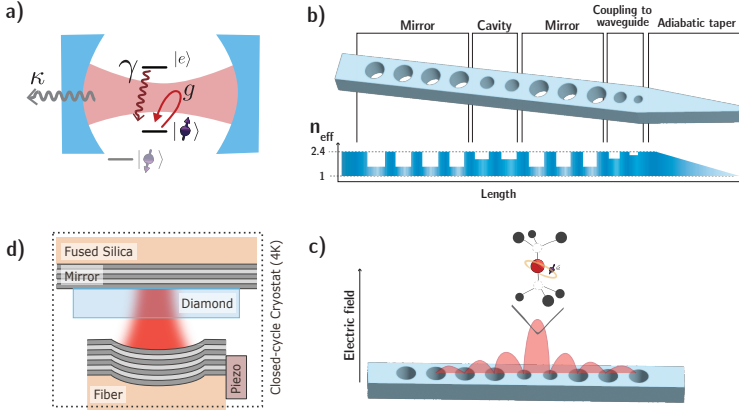


Figure 2.6: **Cavity-QED.**(a) Schematic of an atom coupled to a cavity in a cavity-QED system. (b) Schematic of a photonic crystal cavity. The refractive index modulation forms Bragg mirrors with a designed band-gap. A defect in the periodic structure allows a localized mode and forms a cavity. Outcoupling of the waveguide mode can be done by tapering the mirror to a waveguide and finally tapering the waveguide to allow adiabatic coupling to other structures (e.g. tapered optical fibers or integrated photonic circuits). (c) Schematic of the mode field distribution in a photonic crystal cavity. (d) Schematic of a fiber-based Fabry Perot tunable microcavity. Adapted with permission from Ref. [60] under CC BY 4.0 license terms.

gives devices like the one in Fig. 2.5(a). The latter is the undercut method used for the waveguide devices investigated in this thesis. The detailed fabrication recipe can be found in section 4.8.a.

Toward a scalable and flexible integrated platform, all-diamond devices will likely not grant all the required functionalities for operating a quantum node. One approach to overcome this is hybrid integration [22, 59], as shown in Fig. 2.5(b). Diamond structures, hosting the quantum device, are integrated with conventional integrated photonic and electronic circuits where fabrication is more established. In this way, several key operational components for photon routing, filtering, in- and out-coupling of light to fibers, and electronic signal delivery can be developed separately in a different material.

2.3.2. CAVITY QED WITH GROUP-IV CENTERS

Using optical cavities to enhance the interaction of a quantum system with light is a well-studied approach [61]. A single atomic or atom-like system can be coupled to a single localised optical mode leading to strong interactions with the light field. In the simple picture where the quantum object is a two-level system, as depicted in Fig. 2.6(a), the physics follows the renowned Jaynes-Cummings Hamiltonian:

$$H_{JC} = \hbar\omega_a|e\rangle\langle e| + \hbar\omega_c\hat{a}^\dagger\hat{a} + \hbar g(|e\rangle\langle g|\hat{a} + |g\rangle\langle e|\hat{a}^\dagger), \quad (2.17)$$

where $|e\rangle$ and $|g\rangle$ indicate the ground and excited states of the two-level system transition, \hat{a} is the bosonic operator of the cavity mode and ω_c (ω_a) is the frequency of the cavity (atom optical transition). The factor g is the interaction rate between the atom

and the cavity mode and it is defined as

$$g = \mu_{eg} \sqrt{\frac{\omega_c}{2\hbar\epsilon_0 V}} u(\vec{r}_a) |\vec{d} \cdot \vec{\epsilon}|. \quad (2.18)$$

Here μ_{eg} is the electric dipole moment of the atom transition; the expression in square root takes into account the electric field of a single photon in the cavity, and V is the volume of the electric field distribution in the cavity mode. There is a function that describes the mode field in space, $u(\vec{r})$, normalized to one at the maximum value and evaluated at the atom position \vec{r}_a , and at last a factor $|\vec{d} \cdot \vec{\epsilon}|$ that takes into account the orientation of the transition dipole compared to the cavity field polarization. The overall strength of the coupling for the cavity-atom system is quantified by the cooperativity*

$$C = \frac{4g^2}{\kappa\gamma}, \quad (2.19)$$

where $\kappa = \kappa_{\text{in/out}} + \kappa_{\text{loss}}$ is the total decay rate of the cavity, which includes the decay rate in the input/output channels and in the loss channels, and γ is the decay rate of the atomic transition. In the ideal case, the cooperativity is purely determined by the cavity properties. Since both g^2 and γ are $\propto \mu_{eg}^2$, assuming the atom-cavity resonance condition $\omega_a = \omega_c = \omega$ this can be rewritten as

$$C_{\text{ideal}} = \frac{12\pi c^3}{\kappa\omega V} \propto \frac{Q}{V} \quad (2.20)$$

where $Q = \omega/\Delta\omega$ is the quality factor of the cavity mode with frequency ω and linewidth $\Delta\omega$ (determined by the decay rate κ). Two direct ways of improving the cavity-atom coupling are clear: increasing the cavity Q factor, therefore reducing the cavity losses, and making the cavity as small as possible. There are two relevant platforms for cavity enhancement of diamond color centers [62]. Photonic crystal cavities [63], schematically depicted in Fig. 2.6(b) and (c), can reach mode volumes on the order of half of the wavelength in the material, $V \sim 0.5(\lambda/n)^3$ with n the material refractive index. This in principle allows high cooperativities. However, reaching high quality factors is challenging due to fabrication imperfections and the effect of surface roughness at such a small length scale. By contrast, open Fabry-Perot microcavities [64] (Fig. 2.6(d)) can be realized with very low losses and high Qs at the expense of orders of magnitude bigger mode volumes ($V \sim \mu\text{m}^3$).

In solid-state defects, the optical transition of interest that is coupled to the cavity is not the only possible decay channel from the excited state. For Group-IV centers, as we have seen in section 2.2.2, we can have a fraction of non-radiative decays (QE), PSB emission (DW) and emission in the D-transition (BR). These factors affect the coupling factor g between the transition of interest and the cavity mode since they decrease the dipole moment of the transition. Hence, the product of the branching ratios directly impacts the cooperativity:

$$C = (QE \times DW \times BR) \times C_{\text{ideal}} = \zeta \times C_{\text{ideal}}. \quad (2.21)$$

*Different expressions of the cooperativity are used in literature, usually depending on the definition of κ and γ . The convention we use is common in the solid-state emitters community.

This is another advantage of the SnV, since the total product of these efficiencies is higher than for other group-IV. This means that for the same cavity parameters, the SnV will yield higher cooperativity. Or, looking at it from another angle, to obtain a certain cooperativity the requirements on cavity properties are relaxed. This is valuable because, with the current diamond nanofabrication state of the art, it is challenging to get cavity quality factors as high as the desired designs. Note that, compared to the SiV, the SnV ZPL wavelength being smaller leads to photonic crystal cavities of even smaller mode volume. This also gives higher cooperativity but complicates the fabrication. Any residual broadening of the optical transition, due to dephasing or spectral diffusion, for example, will also impact the cooperativity. The ratio of the experimentally observed linewidth γ_{exp} compared to the ideal transform-limited linewidth γ_0 determines the *coherent* cooperativity

$$C_{\text{coh}} = C \frac{\gamma_0}{\gamma_{\text{exp}}}. \quad (2.22)$$

Again, the stability of the Group-IV optical transition allows the system to have nearly transform-limited linewidth and little spectral diffusion also in nanostructures.

The cavity-atom coupling strength can be divided into three cases. Where $\kappa, \gamma \gg g$ and $C \lesssim 1$ is the weak coupling regime. In this regime, the properties of the atom are modified by the increased photonic density of states at the cavity resonance frequency. This leads to enhancement of the emission in the coupled transition, called Purcell effect, and is associated with a decrease of the excited state lifetime in the cavity τ_{cav} compared to the intrinsic lifetime τ . The Purcell enhancement factor is

$$F_P = C_{\text{ideal}} = \frac{1}{\zeta} \left(\frac{\tau}{\tau_{\text{cav}}} - 1 \right). \quad (2.23)$$

The result is a more efficient photon emission, which usually adds up to an increased collection efficiency since the cavity can be engineered to efficiently extract the single optical mode that the emission is coupled to. However, in this regime, the cavity and atom decay rates are faster than the coupling rate, so the probability that a photon in the mode interacts with the atom is low.

On the other hand, two situations can lead to a high cooperativity, $C \gg 1$. The first one is when $\kappa \gg g \gg \gamma$. This is usually called a "bad cavity" or "lossy cavity" limit. In this situation, Purcell enhancement is stronger as it scales with the cooperativity. Furthermore, even though the cavity decay rate is still the leading timescale, coherent interactions between the atom and photons in the cavity mode start to show. This leads to the atom strongly affecting the cavity spectrum. To this day, all experiments of Cavity-QED with diamond color centers are in this regime. Note that this condition can also result in $C \gtrsim 1$.

Finally, the strong coupling regime is when $g \gg \kappa, \gamma$. In this regime, the interaction exchange rate between the cavity photons and the atom is much faster than all loss channels, so cavity photons interact with the atom multiple times before being scattered out of the system. The atom and cavity coupling is so strong that the cavity mode vacuum field can induce Rabi oscillations of the atom transition (vacuum-Rabi

oscillations), and hybridized atom-cavity modes (dressed states) are formed.

In practice, for the sake of realizing a spin-photon interface for quantum networking applications, all of this can be used in two ways: using Purcell enhancement to increase the spontaneous emission in the cavity mode or using the coherent interaction with input photons to realize spin-dependent single-photon gates.

Cavity enhancement of spontaneous emission requires the least demanding experimental constraints, as it can be obtained already in a weak coupling regime. A Purcell-enhanced transition can be used to generate spin-photon entanglement in a similar way to what is discussed in 2.1.1. The advantages are that the fraction of photons emitted in the transition of interest is larger, the optical transition lifetime is shorter allowing for a higher repetition rate, and the collection efficiency can be increased as the photons are emitted in a well-defined single optical mode. Several experiments have measured Purcell enhancement in a weak coupling regime for SiV and GeV in open Fabry-Perot microcavities [16, 65]. Purcell enhancement of SnV centers was observed both in open microcavities [31] and in photonic crystal cavities [66, 67].

A different approach is to use the coherent cavity-emitter interaction to perform spin-dependent photon gates. In this case, the system should show significant modulation of the cavity reflectivity or transmissivity dependent on the atom state. This is the main approach used for SiV centers in photonic crystal cavities [33, 68], and recently enabled advanced quantum networking experiments showing memory-enhanced quantum communication [69] and remote spin-spin entanglement generation [20]. Significant modulation of a cavity spectrum by a single SnV center has been shown recently in an open Fabry-Perot microcavity [31].

2.3.3. WAVEGUIDE QED WITH GROUP-IV CENTERS

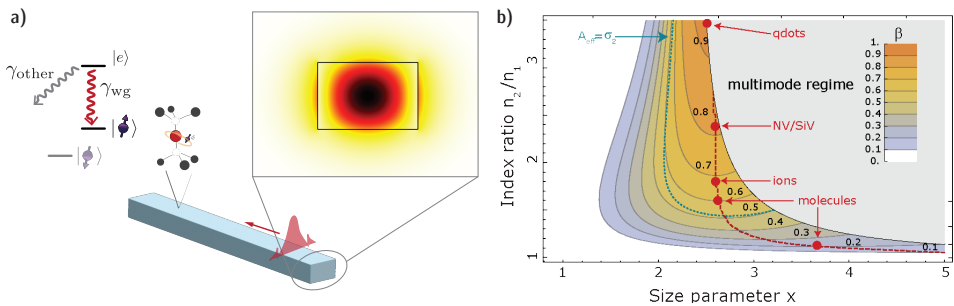


Figure 2.7: **Waveguide-QED.** (a) Schematic of a waveguide-QED system and simulated electric field of a TE optical mode in a single mode diamond waveguide. (b) Maximum β for different material platforms. The size parameter is defined as $x = kr$ with k the light wavevector in the guiding material and r the radius of a circular mode. The dashed blue line marks where the effective mode area is equal to the scattering cross-section of the atom, σ_2 . Adapted with permission from Ref. [70] under CC BY 4.0 license terms.

Another way to enhance light-matter coupling, as opposed to using a cavity's localized mode, is to use a single traveling optical mode in a waveguide as schematically depicted

in Fig. 2.7(a).

A waveguide is a device where the light field is confined in two dimensions and allowed to propagate in one direction. By coupling a two-level system to a single traveling mode the effect relies on just "one pass" of the photon interacting with the atom. In a waveguide-atom system, the strength of the light-matter coupling can be quantified by the decay rate of the optical transition into the waveguide mode, γ_{wg} , against all possible decays, $\gamma_{\text{tot}} = \gamma_{\text{rad}} + \gamma_{\text{dark}}$:

$$\beta = \frac{\gamma_{\text{wg}}}{\gamma_{\text{tot}}}. \quad (2.24)$$

Note that here γ_{rad} includes γ_{wg} .

We can relate this coupling to an equivalent Cooperativity. By considering γ_{wg} as the coupling rate to the single waveguide mode (similar to g) and the total decay rate outside the waveguide $\gamma_{\text{other}} = \gamma_{\text{tot}} - \gamma_{\text{wg}}$ as the loss channels (similar to κ and γ in a cavity), one can define:

$$C_{\text{wg}} = \frac{\gamma_{\text{wg}}}{\gamma_{\text{other}}} = \frac{\beta}{1 - \beta}. \quad (2.25)$$

This is sometimes used to quantify atom coupling to a waveguide mode. As one can see, the perfect coupling condition reads $\beta = 1$ or $C_{\text{wg}} \rightarrow \infty$.

Similarly to the cavity mode volume, the maximal strength of a waveguide-emitter coupling is linked to the effective mode area A_{eff} of the electric field and the position and orientation of the atomic transition dipole. The effective mode field should be comparable with the atom absorption cross section in the material, $\sigma_{\text{atom}} = \frac{3}{2\pi} \left(\frac{\lambda}{n}\right)^2$. While this can be optimized by engineering the mode, there are fundamental boundaries in how small the waveguide can be and still support a guided mode (set by the refractive index contrast between the guiding and the cladding materials) and the emergence of higher-order modes at larger waveguide dimensions (which lower the effective coupling efficiency). For color centers in air-cladded diamond waveguides, these limitations lead to a maximum coupling $\beta_{\text{max}} \sim 0.8$ [70]. For reference, figure 2.7(b) shows the expected scaling of the coupling for different platforms. This is for an ideal dipole coupled to the waveguide. That is, where no extra decay channels are present except the simple two-level transition. Realistically, the coupling will be decreased by imperfect QE, DW, and BR which reduce the fraction decay rates γ_{tot} that can contribute to γ_{wg} .

In the ideal case of $\beta = 1$ the atom behaves as a perfect single photon mirror. This is due to quantum interference between the incoming light field in the waveguide mode and the field scattered by the atom, which results in a strong modulation of the waveguide transmission and reflection signals. For $\beta < 1$ this interference is not perfect and the photon has some probability of being transmitted, decreasing the effect. By exploiting this, the atom-waveguide system can be used similarly to the cavity to generate spin-photon entanglement. The single-photon atom-induced reflection can be used to perform spin-dependent operation on the photon which can lead to spin-photon entanglement. This has currently been realized with quantum dots [71], where couplings can reach $\beta \sim 0.9$. Experiments with group-IV centers coupled to diamond

waveguides have been realized using SiV [68], GeV [21, 22] and SnV [26, 29, 50, 72]. The coupling factors for these experiments so far are on the order of $\beta \sim 0.1 - 0.2$.

2

The waveguide also changes the local photonic density of states, but in contrast with the cavity, this does not cause a strong Purcell effect. The Purcell factor in the waveguide is a combination of the presence of the waveguide mode which gives a small enhancement of LDOS, and the effective refractive index of the emitter surroundings. This can also result in $F_p < 1$ with a consequent slight increase of the lifetime [21]. The magnitude of the Purcell effect is anyway small, so it does not significantly affect the emission. Nevertheless, the waveguide can be used for emission-based spin-photon entanglement, making use of the enhanced collection efficiency.

Waveguide-QED systems can provide similar features as a "lossy" cavity and can be used to develop an improved spin-photon interface compared to bulk systems. Using a waveguide compared to a cavity has the advantage that it is very broadband. For cavity operation, precise frequency tuning of a narrow resonance is a necessary task and can add significant experimental complexity. By contrast, waveguides do not need tuning and can couple at the same time to several emitters over a large frequency range. Moreover, the fabrication of a waveguide has more relaxed requirements on the feature size, making it more reliable and robust. The main disadvantage is that the coupling is not as strong and it is fundamentally limited, compared to cavities where in principle the Q factor would allow arbitrarily high cooperativity, limited by practical challenges, e.g. fabrication. One way to improve the coupling of an atom to a waveguide traveling mode beyond the geometrical limitations is to operate close to the bandgap of a photonic crystal mirror. Near the band edge, it is possible to increase the LDOS for slow-light modes, which then allows strong coupling to the emitter. This can be achieved in photonic crystal waveguides [73], where the guiding structure is confined by or consists of a photonic crystal mirror. These devices are still relatively broadband compared to cavities, such that they do not need precise tuning, and demonstrated strong couplings of $\beta > 0.9$ in quantum dots [74].

BIBLIOGRAPHY

- [1] W. B. Gao, A. Imamoglu, H. Bernien and R. Hanson, *Coherent manipulation, measurement and entanglement of individual solid-state spins using optical fields*, Nature Photonics **9**, 363 (2015).
- [2] M. Atatüre, D. Englund, N. Vamivakas, S.-Y. Lee and J. Wrachtrup, *Material platforms for spin-based photonic quantum technologies*, Nature Reviews Materials **3**, 38 (2018).
- [3] B. Hensen *et al.*, *Loophole-free Bell inequality violation using electron spins separated by 1.3 kilometres*, Nature **526**, 682 (2015).
- [4] M. Pompili *et al.*, *Realization of a multinode quantum network of remote solid-state qubits*, Science **372**, 259 (2021).
- [5] S. L. N. Hermans *et al.*, *Entangling remote qubits using the single-photon protocol: An in-depth theoretical and experimental study*, New Journal of Physics **25**, 013011 (2023).
- [6] C. E. Bradley *et al.*, *A Ten-Qubit Solid-State Spin Register with Quantum Memory up to One Minute*, Physical Review X **9**, 031045 (2019).
- [7] M. H. Aboeih *et al.*, *Fault-tolerant operation of a logical qubit in a diamond quantum processor*, Nature **606**, 884 (2022).
- [8] J. Randall *et al.*, *Many-body-localized discrete time crystal with a programmable spin-based quantum simulator*, Science **374**, 1474 (2021).
- [9] C. Bradac, W. Gao, J. Forneris, M. E. Trusheim and I. Aharonovich, *Quantum nanophotonics with group IV defects in diamond*, Nature Communications **10**, 5625 (2019).
- [10] G. Thiering and A. Gali, *Ab Initio Magneto-Optical Spectrum of Group-IV Vacancy Color Centers in Diamond*, Physical Review X **8**, 021063 (2018).
- [11] C. Hepp *et al.*, *Electronic Structure of the Silicon Vacancy Color Center in Diamond*, Physical Review Letters **112**, 036405 (2014).
- [12] C. Hepp, *Electronic Structure of the Silicon Vacancy Color Center in Diamond*, Ph.D. thesis, Universität des Saarlandes (2014).
- [13] J. N. Becker and C. Becher, *Coherence properties and quantum control of silicon vacancy color centers in diamond*, physica status solidi (a) **214**, 1700586 (2017), arxiv:1709.10321 [cond-mat, physics:quant-ph] .
- [14] E. Neu, M. Agio and C. Becher, *Photophysics of single silicon vacancy centers in diamond: Implications for single photon emission*, Optics Express **20**, 19956 (2012).
- [15] E. A. Ekimov *et al.*, *Germanium-vacancy color center in isotopically enriched diamonds synthesized at high pressures*, JETP Letters **102**, 701 (2015).

- [16] R. Høy Jensen *et al.*, *Cavity-Enhanced Photon Emission from a Single Germanium-Vacancy Center in a Diamond Membrane*, *Physical Review Applied* **13**, 064016 (2020).
- [17] J. Görlitz *et al.*, *Spectroscopic Investigations of Negatively Charged Tin-Vacancy Centers in Diamond*, *New Journal of Physics* **22**, 013048 (2020), arxiv:1909.09435 [cond-mat, physics:quant-ph] .
- [18] T. Iwasaki *et al.*, *Tin-Vacancy Quantum Emitters in Diamond*, *Physical Review Letters* **119**, 253601 (2017).
- [19] P. Wang *et al.*, *Transform-Limited Photon Emission From a Lead-Vacancy Center in Diamond Above 10 K*, .
- [20] C. M. Knaut *et al.*, *Entanglement of Nanophotonic Quantum Memory Nodes in a Telecommunication Network*, (2023), arxiv:2310.01316 [quant-ph] .
- [21] M. K. Bhaskar *et al.*, *Quantum Nonlinear Optics with a Germanium-Vacancy Color Center in a Nanoscale Diamond Waveguide*, *Physical Review Letters* **118**, 223603 (2017).
- [22] N. H. Wan *et al.*, *Large-scale integration of artificial atoms in hybrid photonic circuits*, *Nature* **583**, 226 (2020).
- [23] M. E. Trusheim *et al.*, *Transform-Limited Photons From a Coherent Tin-Vacancy Spin in Diamond*, *Physical Review Letters* **124**, 023602 (2020).
- [24] L. De Santis, M. Trusheim, K. Chen and D. Englund, *Investigation of the Stark Effect on a Centrosymmetric Quantum Emitter in Diamond*, *Physical Review Letters* **127**, 147402 (2021).
- [25] S. Aghaeimeibodi, D. Riedel, A. E. Rugar, C. Dory and J. Vučković, *Electrical Tuning of Tin-Vacancy Centers in Diamond*, *Physical Review Applied* **15**, 064010 (2021).
- [26] A. E. Rugar *et al.*, *Narrow-Linewidth Tin-Vacancy Centers in a Diamond Waveguide*, *ACS Photonics* **7**, 2356 (2020).
- [27] E. I. Rosenthal *et al.*, *Microwave Spin Control of a Tin-Vacancy Qubit in Diamond*, (2023), arxiv:2306.13199 [cond-mat, physics:quant-ph] .
- [28] R. Debroux *et al.*, *Quantum Control of the Tin-Vacancy Spin Qubit in Diamond*, *Physical Review X* **11**, 041041 (2021).
- [29] J. Arjona Martínez *et al.*, *Photonic Indistinguishability of the Tin-Vacancy Center in Nanostructured Diamond*, *Physical Review Letters* **129**, 173603 (2022).
- [30] A. E. Rugar, *Quantum Photonics with the Tin-Vacancy Center in Diamond*, Ph.D. thesis, Stanford University (2022).
- [31] Y. Herrmann *et al.*, *Coherent Coupling of a Diamond Tin-Vacancy Center to a Tunable Open Microcavity*, (2023), arxiv:2311.08456 [quant-ph] .

- [32] L. Orphal-Kobin, C. G. Torun, J. M. Bopp, G. Pieplow and T. Schröder, *Coherent microwave, optical, and mechanical quantum control of spin qubits in diamond*, (2023), arxiv:2312.06431 [quant-ph] .
- [33] C. T. Nguyen *et al.*, *An integrated nanophotonic quantum register based on silicon-vacancy spins in diamond*, *Physical Review B* **100**, 165428 (2019).
- [34] X. Guo *et al.*, *Microwave-based quantum control and coherence protection of tin-vacancy spin qubits in a strain-tuned diamond membrane heterostructure*, (2023), arxiv:2307.11916 .
- [35] G. Pieplow, M. Belhassen and T. Schröder, *Efficient Microwave Spin Control of Negatively Charged Group-IV Color Centers in Diamond*, (2023), arxiv:2312.02637 [quant-ph] .
- [36] S. Maity *et al.*, *Coherent acoustic control of a single silicon vacancy spin in diamond*, *Nature Communications* **11**, 193 (2020).
- [37] S. Niese, *Measuring Microwave Pulse Induced Heating Using Decoherence of the Tin-Vacancy Spin in Diamond*, MSc Thesis, Delft University of Technology (2022).
- [38] B. Pingault *et al.*, *Coherent control of the silicon-vacancy spin in diamond*, *Nature Communications* **8**, 15579 (2017).
- [39] P. Siyushev *et al.*, *Optical and microwave control of germanium-vacancy center spins in diamond*, *Physical Review B* **96**, 081201 (2017).
- [40] Y.-I. Sohn *et al.*, *Controlling the coherence of a diamond spin qubit through its strain environment*, *Nature Communications* **9**, 2012 (2018).
- [41] L. J. Rogers *et al.*, *All-Optical Initialization, Readout, and Coherent Preparation of Single Silicon-Vacancy Spins in Diamond*, *Physical Review Letters* **113**, 263602 (2014).
- [42] K. D. Jahnke *et al.*, *Electron-phonon processes of the silicon-vacancy centre in diamond*, *New Journal of Physics* **17**, 043011 (2015).
- [43] J. L. Skinner and D. Hsu, *Pure dephasing of a two-level system*, *The Journal of Physical Chemistry* **90**, 4931 (1986).
- [44] T. Volz *et al.*, *Ultrafast all-optical switching by single photons*, *Nature Photonics* **6**, 605 (2012).
- [45] E. N. Knall *et al.*, *Efficient Source of Shaped Single Photons Based on an Integrated Diamond Nanophotonic System*, *Physical Review Letters* **129**, 053603 (2022).
- [46] S. Meesala *et al.*, *Strain engineering of the silicon-vacancy center in diamond*, *Physical Review B* **97**, 205444 (2018), arxiv:1801.09833 [cond-mat, physics:quant-ph] .
- [47] L. Li *et al.*, *Heterogeneous integration of spin-photon interfaces with a scalable CMOS platform*, (2023), arxiv:2308.14289 [physics, physics:quant-ph] .

- [48] P.-J. Stas *et al.*, *Robust multi-qubit quantum network node with integrated error detection*, (2022), arxiv:2207.13128 [quant-ph] .
- [49] D. R. Assumpcao *et al.*, *Deterministic Creation of Strained Color Centers in Nanostructures via High-Stress Thin Films*, (2023), arxiv:2309.07935 [physics, physics:quant-ph] .
- [50] R. A. Parker *et al.*, *A diamond nanophotonic interface with an optically accessible deterministic electronuclear spin register*, (2023), arxiv:2305.18923 .
- [51] I. B. W. Harris *et al.*, *Hyperfine Spectroscopy of Isotopically Engineered Group-IV Color Centers in Diamond*, (2023), arxiv:2306.00164 [quant-ph] .
- [52] M. Ruf, *Cavity-Enhanced Quantum Network Nodes in Diamond*, Ph.D. thesis, Delft University of Technology (2021).
- [53] P. K. Shandilya *et al.*, *Diamond Integrated Quantum Nanophotonics: Spins, Photons and Phonons*, *Journal of Lightwave Technology* **40**, 7538 (2022).
- [54] S. Mi, M. Kiss, T. Graziosi and N. Quack, *Integrated photonic devices in single crystal diamond*, *Journal of Physics: Photonics* **2**, 042001 (2020).
- [55] W. Wang *et al.*, *Heteroepitaxy of diamond semiconductor on iridium: A review*, *Functional Diamond* **2**, 215 (2022).
- [56] X. Guo *et al.*, *Direct-bonded diamond membranes for heterogeneous quantum and electronic technologies*, (2023), arxiv:2306.04408 [physics, physics:quant-ph] .
- [57] M. J. Burek *et al.*, *Free-Standing Mechanical and Photonic Nanostructures in Single-Crystal Diamond*, *Nano Letters* **12**, 6084 (2012).
- [58] S. Mouradian, N. H. Wan, T. Schröder and D. Englund, *Rectangular photonic crystal nanobeam cavities in bulk diamond*, *Applied Physics Letters* **111**, 021103 (2017).
- [59] J.-H. Kim, S. Aghaeimeibodi, J. Carolan, D. Englund and E. Waks, *Hybrid integration methods for on-chip quantum photonics*, *Optica* **7**, 291 (2020).
- [60] M. Ruf, M. Weaver, S. van Dam and R. Hanson, *Resonant Excitation and Purcell Enhancement of Coherent Nitrogen-Vacancy Centers Coupled to a Fabry-Perot Microcavity*, *Physical Review Applied* **15**, 024049 (2021).
- [61] A. Reiserer and G. Rempe, *Cavity-based quantum networks with single atoms and optical photons*, *Reviews of Modern Physics* **87**, 1379 (2015).
- [62] E. Janitz, M. K. Bhaskar and L. Childress, *Cavity quantum electrodynamics with color centers in diamond*, *Optica* **7**, 1232 (2020).
- [63] J. D. Joannopoulos, S. G. Johnson, J. N. Winn and R. D. Meade, *Photonic Crystals: Molding the Flow of Light - Second Edition*, in *Photonic Crystals* (Princeton University Press, 2011).

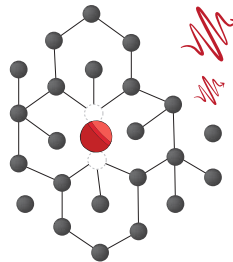
- [64] E. Janitz *et al.*, *Fabry-Perot microcavity for diamond-based photonics*, *Physical Review A* **92**, 043844 (2015).
- [65] J. Benedikter *et al.*, *Cavity-Enhanced Single-Photon Source Based on the Silicon-Vacancy Center in Diamond*, *Physical Review Applied* **7**, 024031 (2017).
- [66] K. Kuruma *et al.*, *Coupling of a single tin-vacancy center to a photonic crystal cavity in diamond*, *Applied Physics Letters* **118**, 230601 (2021).
- [67] A. E. Rugar *et al.*, *Quantum Photonic Interface for Tin-Vacancy Centers in Diamond*, *Physical Review X* **11**, 031021 (2021).
- [68] A. Sipahigil *et al.*, *An integrated diamond nanophotonics platform for quantum-optical networks*, *Science* **354**, 847 (2016).
- [69] M. K. Bhaskar *et al.*, *Experimental demonstration of memory-enhanced quantum communication*, *Nature* **580**, 60 (2020).
- [70] P. Türschmann *et al.*, *Coherent nonlinear optics of quantum emitters in nanophotonic waveguides*, *Nanophotonics* **8**, 1641 (2019).
- [71] M. L. Chan *et al.*, *On-chip spin-photon entanglement based on photon-scattering of a quantum dot*, *npj Quantum Information* **9**, 1 (2023).
- [72] M. Pasini *et al.*, *Nonlinear Quantum Photonics with a Tin-Vacancy Center Coupled to a One-Dimensional Diamond Waveguide*, (2023), arxiv:2311.12927 [quant-ph] .
- [73] M. Arcari *et al.*, *Near-unity coupling efficiency of a quantum emitter to a photonic-crystal waveguide*, *Physical Review Letters* **113**, 093603 (2014), arxiv:1402.2081 [physics, physics:quant-ph] .
- [74] H. Thyrestrup *et al.*, *Quantum Optics with Near-Lifetime-Limited Quantum-Dot Transitions in a Nanophotonic Waveguide*, *Nano Letters* **18**, 1801 (2018).



3

FROM BULK DIAMOND TO SNVs IN WAVEGUIDES

In this chapter, we go through the steps from ion implantation of tin in bulk diamond to integration in nanophotonic waveguides. First, we review different methods for fabricating a bulk diamond sample with SnV centers, discussing the optical properties and stability when the SnV is embedded in the diamond crystal. Then, we introduce the theory of waveguide-QED and simulate the expected coupling for SnV centers in a single-mode diamond waveguide. Finally, we characterize the waveguide devices.



3.1. SAMPLE: SNV FABRICATION

Tin atoms are not a native impurity in diamond, as opposed to Nitrogen. Thus, to obtain SnV centers the substrate needs to be doped. A method for incorporating Sn atoms during CVD diamond growth is not yet available. Currently Sn-doping is only possible by ion implantation.

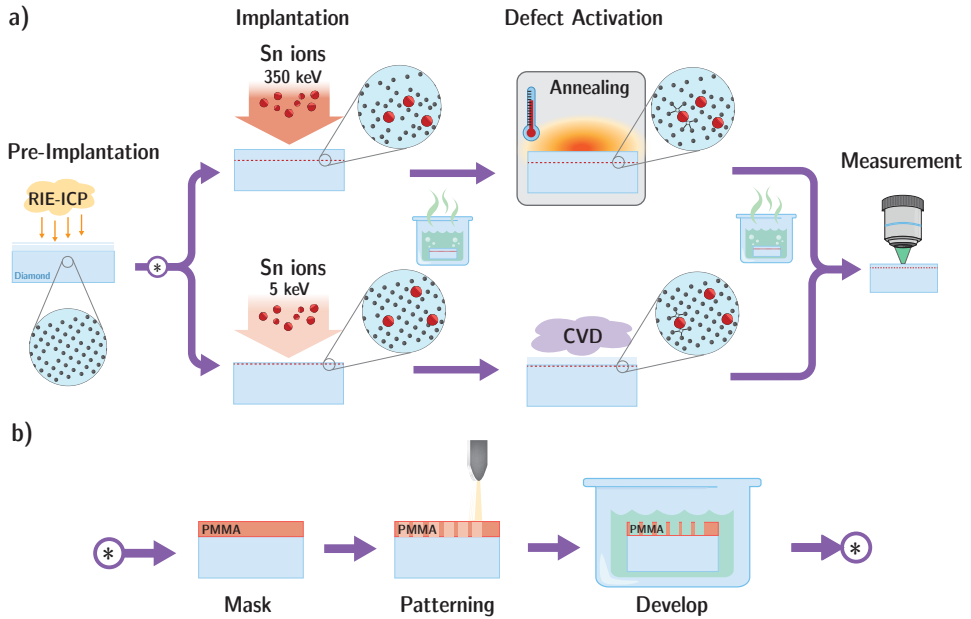


Figure 3.1: **Sample Implantation Process Flow.** (a) Starting from a polished and acid-cleaned diamond substrate, first we perform a pre-implantation etch of the top $\sim 10\mu\text{m}$ of diamond using RIE-ICP to remove polishing-induced strain. Following, we implant Sn ions. The ion energy is chosen according to the target implantation depth. The diamond substrates are cleaned using a boiling tri-acid solution (see text for details) and undergo a defect activation step. This step also mitigates the implantation-induced damage. After the activation step, the sample is cleaned again. In particular for thermal annealing, this step can be used to remove the graphite layer that can form on the diamond surface during high-temperature treatments. (b) Before the implantation, the sample can be masked to obtain spatially localized color centers. The mask material (in this case PMMA) is first spun on the sample, then patterned, and finally developed.

ABOUT ION IMPLANTATION

The SnV centers should be optically (and spin) coherent and have stable optical transitions. These properties are related to the quality of the surrounding crystalline environment and the presence of other defects. Ion implantation can cause severe crystal damage, considering that ^{120}Sn is a much heavier and bigger atom than ^{12}C and requires high energy to reach considerable depth (in the range of tens to hundreds of keV for few tens of nm). The estimated yield of conversion from Sn ion to SnV center with currently available methods is $\sim 1 - 5\%$ [1, 2]. Therefore, a high

ion implantation density is necessary to obtain a target SnV density in a specific location.

Implantation damage, together with the initial crystalline quality of the substrate, contributes to variations of the local strain environment, which can partly be quantified by the inhomogeneous distribution of the optical transitions. Each SnV will experience a different strain and therefore have a different transition frequency. The inhomogeneous distribution should, in general, be at least comparable with the range of the available tuning mechanism (as introduced in Section 2.2.4), which for SnV centers can be few GHz by second-order Stark tuning or in the range of hundred pm with strain tuning. Deterministic positioning and localization of color centers are generally desirable when considering nanophotonic integration. Control on the SnV density is sufficient to ensure coupling to the optical mode of waveguides, but in nanophotonic cavities some control of the spatial position in all three dimensions is ideal.

3.1.1. HIGH ENERGY IMPLANTATION

Implanting Sn ions with high energy (\sim hundreds keV) is the most straightforward approach. The process flow implemented in our group follows the top part of Fig. 3.1(a). The sample fabrication process starts with pre-implantation surface treatment of a polished diamond substrate. The sample substrate is first cleaned in a wet Piranha (ratio 3:1 of H_2SO_4 (95%) : H_2O_2 (31%)) inorganic solution for 20 min at 80°C , followed by the superficial $\sim 5\ \mu\text{m}$ etching via inductively-coupled-plasma reactive-ion-etching (ICP/RIE) Ar/ Cl_2 plasma chemistry based recipe to remove the residual polishing induced strain from the surface of the substrate. An additional $\sim 5\ \mu\text{m}$ ICP/RIE O_2 chemistry-based plasma etch is performed to remove residual chlorine contamination from the previous etching step [3]. Following this, the sample is again cleaned in a Piranha solution.

The substrate is then implanted with ^{120}Sn ions. The ion energy determines the depth of the SnV-doped layer. This can be calculated with Stopping Range of Ion in Matter (SRIM) [4] simulations. An energy of 350 keV with 7° implantation angle results in a Sn layer that is $88 \pm 16\ \text{nm}$ from the diamond surface. While this is usually an acceptable depth for nanophotonic devices, where the dimensions are usually $\sim 200\ \text{nm}$, the high energy heavy atoms create significant damage to the diamond crystal. From SRIM simulations, with this energy is also predicted that every implanted ion forms ~ 2500 vacancies. The implantation dose, combined with the yield, determines the final SnV density. Typically doses in the range of 10^{10} to 10^{11} ions/ cm^2 guarantee spatially and frequency resolvable single SnVs.

After implantation, there is a critical step of thermal annealing of the substrate. Through thermal annealing, the diamond crystal damage can be partly healed and the vacancies are allowed to diffuse in the crystal. Because the split-vacancy configuration of the SnV is energetically favourable [5], this will tend to be formed when a vacancy combines with an interstitial Sn ion. To enhance the mobility of vacancies and structural changes in the crystal, a high temperature is needed. However, diamond is only a metastable solid phase of carbon at high temperatures and moderate or low pressures, while the

stable one is graphite [6]. That is why thermal annealing often results in graphitization of the diamond surface. In addition, contamination or a non-inert environment, as well as crystallographic defects, can enhance graphitization. To mitigate this, there are two regimes for thermal annealing. In Low-Pressure High-Temperature (LPHT) annealing, the diamond is heated up to $\sim 1100^\circ\text{C}$ in high vacuum. In this regime, diamond is not the stable phase. The vacuum environment helps keep an inert environment and avoid contamination. Any resulting graphite superficial film can be removed after the annealing by cleaning in a boiling tri-acid solution (1(60%) : 1(65%) : 1(95–98%) of $\text{HClO}_4:\text{HNO}_3:\text{H}_2\text{SO}_4$). High-Pressure High-Temperature (HPHT) annealing, instead, uses significantly higher temperatures, $> 2000^\circ\text{C}$, and pressures in the few GPa range to make the process happen close to the regime where diamond is the most stable phase.

3.1.2. SHALLOW ION IMPLANTATION AND GROWTH

One way to reduce the implantation damage is to perform Shallow Ion Implantation and Growth (SIIG) [1]. This is schematically depicted in the lower part of Fig. 3.1(a). After the same pre-implantation treatment, the diamond is implanted with Sn ions at low energy (1 – 5keV), resulting in a Sn-doped layer only a couple of nanometers from the surface. With this energy, the crystal damage due to implantation is minimized. A thin diamond film is then grown on the implanted surface by chemical vapor deposition (CVD). During this overgrowth step, the diamond is heated beyond the temperature that allows diffusion of vacancies, and the crystal damage is further reduced, while at the same time allowing the formation of SnV centers. Two main advantages of this technique are, first, that the final crystal damage can be very low without the need for an additional annealing step, and second, that the depth of the SnV layer can be precisely tuned by controlling the thickness of the overgrown film. The challenge is that this technique requires good control over the CVD process. The concentration of impurities and the structural properties of the cap layer are determined by the details of the CVD process and by the crystalline quality of the seed substrate [7].

3.1.3. CHALLENGES FOR SnV GENERATION

While the current state of the art of SnV fabrication is sufficient for proof-of-principle demonstrations, there are still technical challenges that should be addressed to make SnV devices more scalable and reproducible.

Obtaining spatially localized SnV centers is important to maximize the coupling to nanophotonic structures. Considering the optical mode size, on the order of the wavelength, this requires localization with a precision on the order of tens of nm. One way to control the in-plane localization is to make use of an implantation mask, as illustrated in Fig. 3.1(b). By tuning the implantation density it is possible to have localized spots with a number of Sn atoms characterized by a Poisson distribution. Then, taking into account the probability of Sn-to-SnV conversion, a resulting Poisson distributed number of SnV per spot is obtained.

Another approach is deterministic Focused Ion Beam (FIB) implantation. Using a

FIB column can lead to very precise localization of the atoms. A further advantage of FIB is that it is possible to detect a single ion implantation event by measuring the secondary electron scattering due to the impact. When the detection efficiency of the ion implantation is high, it allows to have deterministic control over the number of implanted ions per spot.

While control on the number of Sn atoms in a spot is beneficial, the low yield of Sn-to-SnV conversion, currently estimated around 1 – 5%, is still a limiting factor. An improvement of the conversion yield is necessary towards deterministic SnV generation and could be achieved with, for example, an extended or higher temperature annealing, local generation of vacancies via electron irradiation or femtosecond laser-induced damage, as well as deterministic local laser annealing [8].

3.2. FINGERPRINT: SnV OPTICAL CHARACTERISATION

3.2.1. SnV IN THE CRYSTAL

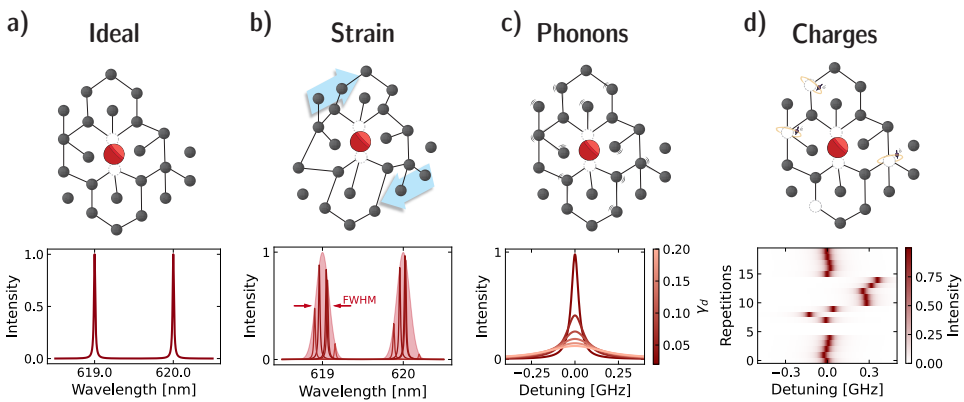


Figure 3.2: **SnV in the Crystal.** In the ideal case (a), the SnV spectrum has well-defined wavelengths for the C and D transitions. However, variations in the local strain environment of the diamond host cause the frequency to be slightly different for each SnV. (b) This results in a distribution of transition frequencies, referred to as inhomogeneous distribution. (c) The optical transition linewidth is broadened by phonon-induced pure dephasing, while noisy charge environment (d) shows up when repeatedly probing the emitter in the form of spectral diffusion and spectral jumps and termination of fluorescence due to charge state change.

The quality of the optical properties and stability of the SnV is largely determined by the quality of the surrounding diamond crystal. Here we consider three main noise sources related to the diamond crystal and their effect on the SnV optical transitions compared to the ideal case depicted in Fig 3.2(a).

STRAIN

Variations in the local strain environment (Fig. 3.2(b)) can be related to the structural properties of the diamond, the presence of crystallographic defects, dislocations, etc.

The Sn ion implantation, especially in case of high energy, results in heavy crystal damage and non-uniform local strain. In addition, the fabrication of devices in diamond can lead to a strained environment for the SnV. Local strain variations cause each SnV to have a different transition frequency, this phenomenon is called inhomogeneous distribution.

PHONONS

As discussed in 2.2.3, phonons are a cause of dephasing in the SnV optical transition (Fig. 3.2(c)). The effect of pure dephasing due to phonon processes alters the frequency content of the emitted photon wavepacket and makes the optical transition broader.

CHARGES

Despite the first-order insensitivity to electric fields, the SnV and other Group-IV still suffer from a noisy local charge environment (Fig. 3.2(d)). Variations in the charge environment are reflected in shot-to-shot variations of the optical transition frequency, a phenomenon known as spectral diffusion.

3.2.2. SPECTRUM AND INHOMOGENEOUS DISTRIBUTION

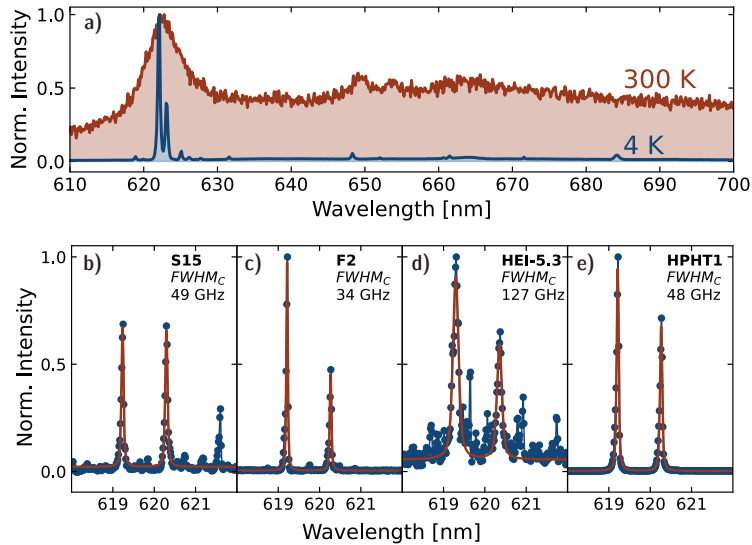


Figure 3.3: SnV Spectrum and Inhomogeneous Distribution. (a) Photoluminescence (PL) spectrum of a SnV sample under off-resonant excitation (532 nm) at room and cryogenic temperatures. (b-e) Inhomogeneous distribution of the C and D transitions in four samples fabricated with different techniques. We report the full width at half maximum of the C-transition distribution for each. (b) S15: Type Ib diamond, <111> oriented, implanted with SIIG method. (c) F2: Type IIa dislocation-free diamond, <111> oriented, implanted with SIIG method. (d) HEI-5.3: electronic grade diamond, <100> oriented, implanted with high energy with LPHT annealing. (e) HPHT1: electronic grade diamond, <100> oriented, implanted with high energy and HPHT annealed.

Figure 3.3(a) shows a photoluminescence (PL) spectrum of an SnV center at room and

cryogenic temperatures. At low temperatures, the C and D ZPL transitions around 620 nm can be resolved. The A and B transitions are not visible due to the low occupation and fast relaxation of the Upper Branch of the Excited State. The PSB extends between ~ 630 and 700 nm.

By looking at four distinct samples, we investigate how the substrate quality and fabrication method affect the inhomogeneous distribution, which is measured by averaging spectra taken on several emitters. Figure 3.3(b-e) shows the inhomogeneous distribution for the four samples.

Samples *S15* and *F2* (Fig. 3.3(b,c)) are fabricated with low energy implantation (Sec. 3.1.2) and subsequent CVD overgrowth of 5 μm and 500 nm, respectively. The diamond substrate has $\langle 111 \rangle$ crystal orientation in both cases but differs in quality. *S15* is a Ib substrate (Syntek) over which an initial CVD film of $\sim 7 \mu\text{m}$ is grown which provides a better chemical purity but similar structural properties as the seed. On the other hand, *F2* is a IIa type diamond that is dislocation-free (FSBI TISNCM). This is realized by HPHT diamond synthesis, post-selection, and laser cutting of an area where no dislocations are visible in X-ray measurements. The full width at half maximum (FWHM) obtained by fitting the inhomogeneous distribution is (49 ± 4) GHz for *S15* and (34 ± 1) GHz for *F2*. The latter is very close to the spectrometer resolution, which is limited to a FWHM of 25 GHz for a single fitted SnV spectrum. This suggests that the original substrate quality can affect the strain environment, but it is still possible to obtain narrow inhomogeneous broadening in the presence of dislocations for low-energy implantation.

Samples *HEI-5.3* and *HPHT1* (Fig. 3.3(d,e)) are implanted with high energy and subsequently annealed as described in section 3.1.1. The substrate is electronic grade $\langle 100 \rangle$ oriented diamond (Element 6), implanted with ^{120}Sn ions at an energy of 350 keV. *HEI-5.3* is annealed at 1100 $^{\circ}\text{C}$ for 8 h in high vacuum, while *HPHT1* is annealed at 2100 $^{\circ}\text{C}$ and pressure in the range of 6-8 GPa for 2 hours. From the spectra, it is clear how the high-energy implantation negatively affects the inhomogeneous distribution. We measure an inhomogeneous FWHM of (127 ± 4) GHz for *HEI-5.3* and of (48 ± 1) GHz for *HPHT1*. The annealing process is crucial for repairing the lattice damage caused by implantation and reducing the strain variations.

These results suggest that the structural properties of the native diamond crystal do have an impact on the inhomogeneous distribution, but the main contribution is given by implantation damage at high energies and how effectively it can be improved by annealing. In a practical application, it is useful to find a trade-off between a narrow inhomogeneous distribution, within the tuning range and giving a higher probability of finding SnVs with similar frequencies, and the presence of some strain which would allow microwave driving or higher operation temperature. Finally, it is good to mention that we have not observed a clear correlation between inhomogeneous distribution and stability of the optical transitions.

3.2.3. SINGLE SNV OPTICAL FINGERPRINT

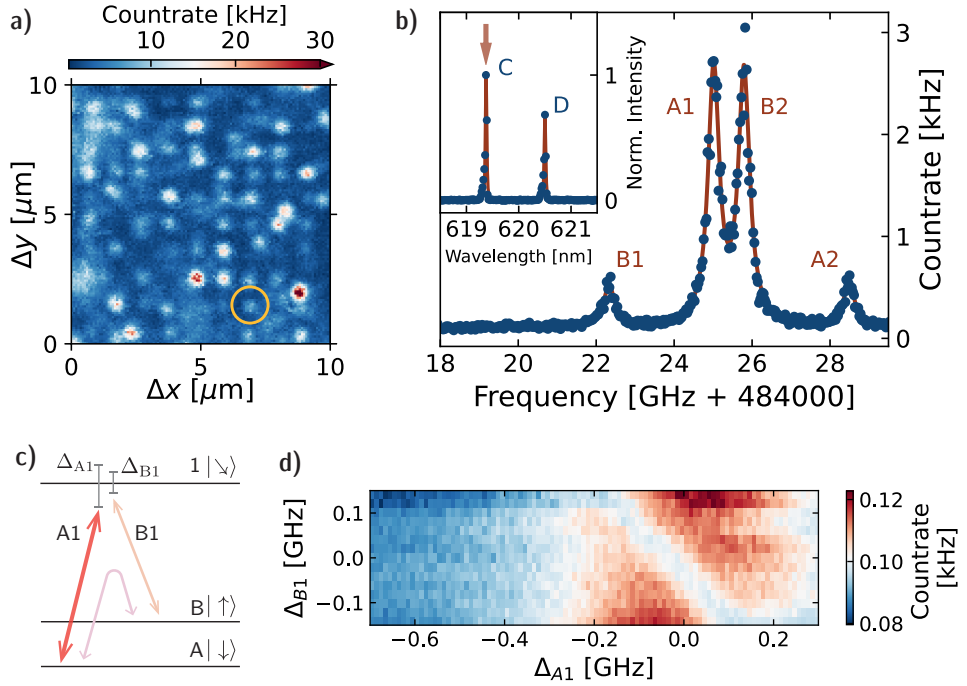


Figure 3.4: **Fingerprint of a single SnV center and Coherence Population Trapping.** (a) Confocal map of an array of Sn implanted spots. In the orange circle, we perform (b) a PL spectrum (inset) showing the C and D transitions for a single SnV. In the C transition, indicated with a red arrow, we perform a PLE scan that shows the four spin-flipping (A2, B1) and spin-conserving (A1, B2) transitions under an external magnetic field (180 mT and 109° angle with respect to the symmetry axis). (c) Schematic of the energy levels used for coherence population trapping (CPT) and (d) map of the CPT measurement on a different SnV center. The CPT dip corresponds to a spin coherence $T_2^* = (0.9 \pm 0.1)$ ns [9].

To show the optical signature of a single tin-vacancy, we fabricate a sample with an array of spots containing on average ~ 1 SnV each. This sample follows the same fabrication steps of sample S15 (see previous section). Before the implantation step, we mask the sample (see Fig. 3.1 and Sec. 3.1.2) with PMMA and pattern an array of circular holes. The implantation density for this sample is 10^{11} ions/cm 2 . Considering a Sn-to-SnV conversion yield between 1 and 5%, holes of 125 nm diameter will have an average occupation of 0.5 to 2 SnVs per hole. Figure 3.4(a) shows a confocal map of the 125 nm holes array, while exciting with off-resonant light (532 nm) and collecting SnV ZPL light (600-625 nm). Several spots showing fluorescence in the SnV ZPL range are visible.

Focusing on the spot in the orange circle, we obtain a PL spectrum and a photoluminescence excitation (PLE) scan of a single SnV (Figure 3.4(b)). This measurement is taken with an external magnetic field of 180 mT along the $\langle 111 \rangle$ growth direction of the sample. This specific SnV has its symmetry axis along one of the other equivalent $\langle 111 \rangle$ diamond directions, resulting in an angle of 109° with the magnetic field. The

low cyclicity of the optical transitions, probably caused by the strongly misaligned field, allows to clearly see the spin-flipping transitions B1 and A2, along with the brighter spin-conserving transitions B2 and A1. From these PL and PLE scans it is possible to extract two quantities of interest: the ground state splitting Δ_{GS} and the frequency of the qubit ω_Q . In this case, we have $\Delta_{GS} = 878$ GHz indicating little strain and $\omega_Q = 2.70$ GHz.

With the spin-flipping transitions being weakly allowed, we can test the optical driving of the spin state. On a similar SnV center in the same sample, we realize a coherence population trapping experiment (CPT) [10]. We form a "Λ-scheme" using the A1 and B1 transitions (Fig. 3.4(c)): while scanning the laser frequency around the B1 transition, we scan over A1 a sideband generated using an electro-optic phase modulator. When the frequencies of the two driving fields meet a two-photon resonance condition, the system is pumped into the state

$$|D\rangle = \cos\theta|A\rangle - \sin\theta|B\rangle, \quad (3.1)$$

where $\theta = \Omega_{A1} / \Omega_{B1}$ is the ratio of the Rabi driving frequencies of the two fields. The $|D\rangle$ state does not have contributions from the excited state and it shows up as a dip in the PSB fluorescence count rate. From the dip, it is possible to extract the spin coherence. From a fit to a master equation model we find the coherence time to be $T_2^* = (0.9 \pm 0.1)$ ns [9]. This value is quite modest, we attribute this to excess heating which keeps the sample at a higher temperature than the nominal value of 3 K or to other dephasing sources that could be related to defects in the CVD diamond due to the native Ib substrate. These are consistent with the broad linewidth of the optical transitions of 350 MHz, around 10 times the transform-limited linewidth. However, the CPT is visible and it is a first step toward optically driving the spin transition.

3.2.4. PHONON INDUCED LINewidth BROADENING

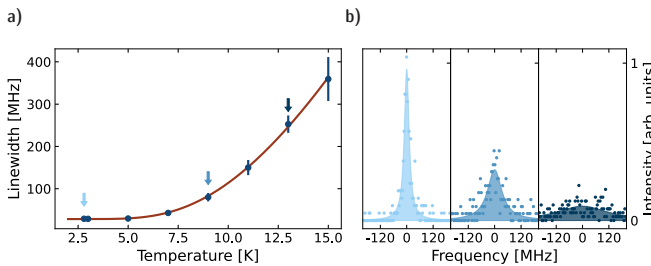


Figure 3.5: **Temperature dependence of the linewidth.** (a) SnV single scan linewidth as a function of temperature. The red curve is a fit using equation 2.15 for temperature-dependent phonon broadening. (b) Three single scans, marked with arrows in (a), show phonon broadening. The shaded area is a Lorentzian fit.

As introduced in section 2.2.3, temperature-induced phonon processes can cause dephasing of the optical transition, which manifests as increasing transition linewidth at higher temperatures. Figure 3.5 shows the linewidth dependence on temperature for a

single SnV. In this regime, where direct phonon processes start to become relevant, we expect the linewidth to behave according to the phonon transition rate. The solid red line is a fit with equation 2.15, showing very good agreement.

3.2.5. STABILITY AND REPUMPING METHODS

Defects, doping, and surface treatments can alter the electronic landscape and the local Fermi Level of the diamond, on which the stability of a certain charge state of the SnV depends. Similarly to other color centers, the SnV^- is known to undergo charge state change and termination of fluorescence under resonant excitation. Experiments on implanted and HPHT annealed diamond [12] suggest that the underlying mechanism is a one-photon process that takes place from the excited state of the SnV^- , promoting an electron from the valence band to the SnV ground state and ionizing the center to the optically inactive SnV^{2-} state.

The charge state can be initialized by inducing charge mobility, usually through a high-energy off-resonant light pulse. This modifies the surrounding charge environment and probabilistically brings the SnV to the singly negatively charged state. At the same time, it stochastically changes the charge occupation of nearby traps and defects and creates a different electronic environment every time. If the charges are close to the SnV, this can result in spectral diffusion and spectral jumps up to a few hundred MHz despite the first-order insensitivity to electric fields.

We use a green laser (wavelengths of 532 or 515 nm) for the off-resonant "repump" pulse. Figure 3.6(a) shows repeated PLE scans over a single SnV center [11]. After each scan, we can define the state of the emitter compared to a set frequency as *on-resonance*, *off-resonance*, or *dark*. If the state is dark, meaning that the maximum count rate in the scan is below a set threshold, we apply a green repump pulse to probabilistically initialize the charge state before the next scan. Three aspects of the behavior of the emitter are interesting to note. First, when the emitter is on resonance and does not ionize (i.e. several consecutive *on-resonance* scans), there is almost no visible spectral diffusion. Second, the SnV ionization and the reset of the correct charge state with a repump pulse are probabilistic. Finally, when the charge state is reset after a repump pulse the emitter can jump in frequency. For this SnV, the scan shows the presence of a second "frequency state" of the emitter around 100 MHz detuned, which could be caused by one close-by charge trap whose state can change at every repump pulse. Though green is an established choice for repumping diamond color centers, some studies showed that the use of a blue laser (~450 nm) can ionize some surrounding defects more efficiently [12] therefore creating a more consistent charge environment at every repump. This scan depicts well the behavior of a "typical good SnV" in our samples, however, the stability of each specific SnV is strongly dependent on the surrounding environment.

Spectral diffusion, including that which is repump-induced, can be circumvented by employing a Charge-Resonance Check (CR-Check) routine [11]. This consists of a check that the SnV is in an optically active charge state and in resonance with a set frequency, realized by probing the SnV transition at the required frequency. A threshold in the num-

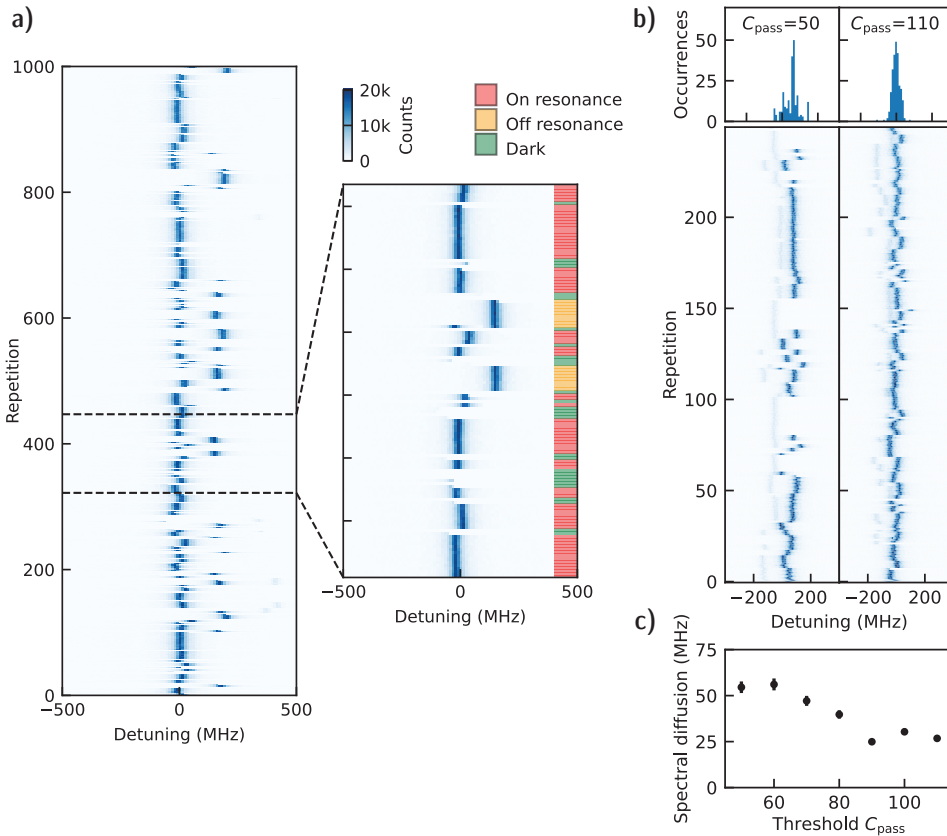


Figure 3.6: **Charge State Repump.** (a) Repeated PLE scans on a single SnV, with an off-resonant repump pulse conditioned on the previous scan having a peak. We can define three states for the SnV whether it is in at the desired frequency (on-resonance), at a different frequency (off-resonant), or in a different charge state (dark). (b) Comparison of repeated PLE scans conditioned on passing a Charge-Resonance Check before the scan, with thresholds of 50 and 110 detected counts. The additional line visible in the scans is probably related to a second SnV center in the surroundings. (c) Width of the spectral diffusion distribution at varying CR-Check threshold. Adapted with permission from [11].

ber of counts collected during the probe pulse can be used to discriminate whether the emitter is optically active and in resonance with the probe laser or not. In case the number of counts is lower than the threshold, one can either apply a repump pulse or try probing again. A successful CR-Check can be used to trigger an experimental sequence, thus ensuring the *on-resonance* condition for the emitter. Figure 3.6(b) shows two series of scans on the same emitter as in (a), in this case, pre-conditioned on passing a CR-Check with thresholds C_{pass} of 50 and 110 counts. The spectral diffusion distribution becomes narrower when increasing the threshold, as can also be seen in Fig. 3.6(c).

3.3. INTEGRATION: SNV IN WAVEGUIDES

3.3.1. EFFECTS OF WAVEGUIDE-QED

We introduced in Section 2.3 the basic concepts of waveguide-QED, here we focus on the physical effects that can be measured and practically used in quantum science experiments.

Single Photon Interaction. In the ideal case, a single photon in a traveling optical mode that is coupled to an emitter with $\beta = 1$ (see Eq. 2.24), interacts inducing a full Rabi cycle of the optical transition and acquiring a phase. The part of the wavefunction that describes the transmission in the waveguide can be split into a state of the photon directly transmitted forward and a state of the photon interacting and being re-emitted in the forward mode. Due to the interaction phase, these two components destructively interfere. The only possible state is then the photon interacting and being scattered in the reflected mode: the two-level system acts as a perfect single photon mirror [13, 14].

This is observable as a dip in the transmitted signal when in resonance with the emitter. With $\beta < 1$, meaning that the photon only interacts with the emitter with a finite probability, the interference is not perfect and the photon can be transmitted. In this case, the contrast of the dip in transmission is decreased. Pure dephasing of the optical transition reduces the coherence of the interacting photon, thus also reducing the interference effect and allowing for more transmission. The timescale of the coherent interaction is the excited state lifetime τ . Increasing the average number of photons per lifetime at the emitter, n_τ , will saturate the effect and increase the transmission, since the reflection is a single-photon process.

The transmission coefficient, accounting for all these effects, can be calculated starting from the emitter dynamics and input-output relations to be [15]:

$$t(\omega) = 1 - \frac{\beta}{\left(1 + \frac{n_\tau}{n_c}\right) \left(1 + 2\frac{\gamma_{\text{deph}}}{\gamma} - i2\frac{\omega}{\gamma}\right)}. \quad (3.2)$$

Here γ is the total decay rate of the emitter, γ_{deph} is the pure dephasing rate, and ω is the detuning of the input photon frequency compared to the emitter transition frequency. The factor n_c is the critical number of photons per lifetime, defined as

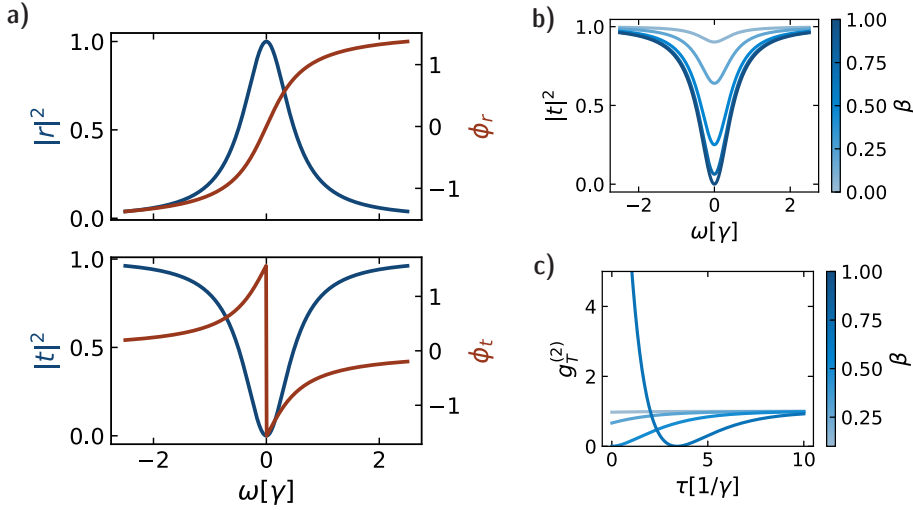


Figure 3.7: **Waveguide-QED Effects.** (a) Reflection (top) and transmission (bottom) coefficients for $\beta = 1$. (b) Transmission extinction for varying coupling β . (c) Photon correlations of the transmitted field for varying β .

$$n_c = \frac{1 + 2\beta \frac{\gamma_{\text{deph}}}{\gamma}}{4\beta^2} \quad (3.3)$$

which indicates the photon flux regime where the interaction saturates. Experimentally, the contrast of the extinction of the transmission signal through the waveguide can be used to quantify the coupling factor β .

The reflection coefficient (for $n_t \ll n_c$) is simply a lorentzian, given by

$$r(\omega) = \frac{\beta}{1 + 2\frac{\gamma_{\text{deph}}}{\gamma} - i2\frac{\omega}{\gamma}}. \quad (3.4)$$

Notably, if the input wavepacket is spectrally narrow compared to the Lorentzian spectrum of the emitter (e.g. it is longer than the excited state lifetime), the coherently reflected photons maintain the spectral and coherence properties of the input field. The transmission and reflection spectra can be obtained as $T = |t|^2$ and $R = |r|^2$ and are shown in Fig. 3.7(a) together with the phase $\phi_{t,r} = \arg(t, r)$.

Multiphoton Interaction. Experimentally, often the input field is not composed of single photons but rather a weak coherent state (WCS) obtained by attenuating laser light such that the probability of multiphoton components is small:

$$|\psi_{\text{WCS}}\rangle \propto |\text{vac}\rangle + \alpha|1\rangle + \frac{\alpha^2}{\sqrt{2}}|2\rangle + O(\alpha^3) \quad (3.5)$$

where α is the complex amplitude of the coherent state. The multiphoton components interact with the emitter in a non-trivial way [14, 16].

Consider a two-photon state at the waveguide input, in a simple picture we can divide the interaction into two cases. The two photons can interact independently with the emitter, this will result in the photons being separately reflected or directly transmitted if the coupling is not ideal. This last case is referred to as the "plane wave" component of the forward scattered field [16]. If the coupling is significant, the two photons can interact collectively. Effectively, one photon excites the emitter and the second triggers stimulated emission in the forward direction. The result is a strongly correlated two-photon bound state that is perfectly transmitted. This picture holds for higher photon numbers, where strong coupling of the emitter to the waveguide can result in the transmission of multi-photon bound states. The transmitted field is a combination of the plane wave and bound states components, which vary at different coupling strengths. For $\beta \ll 1$ there is almost no bound state contribution, as the interaction is weak. For increasing β the bound state contribution becomes dominant, this results in a strongly bunched photon statistics of the transmitted field. The $g^{(2)}$ of the transmitted field at low powers is described by [13]

$$g_{TT}^{(2)}(\tau) = e^{-\gamma\tau} \left(\frac{\beta^2}{(1-\beta)^2} - e^{\frac{\gamma\tau}{2}} \right)^2 \quad (3.6)$$

with γ the spontaneous decay rate of the emitter. Fig 3.7(c) shows the behavior of the photon correlation in the transmitted field, $g_{TT}^{(2)}$, for different coupling strengths. At low β the interference between the dominant plane wave contribution and the bound state results in antibunching, with perfect interference of the two components for $\beta = 0.5$ leading to $g_{TT}^{(2)}(0) = 0$. At higher β , the bound state becomes the leading contribution yielding strong bunching at $\tau = 0$. The bunching effect is followed by antibunching at a delayed time also arising from interference between the plane wave and bound state terms. The reflected field does not contain any contribution of the incident field but only the scattering from the emitter, whose single-photon nature results in perfect antibunching, $g_{RR}^{(2)}(0) = 0$.

Sources of Noise. Several effects cause the SnV optical transition to deviate from the ideal two-level system behavior. Pure dephasing causes decoherence of the interaction, which apart from allowing photon transmission also causes spectral broadening of the reflected photon. The spectrum of the reflected photons will be a combination of the narrow coherently scattered field and a dephasing-induced incoherent part with the width given by γ_{deph} . The finite efficiency of the SnV transition given by the combination of QE, DW, and BR limits the emission rate in the waveguide mode, reducing the factor from the ideal β to an effective coupling

$$\beta_{\text{eff}} = (QE \times DW \times BR) \times \beta_{\text{ideal}}. \quad (3.7)$$

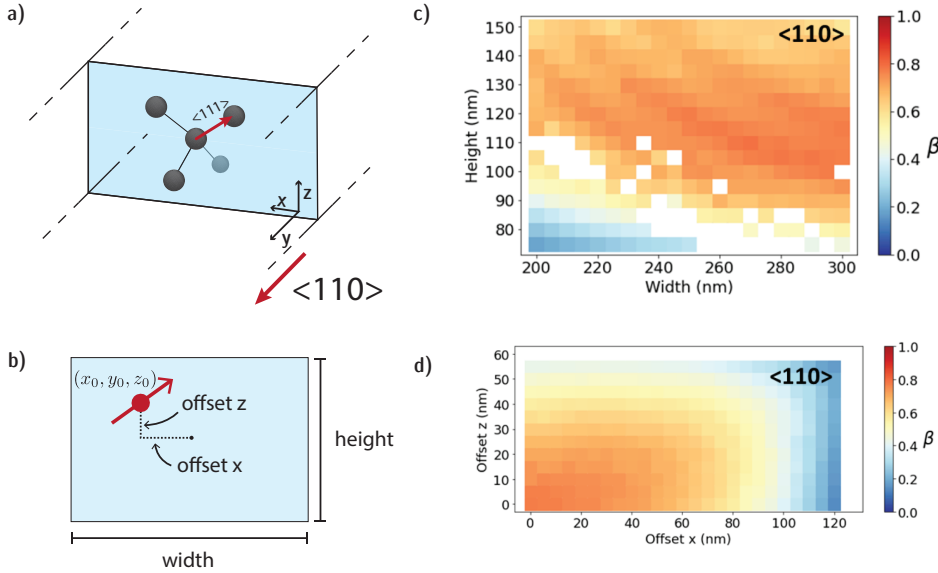


Figure 3.8: **Simulation of Waveguide Geometry and Coupling.** (a) Orientation of the SnV symmetry axis compared to the waveguide direction. (b) Schematic of the simulation parameters. (c) Dipole coupling for different waveguide sizes. (d) Dipole coupling for a waveguide of 250×120 nm at varying SnV positions. Figures (c) and (d) are adapted from [17].

3.3.2. SNV-WAVEGUIDE COUPLING

The decay rate of a transition dipole in a waveguide γ_{wg} , which determines the coupling β , depends on the waveguide geometry and the position of the dipole compared to the electric field distribution of the optical mode. To obtain the optimal waveguide design, we can use finite element methods simulations to extract the expected maximum β .

We consider rectangular cross-section, air-cladded diamond waveguides, as they are compatible with our fabrication process. The dipole of the C-transition is along the symmetry axis of the SnV. Its orientation with respect to the waveguide optical mode is constrained by the orientation of the diamond substrate and the direction of the waveguide. Our fabrication recipe is optimized for $\langle 100 \rangle$ oriented diamond substrates. In this setting, the best coupling of a dipole to a transverse electric mode (TE), where the electric field is perpendicular to the propagation direction, is obtained for a waveguide oriented along the $\langle 110 \rangle$ direction of the diamond crystal. Two of the four possible SnV orientations will be on the electric field plane, with a 54.25° angle from the vertical axis of the waveguide, as shown in Figure 3.8(a). These two directions will optimally couple to TE modes when the SnV is positioned at the center of the waveguide.

Using COMSOL[®] Multiphysics we simulate the coupling of an electric dipole to the waveguide, following the approach of Ref. [15]. The coupling factor β for a mode m can be computed as the ratio between the power of an electric dipole radiated in the waveguide

uide mode m over the total power. Since the power is given by $P = \frac{\omega}{2} \text{Im}[\vec{d} \cdot \vec{E}_m]$, where ω is the dipole oscillation frequency, $\vec{d} = d \cdot \vec{n}$ the dipole moment oriented in the direction \vec{n} and \vec{E}_m the electric field of the mode, we can write

$$\beta_{\text{ideal}} = \frac{\text{Im}[E_{m,\vec{n}}(x_0, y \rightarrow \infty, z_0)]}{\text{Im}[E_{m,\vec{n}}(x_0, y_0, z_0)]} \quad (3.8)$$

where $E_{m,\vec{n}}$ is the projection of the electric field of mode m along the dipole direction, and (x_0, y_0, z_0) is the position of the dipole in the waveguide. To obtain the field amplitude at $y \rightarrow \infty$ we simulate a waveguide of a few μm length and we analyze the field several wavelengths away from the dipole position. We fit the field with two cosines to separate the TE mode from the contributions of other modes (e.g. the TM mode that is excited when the dipole is not at the center of the waveguide). Figure 3.8(c) shows the dipole coupling for different sizes of the waveguide and the dipole at the center of the waveguide. We find a maximum β of 0.79 [17].

We only have partial control over the position of the SnV in the waveguide. Because of the uniform ion implantation over the sample, the lateral offset (x) is randomly distributed for different centers. The vertical offset (z) is set by the implantation energy, which determines the depth of the SnV layer with uncertainty given by the ion straggle. A 88 nm deep SnV layer obtained by high energy implantation has an uncertainty of 16 nm. To account for these effects, we simulate the coupling when the dipole is offset compared to the waveguide center. Figure 3.8(d) shows the coupling to a 250×120 nm waveguide, the geometry with the best expected coupling. The coupling decreases when moving away from the center, but there is an offset range of tens of nm from the center where $\beta > 0.5$ showing that the coupling is robust against misalignment of the emitter. We discussed in 3.1 some ways of fabrication samples with localized implantation. Here precision in the localization on the order of 50 nm, which can easily be obtained with masked implantation, would still yield coupling close to the optimal value.

3.3.3. SETUP AND FIBER COUPLING

We design our waveguides with tapered ends and we couple light in and out by using tapered optical fibers. The fabrication of the tapered optical fibers follows the approach in [18]. We strip the coating of a commercial optical fiber (Thorlabs 630-HP). After a two-step ultrasonic cleaning in acetone and isopropanol (IPA) to remove residues of the coating, we submerge the stripped part of the fiber in hydrofluoric acid (HF, 40% concentration), and with a motorized actuator, we pull the fibers out at a speed of $0.4 \mu\text{m/s}$. The HF etch lasts for 1 h and 45 min, after which the fiber tips result in conical tapers. We use two different approaches for fiber coupling. The first one is adiabatic coupling by evanescent field, which has reported coupling efficiencies up to $\sim 90\%$ [18, 19]. Alternatively, we can use the lensing effect of the fiber taper to focus light into the waveguide. This method has the advantage that does not need contact between the fiber and the waveguide and works also when the fiber tapered tip is damaged or not thin enough for having significant evanescent coupling. Using this method we consistently measure a total fiber-waveguide-fiber coupling efficiency of $\sim 4\%$, which means an average $\sim 20\%$ per coupling.

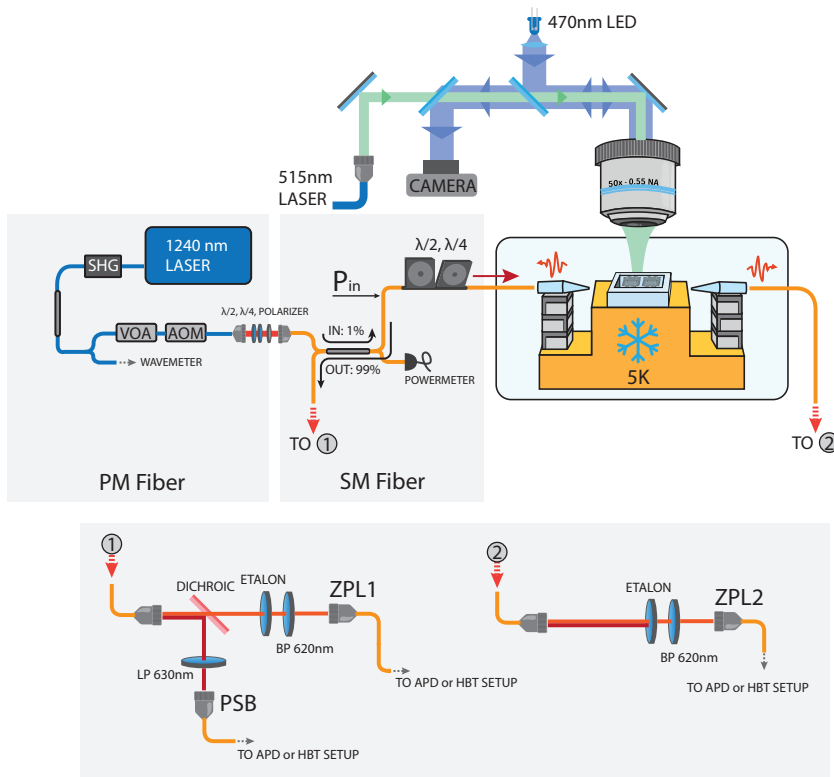


Figure 3.9: **Experimental Setup.** See text for details.

Figure 3.9 shows a schematic of our experimental setup for waveguide experiments. The sample is cooled to 5 K in a closed cycle cryostat (Montana Instruments s50), together with two XYZ piezopositioner stacks (Attocube Systems ANPx51, ANPz51) which allow for control of the position of the optical fibers. This allows probing the waveguides in transmission. We image the sample through an optical window in the cryostat using a long working distance objective (Mitutoyo 50X Plan Apochromat, NA: 0.55, WD: 13 mm), which combined with an LED at ~ 470 nm provides enough resolution to image the waveguides and the fiber tip. Through the same objective, we deliver the repump laser pulses (Cobolt MLD-06 515 nm). The resonant excitation and the photon collection are via fiber. A tunable 1240 nm laser (Toptica DL Pro - TA) pumps a second harmonic generation fiber-coupled crystal (AdvR) to generate tunable laser light around 620 nm. Part of the red output is sent to a wavemeter (High Finesse WS8) for frequency stabilization through a PID loop running in the background and feeding back to the DL Pro controller to tune the IR frequency. The light used for resonant excitation goes through a manual Variable Optical Attenuator (VOA) and an Acousto Optical Modulator (AOM) used to generate pulses. A short fiber-free-space-fiber module (Thorlabs FiberBench)

with polarization control is used to bridge between polarization maintaining (PM) fiber of the laser control and the single mode (SM) fiber used in the rest of the experiment. A 99:1 beam splitter is used to send 1% of the laser light to the input fiber, where we use motorized polarization paddles to control the input polarization. The remaining 99% is used for calibration and monitoring. The reflected light goes through the beam splitter and is collected in the 99% return port. We have two free-space setups for filtering and detection of the light. In the first, usually connected to the reflection port, a dichroic filter (Semrock FF625, short pass ~ 620 nm) separates the PSB and ZPL light. The PSB is further filtered by a Band Pass filter (620 ± 5 nm) and a tunable narrow etalon filter (LightMachinery, ~ 45 GHz FWHM) to get rid of the D-transition. In the PSB path, we further filter the excitation laser with two Long Pass tunable filters set approximately at 630 nm. The second free-space stage only has the 620 nm bandpass and the etalon to filter around the ZPL. The collected photons are fiber-coupled and sent to avalanche photodiode (APD) single photon detectors (Lasercomponents COUNT) or to a Hanbury-Brown-Twiss (HBT) setup realized with a 50:50 fiber beam splitter and two APDs for correlation measurements. We run the experiment using custom software based on the QMI [20] package (version 0.41.0).

3.3.4. CHARACTERISATION OF SNV IN WAVEGUIDES

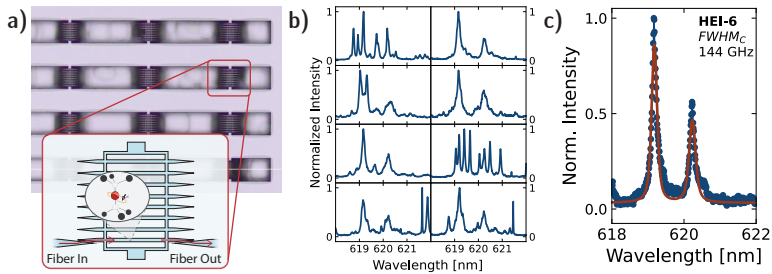


Figure 3.10: **Waveguide Characterisation - PL Spectrum.** (a) Optical microscope image of the sample, each slot contains a chip device with eight waveguides in the geometry depicted in the schematic. (b) PL spectra in eight waveguides belonging to the same chip. (c) Inhomogeneous distribution was obtained by combining PL spectra from 83 waveguides in different chips.

The sample we investigate consists of several diamond chip devices with eight waveguides each, connected to the bulk by support structures, as depicted in Fig. 3.10(a). We first investigate the PL spectrum of the waveguides by shining continuous off-resonant light from the free-space objective and collecting through the tapered fiber the SnV emission in the waveguide. Figure 3.10(b) shows spectra collected from the eight waveguides of one chip. Each waveguide contains several SnV centers. By combining PL spectra of 83 waveguides from different devices we obtain the inhomogeneous distribution spectrum of Fig. 3.10(c), with a FWHM of the C-transition distribution of 144 GHz. This value is in line with results on high-energy implanted samples with LPHT annealing, indicating that the fabrication and the device do not introduce significant additional strain. This sample was implanted with Sn ions at 350 keV with a dose of 10^{11} ions/cm², and annealed at 1200 °C for 5 hours.

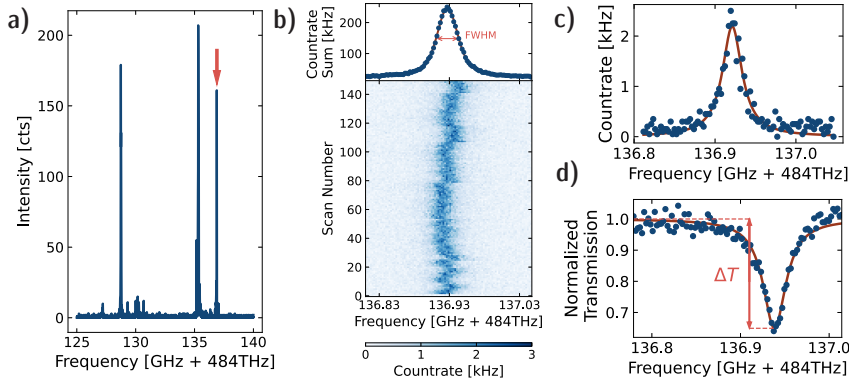


Figure 3.11: **Waveguide Characterisation - PLE.** (a) PLE scan showing several SnVs coupled to the waveguide. (b) Repeated PLE on a single SnV (red arrow in (a)). In this scan, no repump pulse is applied. On top, the sum of all scans shows low spectral diffusion. (c) Single line scan showing narrow, almost transform-limited linewidth. (d) Transmission extinction due to coherent interaction between the input laser and the SnV.

We focus on one waveguide to test the stability and optical properties of the SnV centers. We probe the emitter with a resonant laser through the input fiber, and we collect the PSB photons through the same fiber with a 99 : 1 beam splitter. From the broad PLE measurement in Figure 3.11(a), we see several peaks belonging to different SnVs. We repeatedly scan the transition, using the same conditional repump scheme as in Fig 3.6(a). Figure 3.11(b) shows a typical scan. This SnV shows good stability and spectral diffusion close to the natural linewidth, with an integrated FWHM of (35.8 ± 0.2) MHz. Looking at a single scan (Fig. 3.11(c)) we see that the linewidth is (29 ± 1) MHz, close to the transform-limited value, indicating that the optical transition is coherent and that dephasing and other broadening mechanisms are moderate. Using the second fiber, coupled to the other end of the waveguide, we probe the transmission. Again, we repeat many PLE scans at low input laser power to have a WCS. By integrating over all scans, we obtain the transmission spectrum in Figure 3.11(d), which shows an extinction of the transmission of $\Delta T = 1 - T = 0.35 \pm 0.01$. We fit this with Eq. 3.2 in the limit where $n_T \ll n_c$ and $\gamma_{\text{deph}} = 0$, this yields a coupling $\beta = 0.194 \pm 0.006$.

3.4. CONCLUSIONS

In this chapter, we showed different methods of Sn ion implantation in diamond samples to generate SnV centers and we reviewed the optical properties and noise sources related to the crystalline and charge environment surrounding the SnVs. Finally, we showed the integration of SnV centers in single-mode diamond waveguides. The coherent and stable SnV optical lines in the waveguide, together with the sizeable coupling that we measure through the extinction of the transmission signal due to a single center, indicate that this is a promising platform for developing an efficient spin-photon interface. This experimental setting allows us to further investigate the interaction between a single SnV and the input field in the waveguide, which we do in the next chapter.

BIBLIOGRAPHY

- [1] A. E. Rugar *et al.*, *Generation of Tin-Vacancy Centers in Diamond via Shallow Ion Implantation and Subsequent Diamond Overgrowth*, *Nano Letters* **20**, 1614 (2020).
- [2] S. D. Tchernij *et al.*, *Single-Photon-Emitting Optical Centers in Diamond Fabricated upon Sn Implantation*, *ACS Photonics* **4**, 2580 (2017).
- [3] M. Ruf, *Cavity-Enhanced Quantum Network Nodes in Diamond*, Ph.D. thesis, Delft University of Technology (2021).
- [4] J. F. Ziegler, M. Ziegler and J. Biersack, *SRIM – The stopping and range of ions in matter (2010)*, *Nuclear Instruments and Methods in Physics Research Section B: Beam Interactions with Materials and Atoms* **268**, 1818 (2010).
- [5] U. Wahl *et al.*, *Direct Structural Identification and Quantification of the Split-Vacancy Configuration for Implanted Sn in Diamond*, *Physical Review Letters* **125**, 045301 (2020).
- [6] F. P. Bundy, *The P, T phase and reaction diagram for elemental carbon, 1979*, *Journal of Geophysical Research: Solid Earth* **85**, 6930 (1980).
- [7] J.-C. Arnault, S. Saada and V. Ralchenko, *Chemical Vapor Deposition Single-Crystal Diamond: A Review*, *physica status solidi (RRL) – Rapid Research Letters* **16**, 2100354 (2022).
- [8] Y.-C. Chen *et al.*, *Laser writing of individual nitrogen-vacancy defects in diamond with near-unity yield*, *Optica* **6**, 662 (2019).
- [9] K. T. Dankers, *Phonon-Induced Dephasing of Tin-Vacancy Centres in Diamond Measured by Coherent Population Trapping*, MSc. Thesis, Delft University of Technology (2021).
- [10] R. Debroux *et al.*, *Quantum Control of the Tin-Vacancy Spin Qubit in Diamond*, *Physical Review X* **11**, 041041 (2021).
- [11] J. M. Brevoord *et al.*, *Heralded initialization of charge state and optical transition frequency of diamond tin-vacancy centers*, (2023), arxiv:2311.11962 [quant-ph].
- [12] J. Görlitz *et al.*, *Coherence of a charge stabilised tin-vacancy spin in diamond*, *npj Quantum Information* **8**, 45 (2022).
- [13] D. E. Chang, A. S. Sørensen, E. A. Demler and M. D. Lukin, *A single-photon transistor using nanoscale surface plasmons*, *Nature Physics* **3**, 807 (2007).
- [14] J. T. Shen and S. Fan, *Coherent photon transport from spontaneous emission in one-dimensional waveguides*, *Optics Letters* **30**, 2001 (2005).
- [15] A. Javadi *et al.*, *Single-photon non-linear optics with a quantum dot in a waveguide*, *Nature Communications* **6**, 8655 (2015).

- [16] H. Zheng, D. J. Gauthier and H. U. Baranger, *Waveguide QED: Many-body bound-state effects in coherent and Fock-state scattering from a two-level system*, Physical Review A **82**, 063816 (2010).
- [17] C. F. Primavera, *Coupling Tin-Vacancy Centres to Diamond Waveguides*, MSc. Thesis, Delft University of Technology (2022).
- [18] M. J. Burek *et al.*, *Fiber-Coupled Diamond Quantum Nanophotonic Interface*, Physical Review Applied **8**, 024026 (2017).
- [19] B. Zeng *et al.*, *Cryogenic packaging of nanophotonic devices with a low coupling loss $\leq 1\text{ dB}$*, Applied Physics Letters **123**, 161106 (2023).
- [20] I. T. Raa *et al.*, *QMI - Quantum Measurement Infrastructure, a Python 3 framework for controlling laboratory equipment*, 4TU.ResearchData (2023).

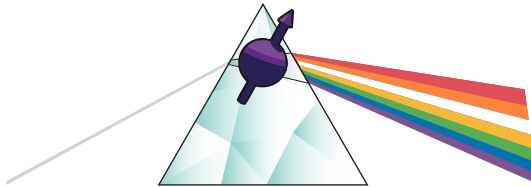


4

NONLINEAR QUANTUM PHOTONICS WITH A SNV CENTER IN A WAVEGUIDE

M. Pasini, N. Codreanu, T. Turan, A. Riera Moral, C. F. Primavera, L. De Santis, H. K. C. Beukers,
J. M. Brevoord, C. Waas, J. Borregaard, R. Hanson

Color centers integrated with nanophotonic devices have emerged as a compelling platform for quantum science and technology. Here we integrate tin-vacancy centers in a diamond waveguide and investigate the interaction with light at the single-photon level. We observe single-emitter-induced extinction of the transmitted light up to 25% and measure the nonlinear effect on the photon statistics. Furthermore, we demonstrate fully tunable interference between the reflected single-photon field and laser light back-scattered at the fiber end and show the corresponding controlled change between bunched and anti-bunched photon statistics in the reflected field.



The results of this chapter are available in pre-print on arXiv:2311.12927

4.1. INTRODUCTION

Nonlinear interactions between single photons and solid-state color centers are at the heart of many applications in quantum science [1, 2] such as the realization of a quantum internet [3, 4]. In particular, color centers in diamond have enabled advanced demonstrations in this direction showing multinode quantum network operation [5, 6], memory-enhanced communication [7] and scalable on-chip hybrid integration [8]. Among the diamond color centers, the tin-vacancy center (SnV) has recently emerged as a promising qubit platform as it combines the inversion symmetry of group-IV color centers [9, 10], allowing for integration in nanophotonic structures, with good optical properties [11–14] and above-millisecond spin coherence at temperatures above 1 K [15, 16]. Devices combining photonic integration with spin and optical control could serve as a future scalable building block for realizing spin-photon gates [17]. On the path towards such scalable on-chip integration, incorporation of emitters into nanophotonic waveguides [12, 18] enables exploration of the emitter-photon interaction and probing of the resulting optical signals both in reflection and transmission.

4

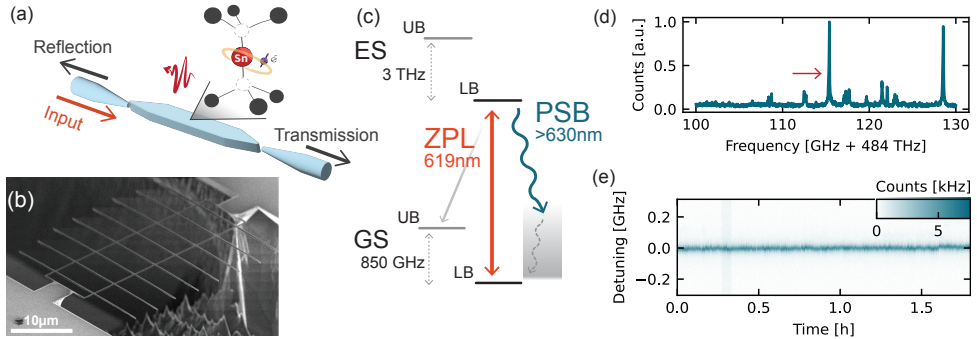


Figure 4.1: Device and optical transition properties. (a) Schematic of the device. We address SnV centers in a nanophotonic diamond waveguide with two tapered ends, which we couple using tapered optical fibers. (b) SEM image of one entire diamond device chip. (c) Energy level scheme of the SnV. At 5 K the SnV spectrum shows two ZPL transitions between the Lower Branch (LB) of the Excited State (ES) to the Lower (Upper) branches (LB, UB) of the Ground State (GS). Here we focus on the ZPL transition between LB of ES and LB of GS at 619 nm, and we filter the other ZPL out. Phonon-assisted decay from the excited state gives rise to a phonon sideband (PSB) with a broad optical spectrum above 630 nm. (d) Photoluminescence excitation in one waveguide showing several SnVs. The red arrow indicates the SnV used for this experiment. (e) Consecutive PLE scans conditioned on the SnV being in the right charge and frequency state. The scanning speed of each PLE is ~ 300 MHz/s.

In this work, we present a device consisting of a SnV center coupled to a nanophotonic diamond waveguide with tapered-fiber access on both sides, depicted in Fig. 4.1(a), and we show its nonlinear interaction at the single-photon level with a weak coherent laser field. We observe the extinction of transmitted light which arises from interference between the photons interacting with the emitter and the single optical mode of the waveguide [19, 20], from which we quantify the coupling strength of the SnV to the waveguide. In the reflected signal we observe interference between single photons scattered by the emitter and a classical reflection of the probe laser. By measuring photon correlations

we observe that the emitter interacts with the incident field at the single photon level, altering its photon statistics both in the transmitted and in the reflected signals. The efficient coupling between SnV and waveguide, together with the single-photon nature of the interaction, make this system a promising starting point for quantum photonic applications.

4.2. DEVICE AND EXPERIMENT

Our device is fabricated in two main phases: the generation of SnV centers in the bulk diamond substrate, followed by the nanofabrication of suspended waveguides that support a single TE mode for SnV emission. An electronic grade diamond substrate is pre-processed and implanted with ^{120}Sn ions at a target depth of ~ 88 nm, followed by an annealing step to create SnV centers. The nanofabrication of the waveguides is based on the crystal-dependent quasi-isotropic-etch undercut method [8, 13, 21–24]. To fabricate the waveguide chips, we first pattern a hard mask material Si_3N_4 , followed by the transfer pattern into the diamond substrate and vertical coverage with Al_2O_3 of the structures sidewalls. Next, the quasi-isotropic etch undercuts the devices, followed by an upward etch to thin the devices down to a thickness of ≈ 250 nm. The fabrication concludes with an inorganic removal of the hard mask materials. The details of the fabrication can be found in section 4.8.a.

Our fabrication differs from earlier work [8, 13, 21–23] in one main aspect: we demonstrate successful quasi-isotropic undercut of the waveguides at a considerably lower temperature of the reactor wafer table of only 65°C . We show that the quasi-isotropic crystal-dependent reactive-ion etch in this temperature regime is successfully undercutting the waveguide structures without the need for an optional O_2 anisotropic etch step following the vertical sidewalls coverage with Al_2O_3 . This has the key benefit of preserving the hard mask aspect ratio, without further edge mask rounding stemming from the O_2 etch.

The fabricated devices consist of arrays of double-sided tapered waveguides, anchored to the surrounding bulk substrate by a square support structure, as seen in Fig. 4.1(b). To couple light in and out of the waveguide we use optical fibers that are etched into conical tapers in hydrofluoric acid [25]. We position the fibers in front of the waveguide and exploit the lensing effect of the taper, as illustrated in Fig. 4.1(a). Though not as efficient as coupling through the evanescent field, we choose this method as it allows easy variation of the distance between fiber and waveguide. This will later be used to tune the phase of the reflected signal. All experiments are performed at 5 K in a closed-cycle cryostat, with no external magnetic field. Within the SnV level structure (Fig. 4.1(c)), we focus on the optical zero-phonon line (ZPL) transition between the lower branches of the ground and excited states, of wavelength around 619 nm. Spontaneous emission from the excited state can also happen with a phonon-assisted process, giving rise to a phonon sideband (PSB).

4.3. OPTICAL TRANSITION STABILITY

A photoluminescence excitation spectrum (PLE) (Fig. 4.1(d)) reveals several SnV centers in the waveguide, which are spectrally resolvable owing to local variations of the strain environment. We investigate the optical stability of one emitter (red arrow in Fig. 4.1(d)) by performing consecutive PLE scans. The scans are pre-conditioned on a successful charge-resonance check [14]: Before each scan, we turn on the probe laser at a set frequency and count how many PSB photons are detected. A threshold number of counts is chosen to make sure that the SnV is in the desired charge state and on resonance with the emitter (see experimental sequences in section 4.8.b). This heralding technique allows to mitigate effects of emitter ionization and of spectral diffusion [14].

4

Summing data from 1.8 hours of continuous measurement (Fig. 4.1(e)), we observe an integrated linewidth of (38.0 ± 0.3) MHz, very close to the average linewidth of the single scans of (32.1 ± 0.1) MHz, indicating that there is very little effective spectral diffusion in our measurements. This can in principle be further improved by increasing the conditioning threshold at the expense of experiment speed. All the measurements reported below are conditioned on a charge-resonant check with similar threshold. By measuring second-order photon correlations using different resonant laser powers (see section 4.8.c), we extract the excited state lifetime of the emitter to be (5.91 ± 0.08) ns, corresponding to a transform-limited transition linewidth of (26.7 ± 0.3) MHz. This value is close to the average single scan linewidth, indicating that there is little residual broadening of the transition.

4.4. SPECTROSCOPY OF THE WAVEGUIDE-SnV SYSTEM

To probe the coupling of the SnV center to the waveguide, we scan the probe laser across the transition frequency, while simultaneously collecting both the transmitted and reflected signals. We spectrally filter the signals and record both ZPL and PSB (separately) in the reflected output port, and the ZPL in the transmission output port (see SI for details). This simultaneous measurement allows us to monitor the SnV behavior through the PSB emission, while observing its coherent interaction with the input probe through the ZPL signal (Fig. 4.2(a)).

We observe a significant extinction of the transmission signal on resonance, indicating a coherent light-matter interaction in our waveguide-QED system [20]: destructive interference between scattered photons and the transmitted field causes the emitter-induced reflection of single photons. The magnitude of the transmission dip contrast on resonance is determined by the emitter-waveguide coupling factor $\beta = \gamma_{\text{wg}} / \gamma_{\text{tot}}$, where γ_{wg} (γ_{tot}) is the decay rate into the waveguide (the total decay rate of the excited state). In particular, in the absence of dephasing of the optical transition, the transmission behavior is described by [26]

$$T(\omega) = \left| 1 - \frac{\beta}{\left(1 + \frac{\langle n \rangle}{n_c}\right) \left(1 - \frac{2i\omega}{\gamma_{\text{tot}}}\right)} \right|^2, \quad (4.1)$$

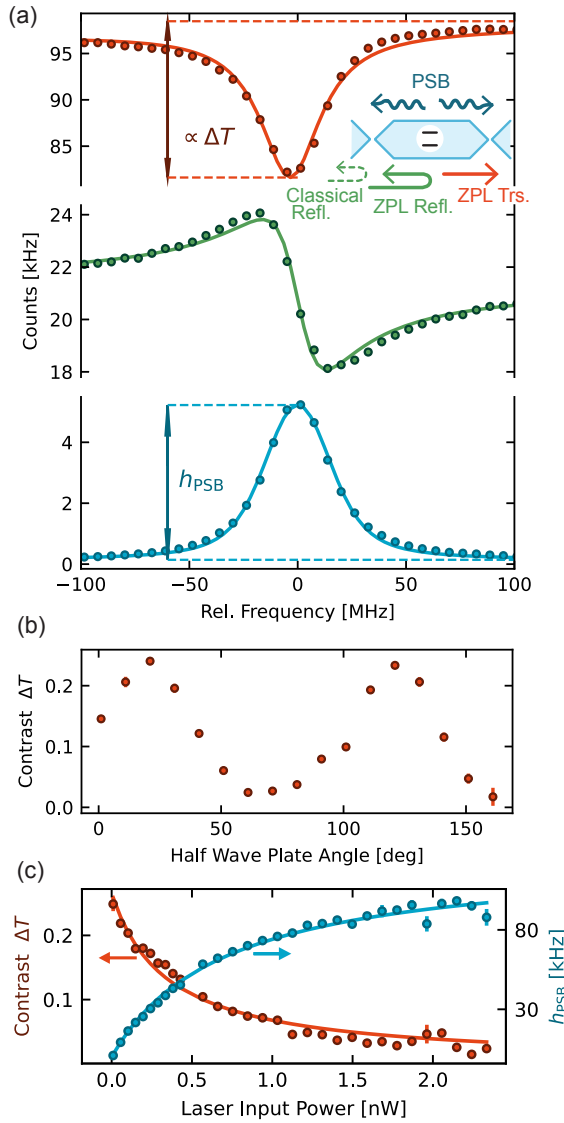


Figure 4.2: **Spectroscopy of the waveguide-SNV system.** (a) Simultaneous measurement of transmitted ZPL light through the system (top), reflected ZPL light (center) and PSB emission (bottom) while scanning the probe laser. The inset shows a schematic of the system, the colors represent the different channels measured. We highlight a relevant quantities used in the rest of the figure: the transmission contrast ΔT and the peak height of the PSB emission scan h_{PSB} . (b) Contrast of the transmission extinction when varying the input fiber polarization. (c) Transmission contrast and PSB peak height as a function of the power in the input fiber showing saturation of the SnV response when the average photon number increases. In the low power range, we observe a maximum transmission extinction of 0.25 ± 0.01 .

where ω is the detuning of the probe laser from the emitter, $\langle n \rangle$ is the average photon number per lifetime in the input state and $n_c = \frac{1}{4\beta^2}$ is the critical photon number, which indicates saturation of the photon-emitter interaction. In the limit of low excitation ($\langle n \rangle \ll n_c$), the transmission contrast on resonance $\Delta T = 1 - T(\omega = 0)$ is thus related to the coupling factor β as $\Delta T = \beta(2 - \beta)$. Note that in this analysis, we ignore the small additional broadening of the optical transition due to dephasing, making our estimates for β a strict lower bound.

Experimentally, the value of the coupling factor β can be reliably extracted by measuring the transmission contrast as a function of input laser power, given that $\langle n \rangle / n_c = P / P_c$ with P_c the input power that saturates the interaction. To ensure that we are optimally coupling the probe field with the linear dipole of the optical transition, we sweep the polarization of the input field to find the maximal transmission contrast (Fig. 4.2(b)). Fitting Eq. (4.1) to the measured transmission contrast as a function of input power (Fig. 4.2(c)) we obtain $\beta = 0.143 \pm 0.005$. This value is in good agreement with numerical simulations for our waveguide geometry (see section 4.8.e) taking into account the emitter depth resulting from the implantation, a small lateral offset (≈ 50 nm) from the waveguide center, and the total efficiency of the transition of interest of 0.37 [27], obtained combining quantum efficiency (0.8) [28], Debye-Waller factor (0.57) [29] and branching ratio between the two ZPL transitions (0.8) [13].

The critical laser power at the fiber input, P_c , corresponds to the critical photon number n_c at the SnV center: $P_c = \eta^{-1} h\nu n_c \gamma$, where η is the fiber-waveguide coupling efficiency, ν is the probe laser frequency and γ is the decay rate related to the excited state lifetime. From the fit value $P_c = (0.32 \pm 0.02)$ nW and knowing $n_c \sim 12$ photons from the value of β , we determine the fiber-waveguide coupling efficiency to be $\eta = 0.33 \pm 0.02$.

The reflection signal contains the single photons coherently reflected by the SnV center, interfering with classical reflection of the probe laser at the tapered fiber end. In a simplified picture, considering a Lorentzian response of the SnV, the reflection signal can be modelled as [30, 31]

$$R(\omega) = \left| 1 + \xi \frac{1}{1 - 2i\omega/\gamma_{\text{tot}}} e^{i\phi} \right|^2, \quad (4.2)$$

where ξ is the ratio between the reflected single photons and the coherent state amplitude, which gives the average number of photons per lifetime in the input field, and ϕ is the phase difference between the coherent and single photon components.

4.5. PHOTON STATISTICS OF TRANSMITTED FIELD

The emitter-induced single-photon nonlinear reflection alters the photon statistics of the transmitted and reflected fields, as we expose below by measuring the second-order correlation for different combination of signals.

We start by correlating the transmitted signal with itself. The emitter can only reflect one photon per its optical lifetime. When two indistinguishable photons coherently scatter on the emitter within the timescale of its optical lifetime, the nonlinear interaction

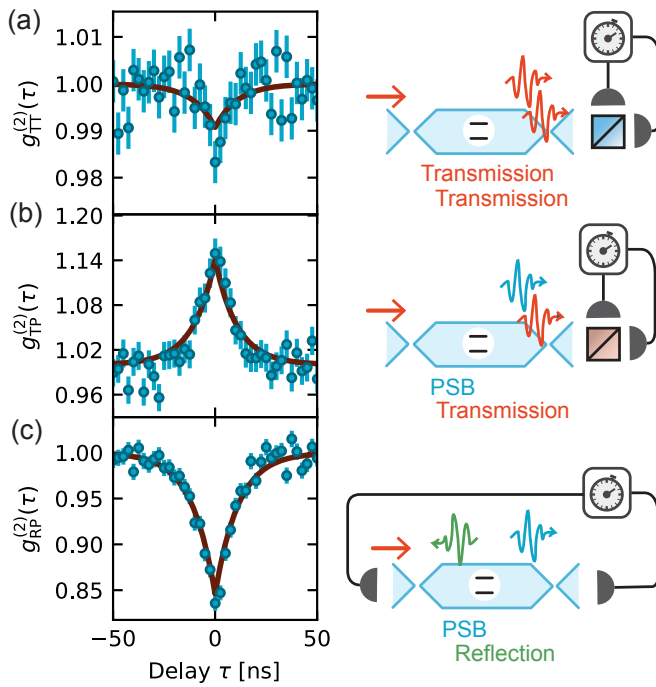


Figure 4.3: **Second order correlations** between (a) two transmitted photons, (b) a PSB and a transmitted photon, (c) a PSB and a reflected photon in the constructive interference regime (see main text and Fig. 4.4 for details). The blue dots are experimental data and the red line is the theoretical model.

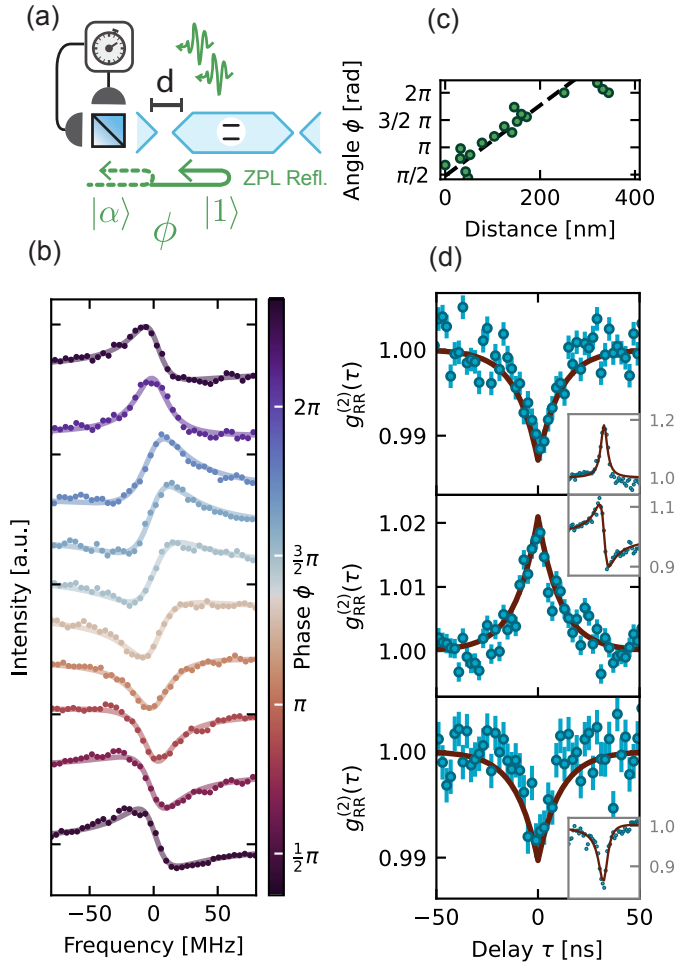


Figure 4.4: **Reflection measurements.** (a) Schematic of the measurement setting. (b) Reflection spectra at different fiber distance, corresponding to different relative phase between the single photon and coherent state components. The solid line is a fit with the simplified model of equation (4.2), from this we extract the phase ϕ which is indicated by the colorbar. (c) Fitted phase as a function of the fiber displacement, measured by the positioner readout sensor. The black dashed line is a guide to the eye indicating a 2π phase change in the distance of half a wavelength. (d) Second order correlation of reflected photons in the constructive (top), dispersive (center) and destructive (bottom) interference regimes. The inset shows the reflection spectrum. We fit the reflection spectrum using Eq. (4.2) to extract ϕ and ξ , which we use as an input to the theoretical model. The red lines, both in the inset and the main figure, are the results of the theoretical model with the supplied parameters. The x axis in the inset is frequency, ranging from -80 MHz to 80 MHz.

results in a strongly correlated two-photon bound-state that is perfectly transmitted [32]. In the case of $\beta \rightarrow 1$ the wavefunction of the scattered light is dominated by this bound-state component, resulting in strong bunching of the transmitted light [19]. In our case however, as the decay rate in the waveguide is lower than the rate of other decay channels ($\beta < 0.5$), the bound-state contribution is suppressed compared to the uncorrelated scattering of the two photons involving other channels. In other words, the probability that one of the two photons is incoherently scattered is higher than the probability of emitting the two-photon bound state in the waveguide. In this regime, upon detection of a photon in the transmission signal the conditional probability of a second ZPL photon detection within the lifetime is suppressed compared to the steady state value. In full agreement with the predictions in Ref. [19], we find that this results in anti-bunching in the photon statistics for the transmission $g_{\text{TT}}^{(2)}$ (Fig. 4.3(a)).

Since we have access to one of the incoherent decay channels, namely the photons emitted in the PSB, we can verify that the effect on the photon statistics is induced by the coherent interaction of light with the emitter. We measure the probability of detecting a transmitted (Fig. 4.3(b)) or reflected photon (Fig. 4.3(c)) conditioned on the emission of a PSB photon. Detecting a PSB photon heralds an incoherent interaction which results in a higher probability of detecting a ZPL photon in the transmission port and a lower probability of detecting a ZPL photon in the reflected port, leading to the observed bunching and anti-bunching, respectively.

We compare the results in Fig. 4.3 with numerical simulations (the red lines in the figures), where the system is modeled as a lossy cavity coupled to an emitter (see section 4.8.f for details). Using values for the model parameters extracted from the data of Fig. 4.2, we find that the simulations accurately reproduce the behavior of the $g^{(2)}$ measurements.

4.6. REFLECTED SIGNAL AND PHOTON STATISTICS

Finally, we investigate the interference between the coherently scattered single photons and the reflected laser light in more detail. By adjusting the fiber position relative to the waveguide, we are able to change the difference between the paths that the classical light and single photon components travel, and thereby controllably tune their relative phase ϕ (Fig. 4.4(a)). Figure 4.4(b) shows the variation in the reflection interference spectrum as we sweep the fiber distance, realized by applying a voltage on the piezo positioner. The phase dependence on distance, which we extract from the piezopositioner sensor, is approximately linear and a full period is obtained in around half wavelength distance (Fig. 4.4(c)).

The photon statistics of the reflected signal depend on the relative phase ϕ . We consider the three limit cases of constructive ($\phi = 6.28 \sim 2\pi$), dispersive ($\phi = 1.57 \sim \pi/2$) and destructive ($\phi = 3.41 \sim \pi$) interference. In the constructive interference case, single photons are added to the coherent state, resulting in sub-poissonian photon statistics as evidenced by the measured anti-bunching in $g_{\text{RR}}^{(2)}$ in Fig. 4.4(d, top). In the dispersive

and destructive interference cases, the presence of a non-zero phase makes the behavior of the photon statistics non-trivial as the relative phase is different for the one- and multi-photon components of the coherent state. Depending on the exact phase and the relative amplitudes of the single photons and the reflected coherent state, the relative weight of the one and two-photon components vary, resulting in either bunching or antibunching. In our regime we observe bunching for the dispersive interference Fig. 4.4(d, middle) and weak antibunching for destructive interference Fig. 4.4(d, bottom). Numerical simulations (red lines) using our theoretical model show excellent agreement with the data.

4.7. CONCLUSIONS

4

In summary, we have presented a detailed investigation of a diamond SnV center coupled to a waveguide, showing significant transmission extinction, tunable interference between single photons and the reflected laser field, as well as providing insights into the nature of the emitter-induced changes in transmitted and reflected fields through photon correlation measurements. These results highlight diamond SnV centers integrated in waveguides as a promising platform for realising efficient integrated spin-photon interfaces.

Whereas nanophotonic cavities can provide overall much stronger interaction, the use of waveguides can alleviate significant fabrication overhead and by their broadband nature provide a more flexible platform, since they do not need to be tuned to the emitter frequency and readily allow for more centers to be used in the same device. We investigated four waveguides in this device and all contained suitably coupled SnV centers, with measured ΔT ranging between 15 – 34%.

While our work shows couplings that are in line with the state of the art for color center-waveguide systems [8, 30, 33], further improvement can be obtained by optimizing the emitter overlap with the optical mode: the waveguide thickness and the implantation depth can be matched to get the SnV closer to the center, while localized ion implantation could improve the lateral position. Already at the established coupling, these devices, when combined with coherent spin control [15, 16], may allow for remote entanglement significantly surpassing the generation rates obtained the diamond NV center [34, 35], opening up new avenues for scaling quantum networks.

4.8. METHODS

4.8.A. SAMPLE AND DEVICE FABRICATION

The sample fabrication process starts with pre-implantation surface treatment of a $\langle 100 \rangle$ surface oriented electronic grade diamond substrate (Element 6). The sample substrate is first cleaned in a wet Piranha (ratio 3:1 of H_2SO_4 (95%) : H_2O_2 (31%)) inorganic solution for 20 min at 80°C , followed by the superficial $\sim 5\mu\text{m}$ etching via inductively-coupled-plasma reactive-ion-etching (ICP/RIE) Ar/ Cl_2 plasma chemistry based recipe in order to remove the residual polishing induced strain from the surface

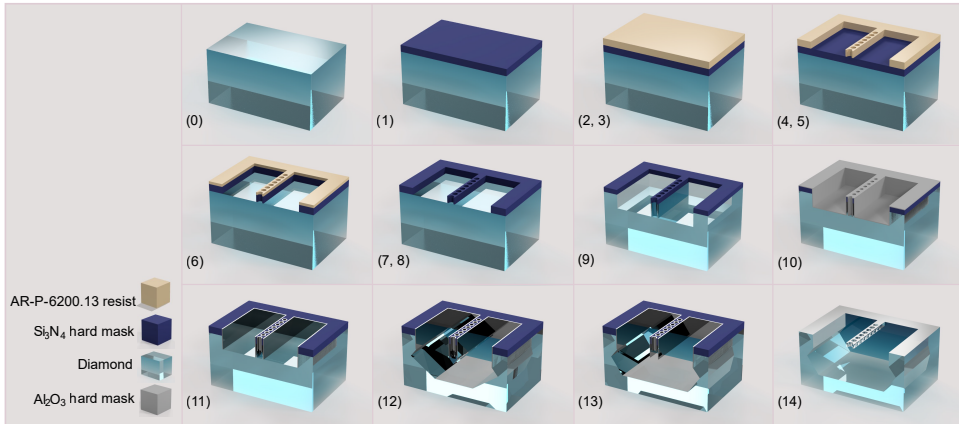


Figure 4.5: Nanophotonic structures fabrication process steps, based on Ref. [8, 13, 21–24]. See text for details.

of the substrate. An additional $\sim 5 \mu\text{m}$ ICP/RIE O_2 chemistry based plasma etch is performed in order to remove residual chlorine contamination from the previous etching step [24]. Following, the sample is inorganically cleaned in a Piranha solution (20 min at 80°C) and implanted with Sn ions (dose $1\text{e}11$ ions/ cm^2 with an energy of 350 keV). Prior to the activation of the SnV centers by vacuum annealing (1200°C), a triacid cleaning (ratio 1:1:1 of HClO_4 (70%) : HNO_3 (70%) : H_2SO_4 (> 99%)) is performed for 1.5 hours in order to remove any residual organic contamination, followed by the the same wet inorganic cleaning procedure after the annealing step in order to remove any superficial graphite thin film layer formed during the annealing step of the diamond substrate. In order to assess the successful activation of the SnV centers, the sample is characterized prior to the nanofabrication of the suspended structures.

The nanofabrication of waveguiding structures follows the process based on the crystal-dependent quasi-isotropic-etch undercut method developed in references [8, 13, 21–23] and [24]. A schematics of this is illustrated in Fig. 4.5.

Specifically, we start with a pre-fabrication process extensive inorganic clean for 20 min in HF (40%) at room temperature (Fig. 4.5, step 0), followed by deposition and patterning of a hard mask material thin film layer of ~ 221 nm Si_3N_4 via plasma-enhanced-chemical-vapour-deposition (PECVD) (Fig. 4.5, step 1). The waveguide structures design is longitudinally aligned with the $\langle 110 \rangle$ diamond crystallographic orientation and exposed via e-beam lithography of ~ 450 nm of AR-P-6200.13 positive tone resist (Fig. 4.5, steps 2 and 3). In order to avoid charging effects of the diamond substrate during the e-beam exposure, the surface of the e-beam resist is coated with ~ 40 nm Electra 92 (AR-PC 5090) conductive polymer. Next, this is developed by immersing the sample in 60 s gentle stirring in H_2O and N_2 blow-dry (to dissolve Electra 92), followed by 60 s DI water, 60 s pentyl acetate, 5 s ortho-xylene, 60 s isopropyl alcohol (IPA) (Fig. 4.5, steps 4 and 5). The process proceeds with the transfer pattern into the Si_3N_4 hard mask material by means of ICP/RIE etch in a CHF_3/O_2 based plasma chemistry (Fig. 4.5, step 6) and complete removal of residual e-beam resist in a two-fold wet step: we first proceed with a resist removal in a PRS 3000 positive resist stripper solution, followed by extensive Pi-

ranha clean inorganic treatment for complete removal of organic material residues (Fig. 4.5, steps 7 and 8). Such considerable inorganic cleaning is employed in order to prevent micro-masking within next dry etch steps that can potentially be caused by organic residues on the sample.

The transfer pattern from the Si_3N_4 hard mask material is transferred by etching top-down in a dry ICP/RIE O_2 plasma chemistry etch in the diamond substrate for an extent of $\sim 2.4\times$ the designed thickness of the devices (Fig. 4.5, step 9). It is crucial to note that the O_2 dry etch heavily affects the aspect ratio of the patterned Si_3N_4 hard mask: we observe the etch rate of Si_3N_4 to be higher at the edges of the patterned structures compared to the determined etch rate of Si_3N_4 on flat area test samples, leading to enhanced erosion of the Si_3N_4 at the edges of the nanostructures. This yields rounded vertical sidewalls with few nanometers of hard mask material at the diamond to Si_3N_4 interface [24]. This leads to weak points across the top surface of the hard mask that can compromise the integrity of the hard mask through the following fabrication steps. We circumvent this challenge by carefully tuning the trade-off between sufficient anisotropic diamond etch and Si_3N_4 mask integrity such that the last withstands the following O_2 based dry etch steps foreseen by the overall fabrication process.

Next, conformal atomic layer deposition (ALD) of ~ 26 nm of Al_2O_3 for hard mask coverage of devices vertical sidewalls (Fig. 4.5, step 10) and the horizontal coverage of Al_2O_3 is fully removed by ICP/RIE etch in a BCl_3/Cl_2 plasma chemistry etch (Fig. 4.5, step 11). This opens access to the diamond substrate: we directly follow with a two-step quasi-isotropic etch. For this, we employ the recipe developed in reference [24]. In contrast to Ref. [8, 13, 21–23], here the quasi-isotropic etch plasma reactor wafer table temperature is only 65°C , therefore completing the full undercut and upward etch of the devices to the target thickness in 2 steps of 9 hours etch each (Fig. 4.5, steps 12 and 13). The full release and upward quasi-isotropic total etch time is considerably long when compared to high temperature plasma regimes. On the other hand, here we demonstrate that this method successfully undercuts diamond waveguides in a low temperature regime. Finally, the hard mask materials are removed in an extensive inorganic treatment for 20 min in HF (40%) at room temperature (Fig. 4.5, step 14).

The overall qualitative characterization of the fabrication steps presented in this work has been executed on a scanning electron microscope Hitachi SEM Regulus system. The etch rates concerning the fabrication steps 6, 9 and 11 (Fig. 4.5) have been pre-characterized on additional test samples, in parallel to the fabrication of the diamond sample employed in this work following similar methodology. Such etch tests have been conducted employing silicon substrate samples, with the thin films of interest deposited in parallel to the diamond substrate. Optical parameters and thickness of the employed materials have been determined via spectroscopic ellipsometry method on a Woollam M-2000 (XI-210) tool. The quasi-isotropic etch rate has been characterized employing supplementary diamond test samples (fabrication parallel to the sample in this work) and analyzed via SEM inspection.

4.8.B. MEASUREMENT SEQUENCES

Figure 4.6 shows the measurement sequence for the experiments we realised. The control of the AOM pulses, fast laser frequency sweeps, APD counting, triggering of the time

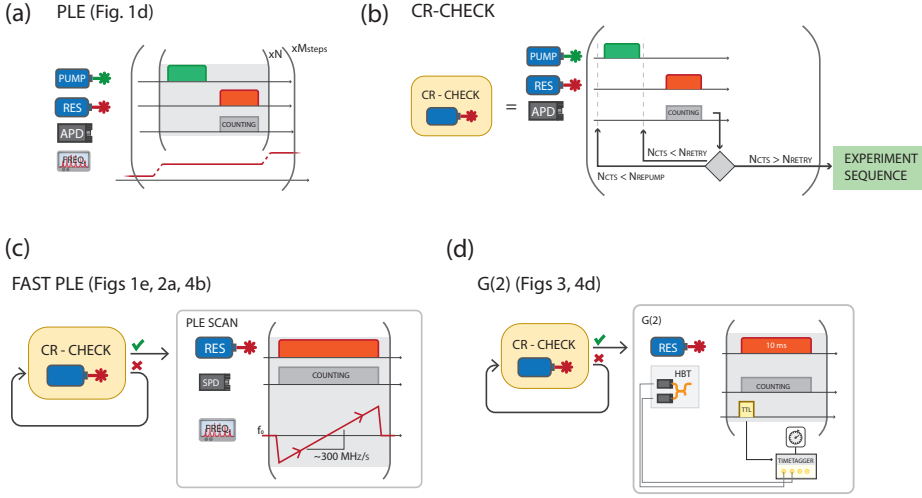


Figure 4.6: Measurement sequences

tagging hardware and logic operations are done by a Adwin Pro II microprocessor. The photoluminescence excitation (PLE) measurement in Fig. 1(d) of the main text is done with the sequence in 4.6(a). We step the laser frequency and for each point we repeat a sequence consisting of a repump and a resonant pulse, during which we count the emitted photons. To ensure that the SnV is in the correct charge and frequency state, we condition the measurements on a successful Charge-Resonance Check (CR-Check, Fig. 4.6(b)), see Ref [14] for details of the procedure. We use CR-conditioned "fast" repeated PLE scans (Fig. 4.6(c)) to measure the PSB, transmission and reflection spectra in order to extract ΔT and the reflection parameters ξ and ϕ . We apply an analog voltage to scan the laser frequency around a set point in a step-wise way. In each step we integrate the counts of the APDs for 20 ms. The single scan speed is ~ 300 MHz/s. We perform the $g^{(2)}$ measurements with the sequence in Fig 4.6(d), by repeatedly sending 10 ms resonant pulses, preceded by a trigger TTL pulse that serves as a sync signal for the timetagger. The pulses are conditioned on a CR Check to ensure that the SnV is resonant with the probe.

4.8.C. LIFETIME MEASUREMENT FROM RESONANT $g_{PP}^{(2)}(\tau)$

To verify that the optical transition is transform limited, we extract the optical decay rate from a series of resonant second order correlation measurements at different powers. We resonantly excite the transition with 10 ms laser pulses and measure the second order correlation of the emitted PSB photons $g_{PP}^{(2)}$ (Fig. 4.7(a)). We vary the power of the excitation pulse and for each measurement and fit the data with the function [36, p. 208]

$$g_{PP}^{(2)}(\tau) = 1 - e^{-(3\Gamma/4)\tau} \left(\cos \Omega_{\Gamma} \tau + \frac{3\Gamma}{4\Omega_{\Gamma}} \sin \Omega_{\Gamma} \tau \right) + C. \quad (4.3)$$

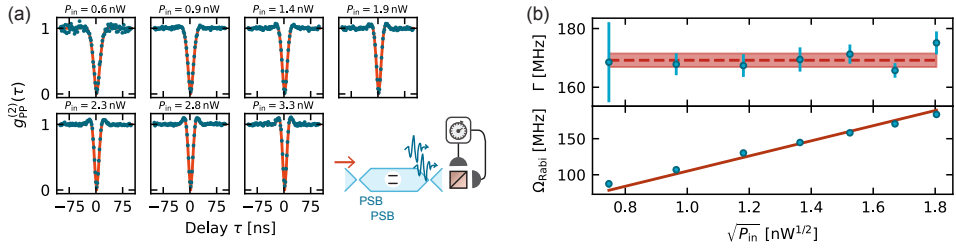


Figure 4.7: (a) Second order correlation between two PSB photons measured at various powers. The light blue curve is a fit using equation 4.3 (b) From the fit in (a) we extract the decay rate (top) and Rabi frequency (bottom) as a function of the probe laser power. We obtain the decay rate by a weighted average of the values (dashed red line in the top graph, shadowed area indicates the uncertainty). The red line in the bottom graph is a linear fit.

4

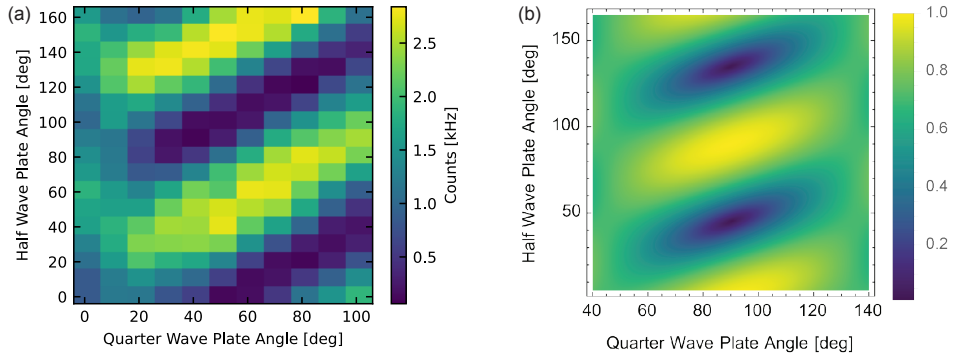


Figure 4.8: Effect of the probe laser polarization on detected PSB counts. (a) Varying the angles of a quarter and half wave plate in the path of the probe laser changes the amount of detected PSB counts. (b) A model of the effect based on Jones calculus.

At the lowest measured power, $g_{pp}^{(2)}(0) = 0.036 \pm 0.019$, showing that we are measuring a single emitter. Additionally, we extract the optical Rabi frequency and the decay rate from the fits. The top graph in Figure 4.7(b) shows the decay rate for each measurement. We take the weighted average, including the uncertainty, to extract a decay rate Γ of (168 ± 2) MHz, which corresponds to a excited state lifetime of (5.91 ± 0.08) ns and to a transform-limited transition linewidth of (26.7 ± 0.3) MHz. This matches well with our average single scan linewidth, indicating that there is little residual broadening of the transition. The bottom plot shows the Rabi frequency, which scales linearly as the square root of the probe power. This measurement is also performed with CR-checks in between excitation pulses.

4.8.D. INPUT POLARIZATION

Here we vary the polarization of the probe laser by changing the angles of two fiber paddles acting as a $\lambda/4$ and $\lambda/2$ waveplate, respectively (see Fig. ??). At each combination

of angles, we record 30 PLE scans and fit the summed PSB counts with a Lorentzian, as done in Fig. 2(a). In Fig. 4.8(a) plot the height of that Lorentzian h_{PSB} (we filter out the failed fits, mostly happening in the area where the counts are low). When the polarization of the probe laser is aligned with the dipole moment of the SnV, the PSB counts are maximal. Rotating the half wave plate by $\sim 45^\circ$ from that optimal setting, makes the polarization of the probe laser orthogonal to the dipole moment of the SnV, this is where the counts are minimal. We model this behaviour using the Jones calculus [37]. Here the waveplates are described by 2x2 matrices

$$M_{\lambda/2}(\phi) = e^{-i\pi/2} \begin{pmatrix} \cos^2 \phi - \sin^2 \phi & 2 \sin \phi \cos \phi \\ 2 \sin \phi \cos \phi & -\cos^2 \phi + \sin^2 \phi \end{pmatrix} \quad (4.4)$$

and

$$M_{\lambda/4}(\phi) = e^{-i\pi/4} \begin{pmatrix} \cos^2 \phi + i \sin^2 \phi & (1-i) \sin \phi \cos \phi \\ (1-i) \sin \phi \cos \phi & i \cos^2 \phi + \sin^2 \phi \end{pmatrix}, \quad (4.5)$$

where ϕ is the rotation angle of the waveplate. We act with both waveplates on vertical polarization and then project on vertical polarization.

$$\begin{aligned} h_{\text{PSB}}^{\text{model}}(\phi_1, \phi_2) &= \left\| \begin{pmatrix} 1 \\ 0 \end{pmatrix}^T M_{\lambda/2}(\phi_1) M_{\lambda/4}(\phi_2) \begin{pmatrix} 1 \\ 0 \end{pmatrix} \right\| \\ &= \frac{1}{2} \sqrt{\cos[4(\phi_1 - \phi_2)] + \cos(4\phi_2) + 2} \end{aligned}$$

The modeled behavior is shown in Fig. 4.8(b) and reproduces well the measured data, except for an absolute shift in the waveplates angles. Note that since we don't know the absolute polarization at the location of the fiber paddles the plot ranges of experiment and model are not the same. Also the fiber paddles do not induce perfect $\lambda/2$ and $\lambda/4$ retardation.

4.8.E. SIMULATIONS OF SNV-WAVEGUIDE COUPLING

We compare the measured β factor with finite element simulations in COMSOL Multiphysics, as outlined in Section 3.3.2. The waveguide is assumed to be rectangular of width 300 nm and height 250 nm, which is the approximate dimension of the devices for this sample measured from SEM images. We simulate different positions of the dipole in the waveguide: at the center, where the maximum coupling is expected, and at the implantation depth of 88 nm with three different offsets from the center in the x direction (Δx) of 0, 50 and 100 nm. For all of these we report the coupling for an ideal dipole β_{ideal} . We account for the finite efficiency of the SnV C-transition by multiplying the β_{ideal} from simulations by $\zeta = \text{QE} \times \text{DW} \times \text{BR} = 0.37$ [27], so we get $\beta_{\text{eff}} = \zeta \beta_{\text{ideal}}$. We obtain the following values:

We observe that the measured coupling for our emitter, $\beta = 0.143$ agrees very well with the SnV being located at the implantation depth and offset from the center of the waveguide by ~ 50 nm.

| Depth [nm] | Δx [nm] | β_{ideal} | β_{eff} |
|------------|-----------------|------------------------|----------------------|
| 125 | 0 | 0.606 | 0.224 |
| 88 | 0 | 0.507 | 0.187 |
| 88 | 50 | 0.403 | 0.149 |
| 88 | 100 | 0.256 | 0.095 |

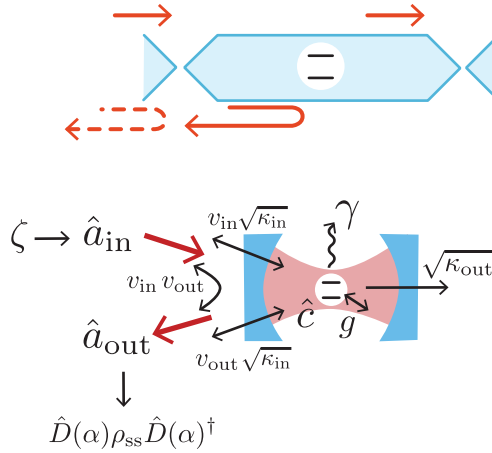


Figure 4.9: Schematic of the theoretical model. Above a sketch of the input and output channels of the waveguide-SnV system, below the corresponding modes and coupling parameters.

4.8.F. THEORETICAL MODELS

ANALYTICAL MODEL FOR TRANSMISSION AND REFLECTION FITTING

For the analytical formula describing the behavior of the transmission signal and used for the fits we follow closely the theory in [26, 38]. The transition linewidth of our SnV is very close to the transform limited value expected from the lifetime measurement, so we choose to neglect dephasing in the transmission dip analysis. In the presence of dephasing, the transmission extinction contrast for a fixed β is decreased. For a dephasing rate γ_{deph} this scales as

$$\Delta T = \frac{\beta(2-\beta)}{1+2\frac{\gamma_{\text{deph}}}{\gamma_{\text{tot}}}}. \quad (4.6)$$

This makes our β a lower bound, since if dephasing is present we would need a stronger coupling to explain the contrast we measure. For the reflection spectrum we assume a simple single mode interference with a lorentzian response of the emitter, similar to what observed in [30, 31].

MODEL FOR THE NUMERICAL SIMULATIONS OF THE $g^{(2)}$

For numerically simulating the $g^{(2)}$, we model the SnV-waveguide system as a lossy cavity coupled to a two level system as depicted in Fig. 4.9. The transmission signal can

be obtained by the decay of the cavity mode \hat{c} in the output of the cavity. For modeling the reflection we use a similar approach as in [39], where two modes \hat{a}_{in} and \hat{a}_{out} couple to the cavity. We add a coherent drive on mode \hat{a}_{in} to model the laser field. Part of the cavity mode which does not interact with the emitter can leak out in the reflection mode \hat{a}_{out} . This artifact coming from the cavity approximation is unwanted as in the waveguide the non-interacting light should go through. We tune the cross-coupling term $\nu_{\text{in}}\nu_{\text{out}}$ to cancel out the unwanted leaking light from the cavity. \hat{a}_{out} now represents the ideal reflection from the waveguide-QED system. The dynamics of the system is described by the Hamiltonian:

$$H = H_0 + H_{\text{drive}} + H_{\text{JC}} + H_{\text{three-mode}} \quad (4.7)$$

$$H_0 = (\omega_e - \omega)|e\rangle\langle e| + (\omega_c - \omega) \left[\hat{c}^\dagger \hat{c} + \hat{a}_{\text{in}}^\dagger \hat{a}_{\text{in}} + \hat{a}_{\text{out}}^\dagger \hat{a}_{\text{out}} \right] \quad (4.8)$$

$$H_{\text{drive}} = i\zeta(\hat{a}_{\text{in}}^\dagger - \hat{a}_{\text{in}}) \quad (4.9)$$

$$H_{\text{JC}} = ig(\hat{c}|e\rangle\langle g| + h.c.) \quad (4.10)$$

$$H_{\text{three-mode}} = (\sqrt{\kappa_{\text{in}}}\nu_{\text{in}}\hat{a}_{\text{in}}^\dagger\hat{c} + \sqrt{\kappa_{\text{in}}}\nu_{\text{out}}\hat{c}^\dagger\hat{a}_{\text{out}} + \nu_{\text{in}}\nu_{\text{out}}\hat{a}_{\text{in}}^\dagger\hat{a}_{\text{out}} + h.c.) \quad (4.11)$$

and the jump operators:

$$L_{\text{emitter}} = \sqrt{\gamma}|e\rangle\langle e| \quad (4.12)$$

$$L_{\text{cavity}} = \sqrt{\kappa_{\text{in}} + \kappa_{\text{out}}}\hat{c} \quad (4.13)$$

$$L_{\text{three-mode}} = \sqrt{\kappa_{\text{in}}}\hat{c} + \nu_{\text{in}}\hat{a}_{\text{in}} + \nu_{\text{out}}\hat{a}_{\text{out}}. \quad (4.14)$$

The "lossy cavity" approximation of the waveguide is realised by having all coupling terms between the optical modes larger than the emitter decay rate, $(\kappa_{\text{in}} + \kappa_{\text{out}}), \nu_{\text{in}}, \nu_{\text{out}} \gg \gamma$. Since we are interested in the low excitation regime, we truncate the Hilbert space to two excitations. We match the measured waveguide coupling with the weak-cavity parameters, we calculate the effective cooperativity corresponding to β :

$$C = \frac{\beta}{1 - \beta} = \frac{4g^2}{\kappa\gamma}. \quad (4.15)$$

We use the QuTiP Python package [40] to numerically solve the master equation for the density matrix and the steady state of the system ρ_{ss} .

To model the interference between the scattered photons and the classical light from the input laser, we use a displaced single photon state [41]. We displace the steady state density matrix with a displacement operator $\hat{D}(\alpha)$, the complex amplitude α has a phase ϕ which encodes the phase difference between the single photon and coherent components, and amplitude $|\alpha|$ that is set in order to match the single-photon/coherent state ratio ξ as measured experimentally. We transform the Hamiltonian and jump operator to work on a displaced frame:

$$H \rightarrow \hat{D}(\alpha)H\hat{D}(\alpha)^\dagger \quad (4.16)$$

$$L \rightarrow \hat{D}(\alpha)L\hat{D}(\alpha)^\dagger. \quad (4.17)$$

The operators we use for transmission, reflection and PSB are:

$$\hat{t} = \sqrt{\kappa_{\text{out}}}\hat{c} \quad (4.18)$$

$$\hat{r} = \hat{D}(\alpha)\hat{a}_{\text{out}}\hat{D}(\alpha) \quad (4.19)$$

$$\hat{\sigma}_e = |e\rangle\langle e|. \quad (4.20)$$

For every simulation, we first reproduce the spectrum by feeding the model with the measured parameters β, ϕ, ξ and measuring the expectation value for $\hat{t}^\dagger \hat{t}, \hat{r}^\dagger \hat{r}$ and $\hat{\sigma}_e$. Then, we calculate the second order correlation between two arbitrary operators \hat{O}_1, \hat{O}_2 as:

$$g_{\hat{O}_1 \hat{O}_2}^{(2)}(\tau) = \frac{\text{Tr}\{\hat{O}_2^\dagger \hat{O}_2 e^{\tau \mathcal{L}} (\hat{O}_1 \rho_{ss} \hat{O}_1^\dagger)\}}{\text{Tr}\{\hat{O}_1 \rho_{ss} \hat{O}_1^\dagger\} \text{Tr}\{\hat{O}_2 \rho_{ss} \hat{O}_2^\dagger\}} \quad (4.21)$$

Where \mathcal{L} is the Liouvillian superoperator calculated in the displaced frame.

BIBLIOGRAPHY

- [1] D. D. Awschalom, R. Hanson, J. Wrachtrup and B. B. Zhou, *Quantum technologies with optically interfaced solid-state spins*, Nature Photonics **12**, 516 (2018).
- [2] M. Atatüre, D. Englund, N. Vamivakas, S.-Y. Lee and J. Wrachtrup, *Material platforms for spin-based photonic quantum technologies*, Nature Reviews Materials **3**, 38 (2018).
- [3] H. J. Kimble, *The quantum internet*, Nature **453**, 1023 (2008).
- [4] S. Wehner, D. Elkouss and R. Hanson, *Quantum internet: A vision for the road ahead*, Science **362** (2018), 10.1126/science.aam9288.
- [5] M. Pompili *et al.*, *Realization of a multinode quantum network of remote solid-state qubits*, Science **372**, 259 (2021).
- [6] S. L. N. Hermans *et al.*, *Qubit teleportation between non-neighbouring nodes in a quantum network*, Nature **605**, 663 (2022).
- [7] M. K. Bhaskar *et al.*, *Experimental demonstration of memory-enhanced quantum communication*, Nature **580**, 60 (2020).
- [8] N. H. Wan *et al.*, *Large-scale integration of artificial atoms in hybrid photonic circuits*, Nature **583**, 226 (2020).
- [9] C. Bradac, W. Gao, J. Forneris, M. E. Trusheim and I. Aharonovich, *Quantum nanophotonics with group IV defects in diamond*, Nature Communications **10**, 5625 (2019).
- [10] M. Ruf, N. H. Wan, H. Choi, D. Englund and R. Hanson, *Quantum networks based on color centers in diamond*, Journal of Applied Physics **130**, 070901 (2021).
- [11] M. E. Trusheim *et al.*, *Transform-Limited Photons From a Coherent Tin-Vacancy Spin in Diamond*, Physical Review Letters **124**, 023602 (2020).
- [12] J. Arjona Martínez *et al.*, *Photonic Indistinguishability of the Tin-Vacancy Center in Nanostructured Diamond*, Physical Review Letters **129**, 173603 (2022).
- [13] A. E. Rugar *et al.*, *Quantum Photonic Interface for Tin-Vacancy Centers in Diamond*, Physical Review X **11**, 031021 (2021).
- [14] J. M. Brevoord *et al.*, *Heralded initialization of charge state and optical transition frequency of diamond tin-vacancy centers*, (2023), arxiv:2311.11962 [quant-ph] .
- [15] E. I. Rosenthal *et al.*, *Microwave Spin Control of a Tin-Vacancy Qubit in Diamond*, (2023), arxiv:2306.13199 [cond-mat, physics:quant-ph] .
- [16] X. Guo *et al.*, *Microwave-based quantum control and coherence protection of tin-vacancy spin qubits in a strain-tuned diamond membrane heterostructure*, (2023), arxiv:2307.11916 .

- [17] H. K. C. Beukers *et al.*, *Tutorial: Remote entanglement protocols for stationary qubits with photonic interfaces*, (2023), arxiv:2310.19878 [quant-ph] .
- [18] A. Sipahigil *et al.*, *An integrated diamond nanophotonics platform for quantum-optical networks*, *Science* **354**, 847 (2016).
- [19] D. E. Chang, A. S. Sørensen, E. A. Demler and M. D. Lukin, *A single-photon transistor using nanoscale surface plasmons*, *Nature Physics* **3**, 807 (2007).
- [20] J. T. Shen and S. Fan, *Coherent photon transport from spontaneous emission in one-dimensional waveguides*, *Optics Letters* **30**, 2001 (2005).
- [21] B. Khanaliloo, M. Mitchell, A. C. Hryciw and P. E. Barclay, *High-Q/V Monolithic Diamond Microdisks Fabricated with Quasi-isotropic Etching*, *Nano Letters* **15**, 5131 (2015).
- [22] M. Mitchell, D. P. Lake and P. E. Barclay, *Realizing $Q > 300\,000$ in diamond microdisks for optomechanics via etch optimization*, *APL Photonics* **4**, 016101 (2019).
- [23] S. Mouradian, N. H. Wan, T. Schröder and D. Englund, *Rectangular photonic crystal nanobeam cavities in bulk diamond*, *Applied Physics Letters* **111**, 021103 (2017).
- [24] M. Ruf, *Cavity-Enhanced Quantum Network Nodes in Diamond*, Ph.D. thesis, Delft University of Technology (2021).
- [25] M. J. Burek *et al.*, *Fiber-Coupled Diamond Quantum Nanophotonic Interface*, *Physical Review Applied* **8**, 024026 (2017).
- [26] H. Thyrrstrup *et al.*, *Quantum Optics with Near-Lifetime-Limited Quantum-Dot Transitions in a Nanophotonic Waveguide*, *Nano Letters* **18**, 1801 (2018).
- [27] Y. Herrmann *et al.*, *Coherent Coupling of a Diamond Tin-Vacancy Center to a Tunable Open Microcavity*, (2023), arxiv:2311.08456 [quant-ph] .
- [28] T. Iwasaki *et al.*, *Tin-Vacancy Quantum Emitters in Diamond*, *Physical Review Letters* **119**, 253601 (2017).
- [29] J. Görlitz *et al.*, *Spectroscopic Investigations of Negatively Charged Tin-Vacancy Centres in Diamond*, *New Journal of Physics* **22**, 013048 (2020), arxiv:1909.09435 [cond-mat, physics:quant-ph] .
- [30] M. K. Bhaskar *et al.*, *Quantum Nonlinear Optics with a Germanium-Vacancy Color Center in a Nanoscale Diamond Waveguide*, *Physical Review Letters* **118**, 223603 (2017).
- [31] M. K. Koch *et al.*, *Super-Poissonian Light Statistics from Individual Silicon Vacancy Centers Coupled to a Laser-Written Diamond Waveguide*, *ACS Photonics* **9**, 3366 (2022).

- [32] J.-T. Shen and S. Fan, *Strongly Correlated Two-Photon Transport in a One-Dimensional Waveguide Coupled to a Two-Level System*, Physical Review Letters **98**, 153003 (2007).
- [33] R. A. Parker *et al.*, *A diamond nanophotonic interface with an optically accessible deterministic electronuclear spin register*, (2023), arxiv:2305.18923 .
- [34] H. Bernien *et al.*, *Heralded entanglement between solid-state qubits separated by three metres*, Nature **497**, 86 (2013).
- [35] S. Hermans, *Quantum Networks Using Spins in Diamond*, Ph.D. thesis, Delft University of Technology (2022).
- [36] D. Steck, *Quantum and Atom Optics* (2007).
- [37] E. Collett, *Field Guide to Polarization* (SPIE, 2005).
- [38] A. Javadi *et al.*, *Single-photon non-linear optics with a quantum dot in a waveguide*, Nature Communications **6**, 8655 (2015).
- [39] A. H. Kiielerich and K. Mølmer, *Input-Output Theory with Quantum Pulses*, Physical Review Letters **123**, 123604 (2019).
- [40] J. Johansson, P. Nation and F. Nori, *QuTiP: An open-source Python framework for the dynamics of open quantum systems*, Computer Physics Communications **183**, 1760 (2012).
- [41] F. A. M. de Oliveira, M. S. Kim, P. L. Knight and V. Buek, *Properties of displaced number states*, Physical Review A **41**, 2645 (1990).

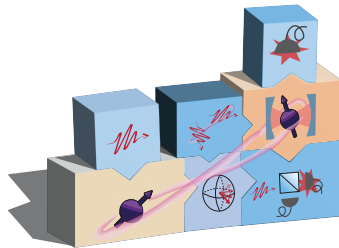


5

REMOTE-ENTANGLEMENT PROTOCOLS FOR QUBITS WITH PHOTONIC INTERFACES

H.K.C. Beukers*, M. Pasini*, H. Choi*, D. Englund, R. Hanson and J. Borregaard

Generating entanglement between distant quantum systems is at the core of quantum networking. In recent years, numerous theoretical protocols for remote entanglement generation have been proposed, of which many have been experimentally realized. Here, we provide a modular theoretical framework to elucidate the general mechanisms of photon-mediated entanglement generation between single spins in atomic or solid-state systems. Our framework categorizes existing protocols at various levels of abstraction and allows for combining the elements of different schemes in new ways. These abstraction layers make it possible to readily compare protocols for different quantum hardware. To enable the practical evaluation of protocols tailored to specific experimental parameters, we have devised numerical simulations based on the framework with our codes available online.



*These authors contributed equally to this work

The content of this chapter has been published in Phys. Rev. X Quantum 5, 010202 (2024)

5.1. INTRODUCTION

Remote entanglement of quantum systems is a vital component in quantum networks and computing [1–3]. Since remote stationary qubits cannot interact directly, a “flying qubit” is needed to mediate the interaction and generate entanglement. Photons offer versatility, as they can transfer quantum information over long distances with low-loss optical fibers, operate at room temperature, and be easily detected with single-photon detectors. In a photon-mediated entanglement protocol, stationary qubits interact selectively with photons, usually via an optical transition, resulting in the entanglement between the photon and the stationary qubit. This entanglement between photons and spins can be used to create entanglement between two distant qubits. The entanglement generated can have high fidelity even in the presence of photonic loss, as photon detection can be used to herald a successful entanglement attempt [4–10], as long as sources of false heralding are limited. These individual entanglement links between quantum nodes can then be combined to distribute the entanglement through a quantum network [11]. This distributed entanglement has been used to perform unconditional quantum teleportation between nodes without a direct optical link [12]. Overall, these technologies pave the way toward network-based quantum computing [13], entanglement-based quantum communications [14], distributed quantum sensing, and long-distance interferometry [15].

5

Photon-mediated remote entanglement of stationary qubits has been demonstrated in numerous quantum systems, including trapped ions [16], neutral atoms [17, 18], semiconductor quantum dots [19, 20], and color centers in diamond [21, 22]. Different demonstrations rely on different entanglement generation protocols, where the choice of protocol implementation is dictated by the features or limitations of the experimental platform. As a result, the implementation of the entanglement protocol is often tailored to specific hardware.

Here, we present a theoretical framework for comparing and understanding different photon-mediated remote-entanglement protocols (REPs). The modular framework consists of four layers, with modules assembled by connecting the output of one to the input of another. The advantage of this framework is that it gives insights into the common features of remote-entanglement protocols. Moreover, it allows easy modification of the modules to compare a protocol with different types of quantum hardware or to rearrange the quantum hardware and test different protocols with the same hardware (which is done in Section 5.8). Dedicated simulations of entanglement generation for a given experiment usually lack this flexibility.

We start by explaining the high-level idea and how the first layer (the “logical building block and topology” layer) can describe REPs in a generic manner. Next, we introduce the encoding and physical building block layers, which link the protocol to specific hardware. Finally, the quantum optical modeling layer provides a detailed and quantitative description of the physical building blocks. Our focus is on qubits realized with a single spin in atomic or solid-state systems, but the framework can incorporate other

systems such as the spin wave in an atomic ensemble and optomechanical resonators, as well as superconducting qubits. These single entangled links between qubits could later be extended to multi-pin encoding for error correction for fault-tolerant quantum networks [23].

We have released a simulation software package titled QuREBB (Quantum Remote-Entanglement Building Blocks) which is available in an accompanying GitHub repository (Sec. 5.7) [24]. This package offers a comparison of three exemplary entanglement protocols. For each protocol, we review every layer, from the idealized version to its practical implementation. As an example, we assume that the protocols are implemented with silicon-vacancy color centers in diamond nanophotonic cavities. This serves as a tutorial on how to effectively employ our theoretical framework for the construction and quantitative analysis of the performance of the protocol. The modular structure of our software implementation mirrors the framework, enabling the implementation of complex quantum systems from the physical to the network levels. Users can easily add new physical devices or logical units without interfering with existing functionality. Our “named quantum object” simplifies the tensor operations of different quantum subsystems by indexing them by names instead of numerical values.

Note that in each layer, we have descriptions of photons, spins, and spin-photon interfaces. In this work, we elaborate spin-photon interfaces in the most detail for their critical role in the creation of entanglement. We also systematically analyze the photonic and spin operations focusing on the construction of REPs. We refer readers interested in more details on spin or photon operations to Refs. [25–27].

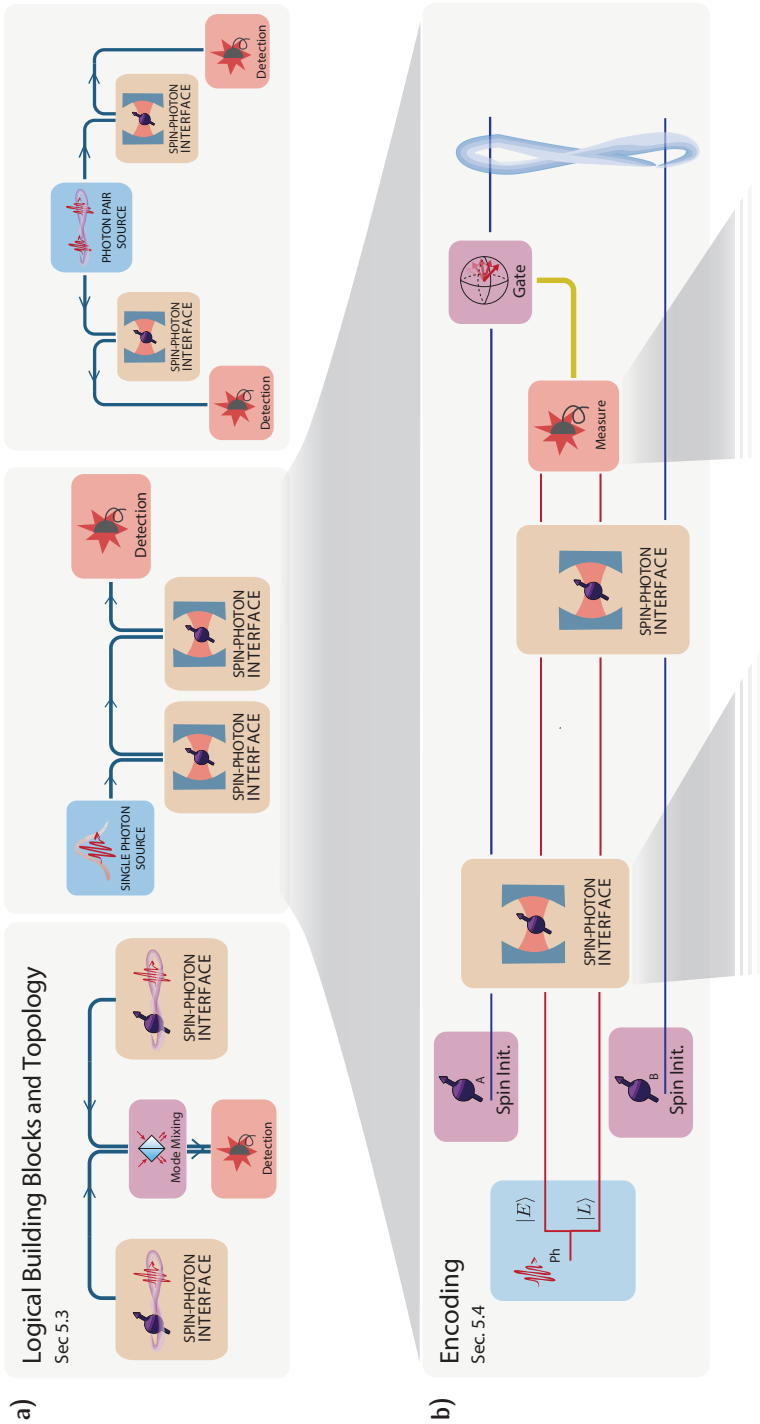
5.2. REMOTE-ENTANGLEMENT-PROTOCOL FRAMEWORK

Figure 5.1 shows our modular framework for REPs. The framework consists of four layers, each becoming more specific and detailed in terms of hardware. Throughout the paper, we refer to stationary qubits as spins for convenience.

In the first layer, we choose the topology of the protocol and construct it using logical building blocks (LBBs) (Fig. 5.1(a)). The topology, i.e., how the photons travel between the nodes, determines the generic high-level quantum circuit and the LBBs are the idealized quantum operations, such as the spin-photon interface, the photon source, and the photodetector. The LBBs act on the spin qubit or the photonic qubit, or both. This layer simplifies and categorizes REPs, giving insight into the entanglement generation. The REP topology is classified into detection-in-midpoint, sender-receiver, and source-in-midpoint protocols [28], as shown in Fig.5.1(a). We use the sender-receiver topology as an example in the figure.

In the second layer, we choose the qubit encoding, in particular the photonic encoding which is the most relevant for the REP: Fock state, polarization, dual rail, frequency encoding, or time-bin encoding, the latter is shown in Fig.5.1(b). This layer translates the abstract photonic and spin qubits into a specific implementation in the system.

Entanglement link



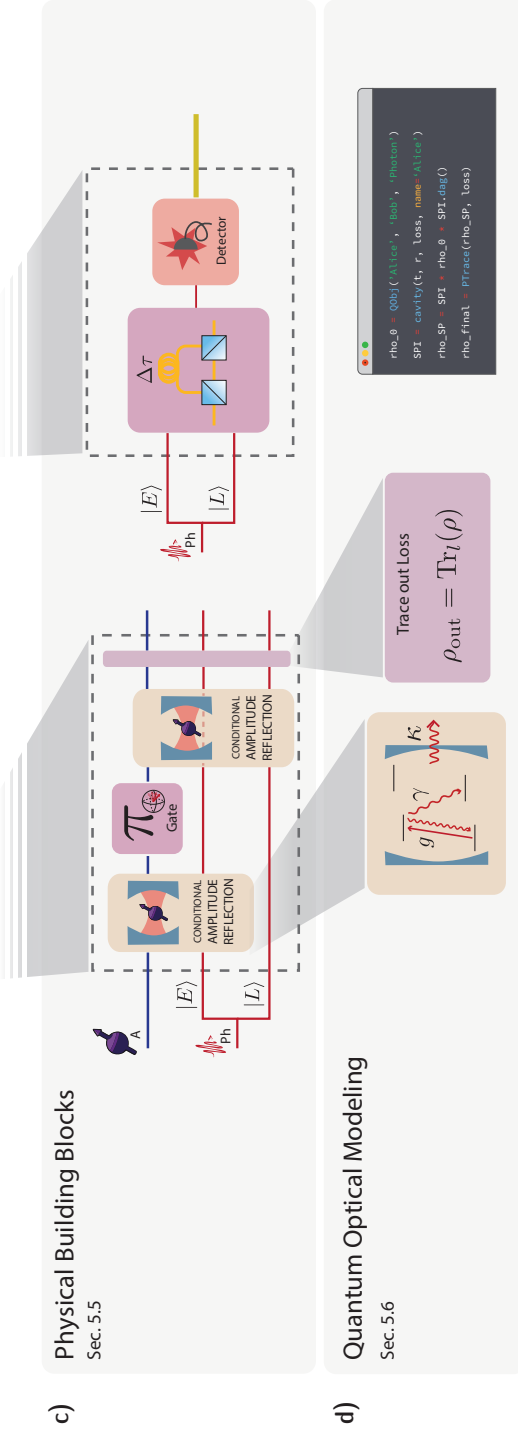


Figure 5.1: An overview of remote-entanglement-protocol modular framework. Entanglement link - The objective of entanglement protocols is to entangle two remote spins (purple) where the entanglement is created by photons (red). (a) **Logical Building Blocks and Topology** (Sec. 5.3) - The topology for remote entanglement generation is deconstructed in logical building blocks (LBBs). From left to right, we consider three main REP topologies: the detection-in-midpoint, sender-receiver, and source-in-midpoint topologies. (b) **Encoding** (Sec. 5.4) - The encoding layer chooses the basis for the photonic qubits and the levels for the spin qubit. We illustrate the time-bin encoding of sender-receiver topology with spin-photon gates. (c) **Physical Building Blocks** (Sec. 5.5) - The physical building blocks (PBBs) are the quantum channels describing the operations of the physical systems including imperfections. This layer shows the REP at the physical level. The first panel describes the construction of spin-photon gates with an overcoupled cavity-QED system for state conditional amplitude reflection. The second panel shows the implementation of a measurement of the time-bin qubit in the X basis, using a Mach-Zehnder interferometer (see Figs 5.3 and 5.4). (d) **Quantum optical modeling** (Sec. 5.6) - This layer models the hardware used in the PBB. In this example the relevant parameters for the PBBs (e.g. the state-dependent reflection coefficient, $r_{|0\rangle,|1\rangle}$) can be calculated from physical variables (e.g. the spin-cavity coupling rate, g) using a detailed quantum optical model. We implemented these descriptions in a software package publicly available on GitHub (Sec. 5.7). Sec. 5.8 shows the simulation and benchmarking results with our framework.

In the third layer, we get closer to the hardware and implement the protocol in physical building blocks (PBBs). We implement the LBB with the desired hardware and encoding in PBBs as shown in Fig. 5.1(c). This requires the idealized quantum operations of the LBB to be compiled to the available PBBs. For example, in Figure 5.1, the spin-photon interface block is implemented as three PBBs, namely, the reflection of the early time bin, a single-qubit rotation, and a reflection of the late time bin. The PBBs are a native operation for the hardware and are modeled as a quantum channel.

The final layer is quantum optical modeling, where the exact physics of PBBs are modeled. This layer is added to reuse the quantum modeling of a system for different PBBs. For example, a critically coupled or an overcoupled cavity both require the same quantum optical modeling but are used in different PBBs.

5.3. LOGICAL BUILDING BLOCKS AND TOPOLOGY

5

The first layer of our framework is the choice of protocol topology and its description in terms of logical building blocks (LBBs). The operation of the protocol topology can be described by the circuit diagrams (Fig. 5.2(a)). LBBs are high-level quantum operations in a quantum network that can be chained together to form an entanglement protocol, such as photon sources, spin-photon emission, and photon detection. In Fig. 5.2(b), we show how LBBs compare to elementary circuit diagrams, and in Fig. 5.2(c), how they can be used to construct different protocol topologies. The LBBs are not hardware-specific, as the practical details on what generates this operation and the dependence on physical parameters are described in the physical building block layer.

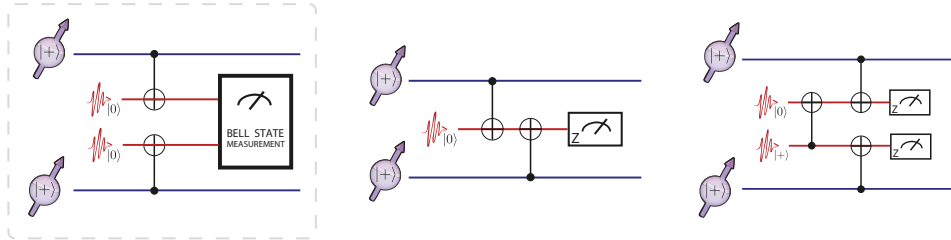
5.3.1. TOPOLOGY OF THE PROTOCOL

In this work, we consider three topologies for REPs, described in Fig. 5.1(a); namely, detection-in-midpoint (ingoing), sender-receiver, and source-in-midpoint (outgoing) [28].

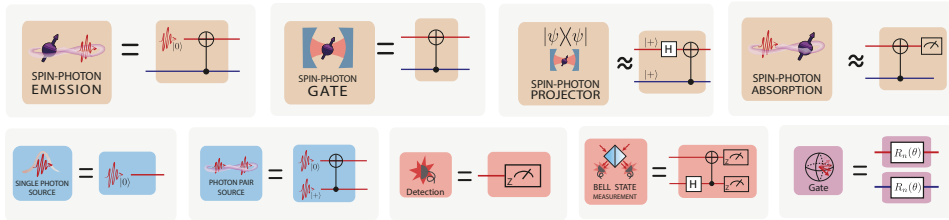
In the detection-in-midpoint topology, both end points generate spin-photon entanglement. The photons are then measured in the middle, in an entangled basis using a Bell-state measurement. This projects the two spins in an entangled state. The detection-in-midpoint topology has an advantage in its simplicity. At its most basic, this topology requires only photon emission from the spins, beam-splitter interference of the photons, and single-photon detections at the central station. Efficient spin-photon interfaces such as optical cavities, while helpful, are not necessary to get high-fidelity entanglement. Furthermore, the time overhead for classical communication is reduced by half compared to the other topologies, since the end points communicate solely with the detection point, eliminating the need for direct communication between them.

In the sender-receiver topology, the first end point generates spin-photon entanglement, and the photon is then sent to the second end point, where it interacts with the spin, such that entanglement between the spins is achieved. This interaction

a) Protocol topology operation as circuit diagrams



b) Logical Building Blocks and corresponding circuit diagrams



c) Different LBB implementation of the same topology

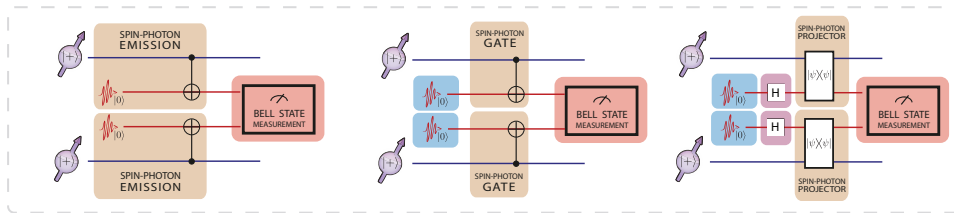


Figure 5.2: **The remote-entanglement-protocol topologies and logical building blocks (LBBs).** (a) The three available topologies for REP — detection-in-midpoint, sender-receiver topology, and source-in-midpoint — and depiction of their operation with circuit diagrams. Here we use the notation $|+\rangle = (|0\rangle + |1\rangle)/\sqrt{2}$. (b) The LBBs available to construct the REP. The circuit description outlines their idealized operations, which the user can match with the diagrams in (a). For the spin-photon projector and the spin-photon absorption, an approximate gate diagram is given. This can be used to see how they can be used in the quantum circuits in (a). The exact gate description for these LBBs would be a projector operation and a SWAP gate. (c) Three different implementations of the midpoint detector, as an example. In this case, the spin-photon emission, spin-photon gate, and spin-photon projector are used as the spin-photon interface, respectively.

can be a gatelike behavior (e.g., by using an optical cavity) after which the photon is measured. Alternatively, the photon can be absorbed by the spin-photon interface in which case this topology matches the workings of quantum state transfer [17, 29]. The sender-receiver topology does not necessitate an intermediary station for the spins to become entangled. However, the classical communication time for the heralding signal is twice as long compared to a detection-in-midpoint topology, as it needs to travel the full distance as opposed to half of it.

The source-in-midpoint topology has an entangled photon source in the middle that sends these photons to the end points. The end points have an entangling interaction between the spin and the photon, after which the photons are measured and the spins will be projected into an entangled state. The source-in-midpoint topology is useful in satellite-assisted entanglement protocols. The ground-to-satellite channel (uplink) has a higher overall loss than the satellite-to-ground channel (downlink). Phenomenologically, this phenomenon is collectively referred to as the “shower-curtain effect” of the atmosphere [30]. In particular, the diffraction and deflection by air turbulence are more severe in the early stage of transmission than in the late stage on the dispersed beam. Moreover, practical factors such as limited onboard optics on the satellite result in a larger pointing error in the uplink than in the downlink [31].

Remote entanglement between two stationary qubits has been experimentally realized with sender-receiver topology using trapped atoms embedded in optical cavities [32], and with detection-in-midpoint using several platforms including nitrogen-vacancy (NV) centers in diamond [21], quantum dots [19], trapped ions [16], and atoms [18].

5.3.2. SPIN-PHOTON-INTERFACE BLOCKS

The key logical building block of an REP is the spin-photon-interface block since this is the interaction between the stationary and flying qubits. In this work, we focus on REPs that are heralded, using single-photon detection to screen out photon-loss errors. Absorption-based spin-photon interfaces generally allow heralding only through additional energy levels in the stationary qubit [17]. Thus, we give only a cursory treatment of absorption-based spin-photon interfaces. We identify four main categories of spin-photon-interface blocks, as follows.

Spin-Photon Emission. A spin-photon-emission block creates a photonic qubit entangled with the qubit state of the spin by emission through a higher-level excited state. This is commonly achieved by the emission of a photon after spin-dependent excitation with a laser pulse. As an example, optical excitation of a spin in a superposition state will emit a photon depending on the spin state, $\frac{1}{\sqrt{2}}(|0\rangle_s + |1\rangle_s) \xrightarrow{\text{laser}} \frac{1}{\sqrt{2}}(|0\rangle_s + |\text{excited}\rangle_s) \rightarrow \frac{1}{\sqrt{2}}(|0\rangle_s |0\rangle_p + |1\rangle_s |1\rangle_p)$, where the subscript s (p) labels the state of the spin (photonic mode) and $|1\rangle_s$ is the bright state of the spin that is excited and emits a single photon. Alternatively, the system can be brought to an excited state in which two different decay channels lead to two different spin states. The emitted photons can, e.g., have a differ-

ent polarization entangled with the spin state. Various optically active quantum systems have realized spin-photon emission through spin-dependent optical excitation or decay to different spin states, including NV centers in bulk diamonds [33], neutral atoms [34], trapped ions [16], and quantum dots [19].

Spin-Photon Gate. A spin-photon-gate block is a conditional gate between the spin and a photon. Depending on the exact implementation, this will act as a controlled-Z or controlled-X rotation on the photonic qubit. Spin-photon-gate blocks require a strong coupling of photons with the stationary qubit, and this is realized by confining the light with photonic cavities or waveguides. In some cases, the need for strong coupling can be relaxed at the expense of a nondeterministic but heralded gate operation. Examples of practical implementation of spin-photon-gate LBB are trapped atoms in Fabry-Perot cavities [32], SiV centers in diamond photonic crystal cavities [35], and quantum dots in photonic crystal waveguides [36].

Spin-Photon Projector. A spin-photon-projector block selects only specific states from the input state. With the right input state and the right selection, this results in spin-photon entanglement. This method is sometimes referred to as "carving" [37]. An example is where the input state is in a superposition for both the photon and spin qubit (note that the $|0\rangle_p$ is referring to the qubit state, not the vacuum state), $\frac{1}{2}(|0\rangle_s|0\rangle_p + |0\rangle_s|1\rangle_p + |1\rangle_s|0\rangle_p + |1\rangle_s|1\rangle_p)$, and the spin-photon interface has a photonic loss that depends on both the spin and photon state. In this example, a spin-photon interface that has photon loss for the photon in the scenarios $|0\rangle_s|1\rangle_p$ and $|1\rangle_s|0\rangle_p$ would create, with a 50% chance, the state $\frac{1}{2}(|0\rangle_s|0\rangle_p + |1\rangle_s|1\rangle_p)$. So heralding no photon loss by photon detection ensures that only (an entangled) part of the incoming state is selected. This approach has been used for entangling two neutral atoms in a cavity [37] and with silicon-vacancy centers in diamond photonic crystal cavities for the demonstration of an asynchronous Bell-state measurement between two photons [35]. The downside is that it has intrinsic losses as it rejects part of the incoming state rather than performing a deterministic gate.

Spin-Photon Absorption. The spin-photon absorption block transfers the photon state to the spin state. The block often implements a strong interaction using a cavity [38] or a spin ensemble [39]. The absorption of a photon from lossy channels results in the vacuum field and does not herald the entanglement by photodetection, resulting in low fidelities. Instead, spin-photon absorption can be useful if used carefully. For example, one can read the spin state after the absorption, effectively constructing a heralded protocol. Alternatively, one can make a high optical-depth spin ensemble absorb a single photon from a photon-pair source and use the other photon from the source [40]. If the channel loss is negligible, the spin-photon absorption can directly implement quantum state transfer without classical communications [41].

5.3.3. PHOTON BLOCKS

Photon source. Photon source blocks can be considered as the initialization of photonic qubits. High-rate entanglement generation with photon sources requires the deterministic generation of single photons with high-efficiency quantum emitters [42, 43] or photon-pair generation followed by the heralding [44]. For high fidelities, single photons need to be indistinguishable, which is often challenging in a solid-state environment [45–47]. The distinguishability problem is considered in the quantum optical modeling layer.

Photon-pair sources. Photon-pair sources provide entangled photon pairs, which can be used for REPs with source-in-midpoint topology. This can be understood as two photons initialized in an entangled state. Midpoint on-demand entangled photon-pair sources have been proposed based on correlated photon decay from quantum emitters [28], mode mixing of single photons [48] or multiplexing spontaneous pair sources [49]. We note that at the LBB level, photon-pair sources output perfect Bell states in the logical basis, $|0\rangle$ and $|1\rangle$. The photonic basis of the states is determined in the photonic encoding layer (Sec. 5.4) and imperfections, such as probabilistic photon-pair generation, are detailed in the quantum optical modeling of PBBs (Sec. 5.6).

Photon measurement. Generally in the REPs, the photon is still entangled with the spins before detection. For example in the sender-receiver topology (middle circuit of Fig 5.2(a)), the state before the measurement is

$$\frac{1}{2} (|0\rangle_p (|00\rangle_{AB} + |11\rangle_{AB}) + |1\rangle_p (|01\rangle_{AB} + |10\rangle_{AB})), \quad (5.1)$$

where A and B refer to the two separate spins. This means that the photon needs to be measured on a basis that preserves entanglement between the spins — this is in the Z basis for this situation. In this measurement of the photonic qubit, the outcome heralds a different entangled state on the spins; in this example, measurement of $|0\rangle$ for the photon heralds $\frac{1}{\sqrt{2}}(|00\rangle + |11\rangle)$. One can choose to feed back on one of the spins to always generate the same entangled state or use the measurement outcome in postprocessing.

Bell-State Measurement. Photonic Bell-state measurement projects the state of two photons into one of four Bell states, $|\Psi^\pm\rangle = |01\rangle \pm |10\rangle$, $|\Phi^\pm\rangle = |00\rangle \pm |11\rangle$. When it is required to have a quantum operation between two photons — e.g., in the detection-in-midpoint topology — the Bell state measurement can be used. This is advantageous, as in linear optics the photons do not interact. This can be achieved with a beam splitter and photon measurement after the beam splitter. The Bell-state measurement projects two photons into an entangled state. It is usually used for entanglement swapping of two spin-photon-entangled pairs to yield entangled spins. Note that the Bell-state measurement with linear optics is probabilistic, with only a 50% chance of succeeding. However, with auxiliary single photons, one can boost the success probability to 75% [50]

Photon gates. Gates on the photonic qubit are essential in some entanglement protocols. How easily these can be implemented depends completely on the photonic encoding used and this is discussed in Sec.5.5.1.

5.3.4. SPIN BLOCKS

Operations on the spin such as initialization, gates, and measurements are their own logic building blocks. They are the standard set of initialization, qubit gates, and qubit measurement [27]. In some cases, entanglement protocols require the spin to be initialized and put in a superposition for each entanglement attempt.

5.3.5. OTHER LOGICAL BUILDING BLOCKS

The blocks discussed earlier are the logical operations required for the working of the REPs. On top of these there are processes that in an ideal scenario do not do anything to the photonic and spin qubits. Their implementation will, however, add noise; e.g., a photonic loss in a fiber or quantum frequency conversion of the photons. These blocks do not change the logical states of qubits in the ideal situation, so they appear as identity operators in the circuit diagrams of the LBB layer and they can be modeled in detail as PBBs. For example, a photonic loss block can be added, which takes care of the losses in the system: this does not change the ideal operation of the protocol but will impact the rate and fidelity in the simulations (which is implemented in the PBB).

For a long-distance entanglement generation, it is advantageous to use photons in the telecom band to improve photon transmission using ultralow-loss fibers. As the physical platforms used for spin-photon interfaces have limited access to those wavelengths, quantum frequency conversion [51, 52] is often used to match the photon wavelength of the spin-photon interface with the desired communication band. In this case, one can model and add a frequency-conversion block to protocols.

5.3.6. COMBINING TOPOLOGY AND LOGICAL BUILDING BLOCKS

In a given topology, a user can implement different combinations of LBBs. Figure 5.2(c) demonstrates the detection-in-middle topology implemented with the spin-photon emission, gate, and projector logical building blocks.

5.4. ENCODING

In Sec 5.3, the ideal operation of an REP has been outlined. To translate this to the quantum hardware, the abstract spin and photonic qubits need to be encoded in the desired and available spin and photon levels. In this section, the photonic encodings are discussed in detail, as these are very general. The spin encoding is much more platform dependent and therefore is discussed more briefly.

5.4.1. PHOTONIC ENCODING

Optical photons are the best option to send quantum information over a long distance for remote entanglement. Quantum information can be encoded into a photon using

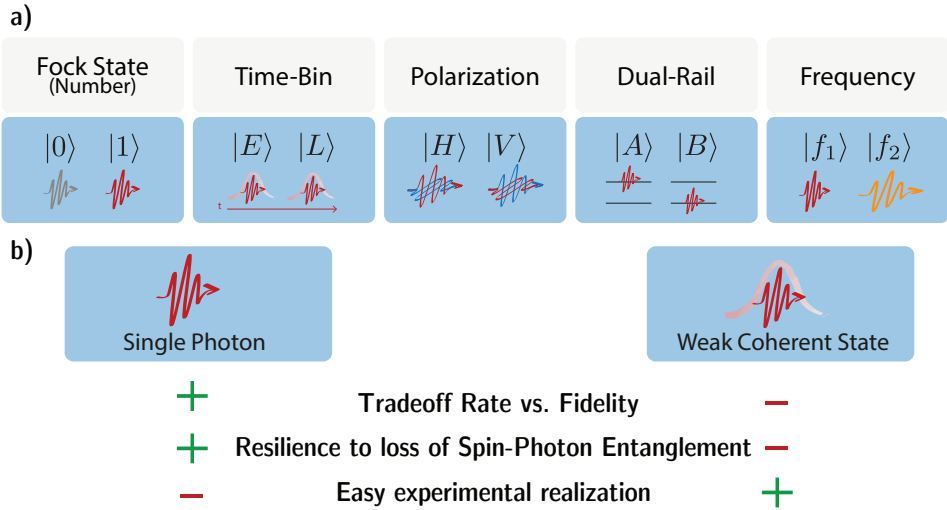


Figure 5.3: **The encoding of photonic qubits.** (a) The basis states of photonic encoding. (b) In every basis choice, the basis can be implemented with single photons or those can be approximated with a weak coherent state.

various degrees of freedom: amplitude (Fock-state encoding), timing (time-bin encoding), spatial modes (dual-rail encoding), polarization (polarization encoding), and frequency (frequency encoding) (see Fig. 5.3). In the literature, dual-rail encoding can also refer to general two-mode encodings; e.g., time-bin and frequency encoding. In this tutorial, we will use the term “dual-rail” exclusively for the encoding into spatial modes. Each of the encoding schemes has two states acting as the qubit basis. In general, the other degrees of freedom are kept the same to simplify the operations and allow for the interference of encoded photons for a Bell measurement, which requires indistinguishable photons unless precise measurement of conjugate variable is available and the measurement result is mutually unbiased (for frequency-mismatching case see, e.g., Refs. [53, 54]).

PHOTON NUMBER OF THE PHOTONIC QUBIT

All encoding except Fock-state encoding have a single photon in the basis states. The advantage is that the loss of photons can be detected. The entanglement protocols discard the cases with photon loss for high-fidelity entanglement generation, so-called heralded entanglement [21, 22].

As high-efficiency indistinguishable single-photon sources are technologically demanding, the single photons are frequently replaced with weak coherent sources (attenuated lasers). They have Poisson statistics with a small mean photon number, well below one. The wave function of a weak coherent state is dominantly vacuum ($|0\rangle$), with a small fraction of single-photon state ($|1\rangle$) and an even smaller fraction of two-photon states

(|2⟩):

$$|\alpha\rangle \propto |0\rangle + \alpha|1\rangle + \frac{\alpha^2}{\sqrt{2}}|2\rangle + \dots \quad (5.2)$$

where α is the complex amplitude and $|\alpha|^2 \ll 1$ is the mean photon number. The vacuum component $|0\rangle$ reduces the rate of entanglement generation, since it cannot herald entanglement through photodetection. The $|2\rangle$ state reduces the fidelity of the spin-photon entangled state, as the loss of one of the two photons leaks information to the environment. There is, therefore, a trade-off between rate and fidelity for choosing α , when using weak coherent states as approximate single-photon states in heralded-entanglement-generation protocols.

ENCODING BASIS

Fock-state encoding. Fock-state encoding stores quantum information in the photon-number eigenstates with zero photons and one photon ($|n=0\rangle$ and $|n=1\rangle$, where n is the photon number). $n > 1$ states are not considered in the encoding due to technical difficulties in preparing those states. However, the problem is that loss takes one qubit state to the other and therefore directly impacts the fidelity (compared to other encodings where loss can be detected as the vacuum state is not part of the encoding space). The relative phase of the two bases evolves as the optical phase, so the optical path length needs to be stabilized or at least known for correction. Despite these complications, Fock-state encoding has a significant advantage in that Bell measurement is possible with the detection of a single photon, while the other encodings need the detection of two single photons. The success probability of a heralded protocol scales linearly with the probability of photon loss if only single-photon detection is needed, while it scales quadratically for two-photon detection (in all but Fock-state encoding). In cases in which photon losses are significant, due to long-distance transmission or devices with low efficiency, the linear scaling given by Fock-state encoding can provide a key advantage over other encodings.

Time-bin encoding. Time-bin encoding counteracts the drawbacks of Fock-state encoding at the expense of the requirement of two-photon detection for Bell measurement. Two time bins (early and late) are chosen to encode the photons. Photon loss can always be detected, in the ideal case of detectors with no dark counts, as this would result in no detection of photons. Therefore, the fidelity of protocols with time-bin encoding is not compromised, as long as dark counts are negligible with respect to the signal but the rate decreases. Another advantage is relaxed phase stability: the optical phases should be stable on the time scale of the spacing of the time bins. However, arbitrary qubit operations are hard to implement but the encoding is quite robust against noise sources such as dispersion or birefringence in the transmission medium. Therefore, this encoding is mostly used in sending quantum information over long fibers and not in situations that require full control over the photonic qubit state [55].

Polarization. The polarization encoding defines the qubit state in two perpendicular polarizations: horizontal (H) and vertical (V), diagonal (D) and anti-diagonal (A), or left (L) and right (R) circular. Single-qubit gates are easily implemented, as all single-qubit

rotations can be performed with wave plates (see Sec. 5.5.1). Moreover, polarization encoding requires phase stability between the two polarization bases. This stability can be readily attained in free space. In single-mode optical fibers, the polarization is preserved but temperature and stress fluctuations in the fiber can rotate the polarization: stabilization and calibration are therefore required. Polarization-maintaining (PM) fibers decouple the two different polarization bases by using orthogonal modes with different effective indices. This preserves only the amplitude in each basis and not the phase relation between them. In remote-entanglement experiments using polarization encoding, single-mode fibers are usually used [32, 56].

Dual-rail encoding. The dual-rail encoding uses two spatial modes for photons. This encoding has one significant drawback, as it requires twice the physical elements. The phase between two separate paths is extremely stable on the integrated photonic device; however, in fiber or free space, the requirements are comparable to those for phase stabilization for Fock-state encoding. This encoding can implement operations that are hard to perform in another encoding because path separation gives the most flexibility to use optical elements separately in two modes (see Sec. 5.5.1).

5

Note that in some literature the term “dual-rail encoding” is used to refer to a single excitation out of two orthogonal bosonic degrees of freedom, encompassing spatial modes, polarizations, time bins, frequencies, wave vectors, and orbital angular momentum. In these instances, “Fock-state encoding” is referred to as “single-rail encoding” [55]. In this tutorial, we use “dual-rail encoding” specifically for the single excitation in two spatial photonic modes and specify the degree of freedom in other cases.

Frequency encoding. In frequency encoding, photonic qubits utilize two distinct frequency modes as basis states. Single-qubit gates in frequency encoding require nonlinear optical devices such as electro-optic modulators that suffer from low efficiencies. To measure frequency-encoded photons, the frequency separation of two frequency modes must exceed the spectral resolution of a grating or a cavity. One can also directly detect a frequency-encoded photon in a time-separated manner by using group-velocity dispersion in optical fibers [57] or Bragg gratings [58]. Note that group velocity-dispersion does not convert the frequency encoding to time-bin encoding. Even if a photon of one frequency is time shifted relative to a photon of another frequency, the two photons still occupy distinct frequency bins.

5.4.2. SPIN ENCODING

Besides the photonic qubit, the spin qubit also needs to be encoded in the physical states of the system. The encoding of the stationary qubit depends on the system at hand. An important requirement for the spin-photon interface is that at least one of the states has an efficient and stable optical transition. Besides, there should be ways to initialize, control, and read out with high fidelity. Lastly, the coherence time of the qubit should be long enough to bridge at least the time of flight of the photons to the midpoint or another quantum node, as this allows for heralded-entanglement generation, which is required for applications beyond point-to-point quantum key distribution [3]. Examples of the

levels that are used to encode the spin qubit in various systems are the electronic spin for NV centers in diamond [21] or cold atoms [17], spin-orbital hybrid states for group-IV centers in diamond [35], hyperfine levels in trapped ions [16], and angular momentum states in quantum dots [19].

5.5. PHYSICAL BUILDING BLOCKS

After the REP topology is constructed with LBBs and the encoding is chosen, we can construct the REP with the physical systems that are available. The LBBs are ideal circuit elements acting on the qubits of photons and spins, while the PBBs are physical processes on the optical modes (e.g., early and late) and spin states. Therefore, the PBB layer translates the abstract operations to allow hardware implementation.

For example, to generate spin-photon entanglement, a spin-photon-interface LBB can be composed of several PBBs that perform operations on different photonic states. As shown in Fig. 5.1, a spin-photon-interface LBB with time-bin encoding consists of a conditional-amplitude-reflection PBB in early mode, a qubit-rotation PBB on the spin, and a conditional-amplitude-reflection PBB acting again on the late mode.

5.5.1. PHOTON OPERATIONS

The PBBs of the photonic operations are described in Fig. 5.4. Polarization and dual-rail encoding are convenient with regard to the implementation of quantum gates and are often used in linear optics quantum computation [59]. The photonic PBBs, of which we describe photonic loss, mode mixing, and photodetection in Sec. 5.6.3, are often studied in standard quantum optics textbooks.

MEASUREMENT

Measurement in all photon encodings is done by means of single-photon detectors. Fock-state encoding can be measured directly. However, a single-photon state ($|1\rangle$) after photon loss cannot be distinguished from the vacuum state ($|0\rangle$). Time-bin encoding requires time-resolving detectors. Polarization and frequency-encoded qubits cannot be detected directly and are usually converted to dual-rail (see Sec 5.5.1) where both modes are then measured with a separate detector.

PHOTON GATES

An arbitrary gate can be made with the combination of rotations around the X and Z axes of the qubit Bloch sphere. For a Z rotation, the phase between the qubit basis states needs to be changed. Also, this is directly the phase that needs to be stable for the use of the encoding. For an X rotation, the operation needs to change the basis states. This can be readily implemented for polarization encoding with waveplates. For a Fock state encoding, this is not trivial and has not been demonstrated to the best of our knowledge, and the time-bin needs to be converted to dual-rail. In dual-rail encoding a Mach-Zehnder interferometer is used.

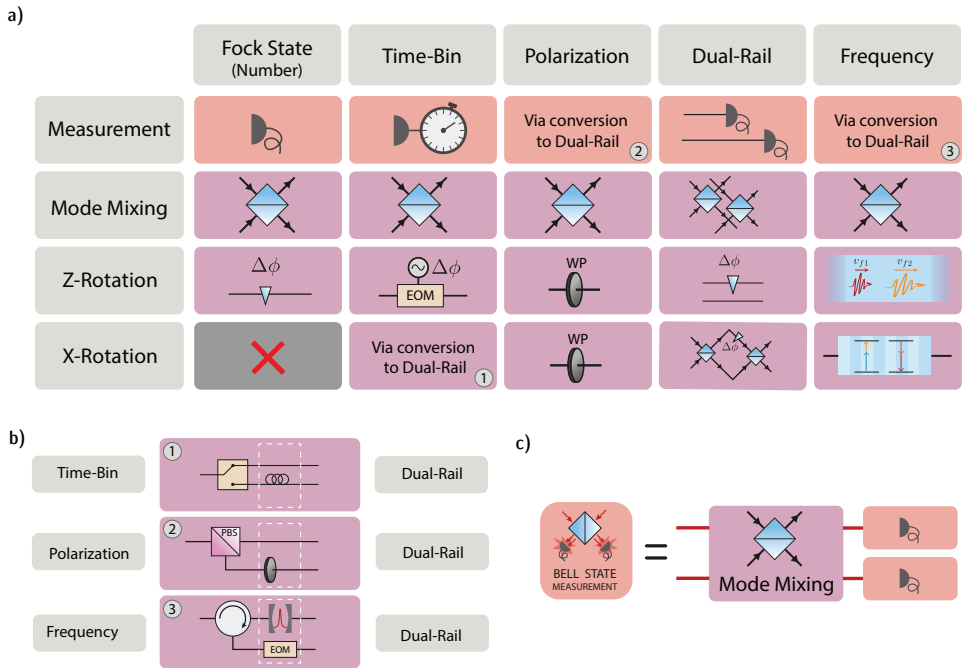


Figure 5.4: **The photonic PBBs for the different photon encodings.** (a) Each basis has its own implementation of the quantum operations, but some do not have natural implementation without converting them to a different basis (usually to dual-rail). The *measurement* in the computational basis is performed with a single-photon detector. For time-bin encoding, it needs to be time resolved. For polarization and frequency, the qubit is usually converted to and detected in dual-rail encoding. Two-qubit gates are implemented using *mode mixing* with a beam splitter. The mode mixing lets two photonic qubits interfere with each other. For a *Z rotation* the phase between the two basis states needs to be altered. This is implemented in Fock-state encoding with a delay line, in time-bin encoding with an electric optic modulator (EOM) shifting one time-bin, in polarization encoding with a wave plate, in dual-rail encoding with delaying one of the lines, and in frequency encoding with a dispersive medium. The *X rotation* requires changing the photon between the two eigenstates, which is not feasible for Fock-state encoding, goes via dual-rail for time-bin encoding, can be easily implemented with a wave plate in polarization encoding, and uses a Mach-Zehnder interferometer for dual-rail and nonlinear processes for frequency encoding. (b) The conversion between the basis that can be used for the easier physical implementation of quantum operations. Fock-state encoding cannot easily be converted. All other encodings can be converted to and from dual-rail. For this, one element adds a new encoding (switch, PBS, or cavity or grating), and another removes the old encoding (in the white dashed box, a delay, wave plate, or frequency-shifting EOM). The latter can be omitted if the photon is detected afterward, as no indistinguishability is required. (c) The LBB of Bell-state measurement can be constructed using mode mixing and single-photon detection in each of the encodings.

BELL-STATE MEASUREMENT

The Bell-state measurement can be performed with linear optics with a 50% success probability [55]. It can only detect the $|\Psi^\pm\rangle = |01\rangle \pm |10\rangle$ state, as it requires the detection of both modes after the beam splitter. The $|\Phi^\pm\rangle = |00\rangle \pm |11\rangle$ state cannot be detected as measuring the same modes after the beam splitter reveals both their individual states. The Bell-state measurement is done by using a beam splitter for mode mixing and two detectors to tell which of the two detectable entangled states ($|\Psi^+\rangle$ or $|\Psi^-\rangle$) has been measured (Fig 5.4(c)).

CONVERSION BETWEEN ENCODINGS

Figure 5.4(b) shows the possible conversion between the encodings. In practice, dual-rail encoding is a versatile encoding that can be converted directly into the others and vice versa. For the conversion, one needs the separation of the photons in different modes into different spatial paths (e.g. using a polarizing beam splitter) and compensating elements to remove the character from the previous encoding (e.g. using a wave plate). The compensation can be omitted if one does not need indistinguishable photons after conversion; e.g., if the photons are detected directly.

The conversion between time-bin encoding and dual-rail is used often as this is the only viable way to perform X gates on the photonic qubit. In this case, the switch is often replaced by a beam splitter by accepting the 50% loss, as this reduces the complexity of the experiment and as the time delay between time bins can be short compared to the switching time. When using a beam splitter, there are also possible optical paths involving the unwanted output ports that cause the photon to be delayed and fall outside of the defined time-bin window; however, these cases can be discarded upon measurement using time-resolving detectors.

5.5.2. SPIN OPERATIONS

The exact PBB spin operations depend considerably on the chosen spin encoding. We discuss the most common ones below.

INITIALIZATION

Initialization of the spin is usually achieved in one of the following ways. When a nonperfectly cycling optical transition is present, which means that under continuous driving there is a (small) probability of spontaneously decaying to a different state than the ones involved in the transition, it is possible to use optical pumping [60]. By laser excitation of the noncycling transition, the system will eventually decay to the desired qubit state and remain there, as this is not driven by the laser. In systems with a very good readout, it can be advantageous to read and generate the desired initialized state with a control pulse conditional on the readout result [35]. If one wants to prepare the system in a superposition a quantum gate can be used. Alternatively, one can prepare a state by stimulated Raman adiabatic passage (STIRAP) [61].

CONTROL

Quantum control of the qubit is usually achieved by direct Rabi driving of the transition. This is usually a microwave [25] or optical field but it can also be done with other

coupled fields, such as an oscillating strain field [62]. If the transition frequency is experimentally hard to reach or is only weakly allowed, two driving fields in a lambda configuration can be used, in which the qubit states are coupled to a common excited state. By driving both transitions, a coherent rotation on the qubit can be achieved with a two-photon Raman transition [63]. In some systems, mostly based on solid-state implementations, coupling to fluctuating magnetic fields in the surrounding environment, such as nuclear spin baths, can affect the coherence of spin-based qubits. With the control in place, it is usually possible to extend the coherence time of the spin qubit in these platforms by means of dynamical decoupling [64].

READOUT

The qubits that we are considering have a good spin-photon interface, which allows for optical readout of the spin. The spin can be read out by the detection of the state-dependent fluorescence. For high fidelity of this readout, a high collection efficiency and good cyclicity of the optical transition are needed. A good cyclicity results in a transition that can be driven for a long time, generating as many photons as possible before the qubit decays to an unwanted state [65], while a high collection efficiency allows for measuring enough photons for a high-fidelity readout with a shorter driving time and lower probability of the qubit changing state. When a conditional-phase-reflection PBB (see Sec. 5.5.3) is used, the spin state can be read out by phase readout [66].

5

AUXILIARY QUBITS

To go beyond a single entangled link, it is essential to have auxiliary qubits for storage of quantum states in the system [67]. This is required for, e.g., entanglement distillation [68–71] and entanglement swapping in repeater schemes. The available auxiliary qubits are highly dependent on the system and can go from nuclear spins in solid-state emitters to different species of atoms or ions in those systems. The most difficult requirement to fulfill for these qubits is often that they need to be resilient for entanglement attempts on the spin qubit, which typically involves a lot of initialization and control pulses. This can result in a competition between the coupling required for two-qubit gates and the isolation required for resilience during entanglement attempts [60].

5.5.3. SPIN-PHOTON INTERFACE

The spin-photon interface is an essential part of the entanglement protocols, as it connects the stationary and flying qubits. We discuss five different spin-photon-interface PBBs (see Fig 5.5). The first three are suitable to make spin-photon entanglement for a spin-photon-emission LBB: spontaneous emission, coherent scattering, and Raman scattering. These PBBs are all controlled with a classical laser control pulse and the output is a single photon (or a weak coherent state depending on the exact implementation) entangled with the spin. When the interaction between the light and the emitter is very strong, we can get a reflection of a single-photon or weak coherent state in which the amplitude or phase of the reflected light is controlled by the spin state. The conditional-amplitude-reflection or conditional-phase-reflection PBB can be used to build the LBB of a spin-photon projection or a spin-photon gate.

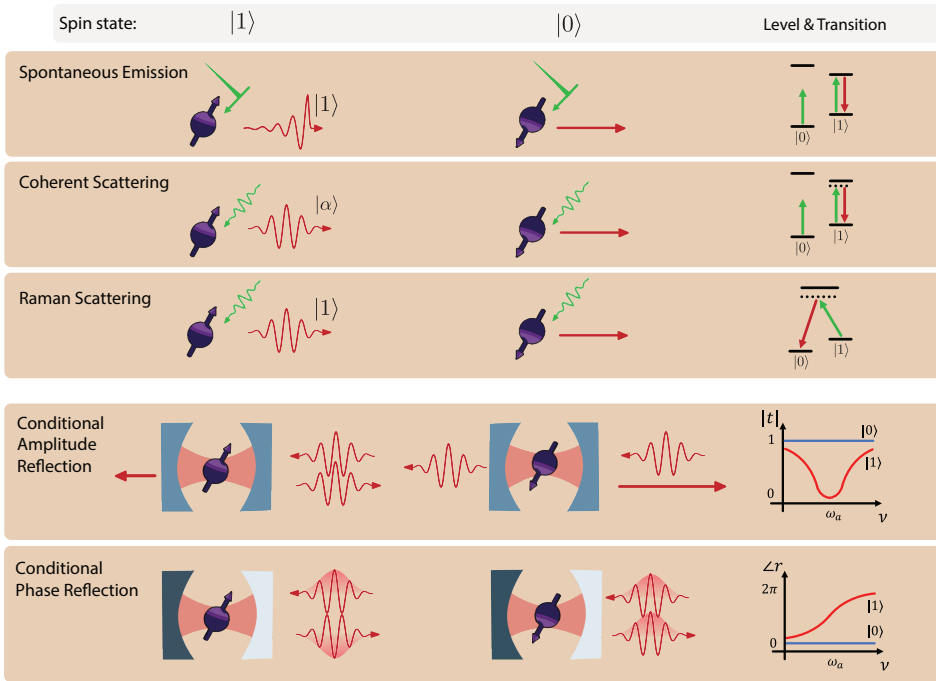


Figure 5.5: **Spin-photon interface PBBs.** State-selective optical transitions as spin-photon interfaces. For the *spontaneous-emission* spin-photon interface, the excitation pulse is much shorter than the optical lifetime and excites the $|1\rangle$ transition: it will emit a single photon by spontaneous emission. The *coherent-scattering* spin-photon interface scatters a weak pulse from the $|1\rangle$ optical transition, resulting in a photon with a weak coherent state. The *Raman-scattering* spin-photon interface is excited with a pulse but as the optical excitation ends up in a different spin state only a single photon is emitted. In the **conditional-phase-reflection** spin-photon interface a photon is reflected from the cavity with a coupled spin. For $|1\rangle$, the phase is flipped and therefore entangled with the spin state. An overcoupled cavity is used for this purpose. In the *conditional-amplitude-reflection* spin-photon interface, the photon is transmitted or reflected depending on the spin state. A critically coupled cavity is used for this case.

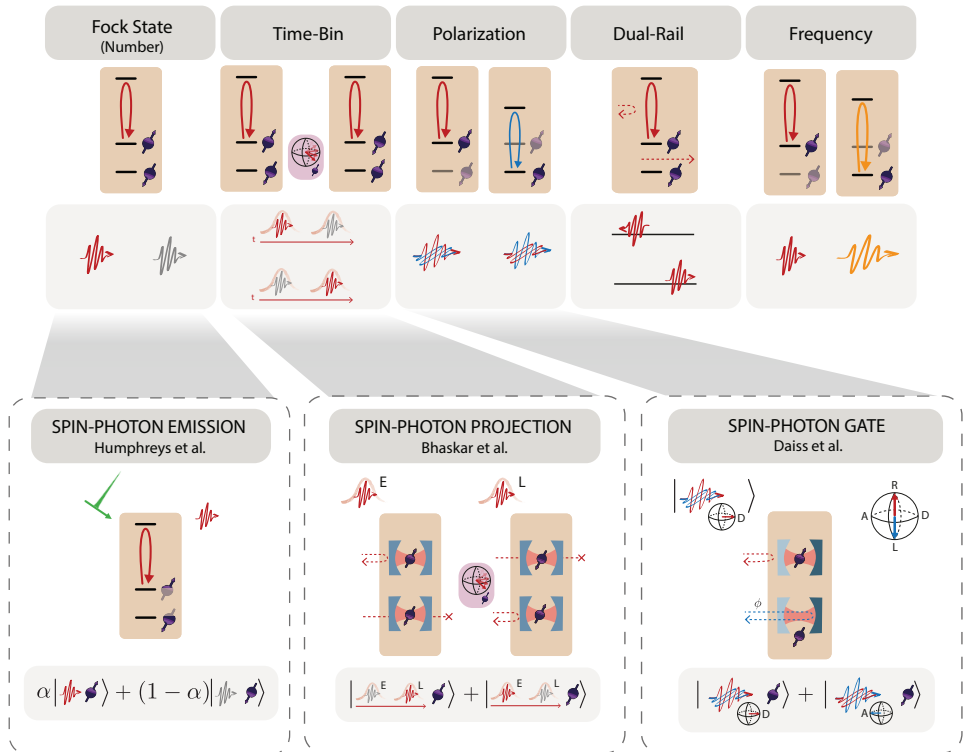


Figure 5.6: **Spin-photon interface PBBs.** A schematic example of how a spin-photon-interface LBB can be implemented in the different photonic encodings, starting from a spin-photon PBB. Below are examples of experimental realizations of the emission [22], projection [35], and gate [32] LBBs in different encodings.

SPONTANEOUS EMISSION

The conceptually most simple way to implement a spin-photon interface is the emission-based spin-photon interface, where the spin-photon entanglement is generated through spontaneous emission. In this case, a short high-power optical π pulse is used to excite the system to the excited state. If this excitation or the spontaneous emission depends on the spin state we can create spin-photon entanglement.

With this PBB, we can create a spin-photon-emission LBB. For Fock-state encoding we prepare the spin in a superposition and apply a spin state-dependent optical π pulse such that the presence of a photon is entangled with only one of the spin states. For the time-bin encoding, we initialize the spin state in an equal superposition and apply the excitation twice with a π -pulse of the spin in the middle. For the polarization or frequency encoding, both spin states need to have an optical transition with a different polarization or frequency. The entanglement can either be generated by initializing the spin in an equal superposition and exciting both transitions or by relying on an optical transition that has an equal chance of decaying to either state, correlated with a different polarization or frequency. An example of polarization encoding can be found in Ref. [72].

The photon coming from such a process will have a frequency and exponential temporal shape determined by the optical properties of the emitter. The line width is determined by the lifetime and the inhomogeneously broadened line width and the indistinguishability are determined by the dephasing processes of the optical transition. This requires favorable properties of the emitter to make the photons suitable for entanglement generation. The optical π pulse needs to be much shorter than the optical lifetime; otherwise, in the case of fast spontaneous decay, the same pulse can cause reexcitation of the transition and a second photon emission, which can lead to an error in the protocol. On the other hand, it needs to be not too short, as this increases the line width of the excitation pulse and can therefore couple to and cause photon emission from unwanted off-resonant transitions that are close in frequency. A common method to separate the single photon from the excitation laser is to use the delayed emission of the photons compared to the arrival of the laser pulse. By delaying the detection window compared to the arrival of the excitation pulse, one can filter out the laser pulse in the time domain. This PBB has been used to make entanglement between NV centers [22] (see Fig 5.6).

COHERENT SCATTERING

In the coherent-scattering PBB a long and weak pulse is scattered elastically from the emitter. Under the condition that the exciting pulse is weak and long enough that, on average, only one photon interacts with the emitter within the optical lifetime, the scattered light will inherit the temporal shape, photon statistics, and frequency of the excitation field [67]. One can detune the laser from the emitter, making it more resilient to the spectral instability of the emitter. However, as the light has the same character as the laser, filtering the excitation light is experimentally much more challenging. This PBB allows for a spin-photon-emission LBB in a similar way to spontaneous emission.

RAMAN SCATTERING

The third way to make a spin-photon-emission LBB is to use the PBB of Raman scattering. In this case, the driving field and the emitted photon are coupled in a lambda scheme, where they both couple to a virtual state (see Fig 5.5, third row). In this inelastic scattering event, the temporal wave form and frequency are determined by the driving field, but now only a single photon is emitted. The driving field and the spontaneously emitted photons, which would act as noise sources, can be separated and filtered out from the scattered photons since they have different frequencies. There is usually a trade-off between efficiency and noise in this PBB by choosing the detuning of the virtual level from the excited state. This PBB has been used for entangling trapped ions over hundreds of meters [56].

Raman transition can be also used for spin-photon absorption. In this case, the spin absorbs the incoming photon with one transition and the other transition is driven so that the spin is in another state upon absorption. If there is no photon interacting with the first transition — e.g., because there is no photon or it is in a different polarization — then there is no change in the spin state, because the driving addresses the transition with no population.

CONDITIONAL AMPLITUDE REFLECTION

When the interaction between the spin and the photon becomes strong, a single spin can modulate the single photon. This is different from the three previous situations in which the driving field is “classical” and only the photon emitted or scattered is in the single-photon regime. As emitters have a limited dipole, the light field needs to be confined spatially to achieve strong interaction, which can be achieved in an optical cavity or a waveguide. In the conditional-amplitude-reflection PBB, the emitter acts as a quantum switch, reflecting the light if it is in one spin state while transmitting the light in the other spin state.

In the dual-rail encoding, this can clearly be used to realize a spin-photon gate, as the spin interacts directly with the two spatial paths. For the other photonic encodings, we can use this PBB to make the spin-photon-projector LBB: the photon is only reflected if the transition is on resonance and otherwise is lost. This PBB has been used to show an asynchronous Bell-state measurement with the silicon vacancy in diamond [35], where a time-bin photonic qubit and a nanophotonic optical cavity have been used (see Fig 5.6).

CONDITIONAL PHASE REFLECTION

To perform a spin-photon gate, the conditional-amplitude-reflection PBB works only for the dual-rail encoding. For the other encodings, the problem is that photons are lost in transmission depending on the spin state, which is not compatible with a spin-photon gate. To apply a spin-photon gate, we need an unconditional reflection of the photon. The conditionality of the interaction should therefore be encoded in the phase of the photon. This is achieved with an overcoupled cavity, where the back side of the cavity has a much higher reflectivity than the front, such that the photon will not be transmitted. The emitter will alter the cavity response in such a way that, depending on the spin state, the photon will be reflected on the cavity or will enter the cavity and leave

it again. When calibrated well, this can result in a π -phase-shift difference between the two types of reflection. The cavity can, in principle, also be replaced by a waveguide with a mirror at the end.

The conditional phase reflection with polarization-encoded photonic qubits has been the central PBB in the realization of a nonlocal gate with cold atoms in cavities [32] (see Fig 5.6).

5.6. QUANTUM OPTICAL MODELING

In the quantum optical modeling layer, the devices used are simulated at the quantum optics level. The aim of this layer is to calculate the action of the PBB on the photonic modes and spin states. The operations of the PBBs are modeled as quantum channels, which are completely positive trace-preserving maps. The PBBs map an input density matrix to an output density matrix. We emphasize that the mathematical modeling of PBBs can be done in different levels of detail. Thus, one can choose the PBB model as exhaustive or approximate depending on the purpose. The quantum optical modeling layer is separated from the PBB layer, as many PBBs rely on the same physical systems and therefore the same modeling; e.g., the conditional-amplitude- and conditional-phase-reflection PBBs both use an emitter coupled to a cavity. Moreover, the same PBBs can be modeled in different ways with different details. We will first discuss the intrinsic properties of the emitter, then how they can be enhanced and modified by an optical cavity, and, finally, the modeling of a couple of PBBs.

Using the modeling of a hardware-specific implementation, an REP can be benchmarked and optimized with respect to relevant experimental parameters. Having a realistic description of the building blocks also allows us to take into account noise sources and practical limitations.

5.6.1. EMITTER

For the spin-photon interface to perform well, the properties of the optical interface are important. The optical transition of an ideal emitter (Fig. 5.7(a)) has a naturally broadened line width γ related to its excited-state lifetime. In practice, noises in the surrounding environment of the emitter generally cause the optical line to broaden [47, 73].

The noises can be divided into spectral diffusion and dephasing by their time scales. Especially for solid-state emitters, the fluctuation of the local charge environment is often slower than the nanoseconds lifetime of the transition. These charge fluctuations can change the spacing of the energy levels involved in the optical transition by the Stark effect, causing the frequency to change. This effect is called spectral diffusion. Spectrally diffused transitions have a fluctuating resonance frequency, shot-to-shot, that can be modeled with a Gaussian distribution of standard deviation σ_ω . The fidelity of spectrally diffused spin-photon interfaces can be calculated by a Monte Carlo simulation, statistically averaging over the distribution function [47]. On the other hand, fast noise sources such as mobile charges on the surfaces of photonic nanostructures or acoustic

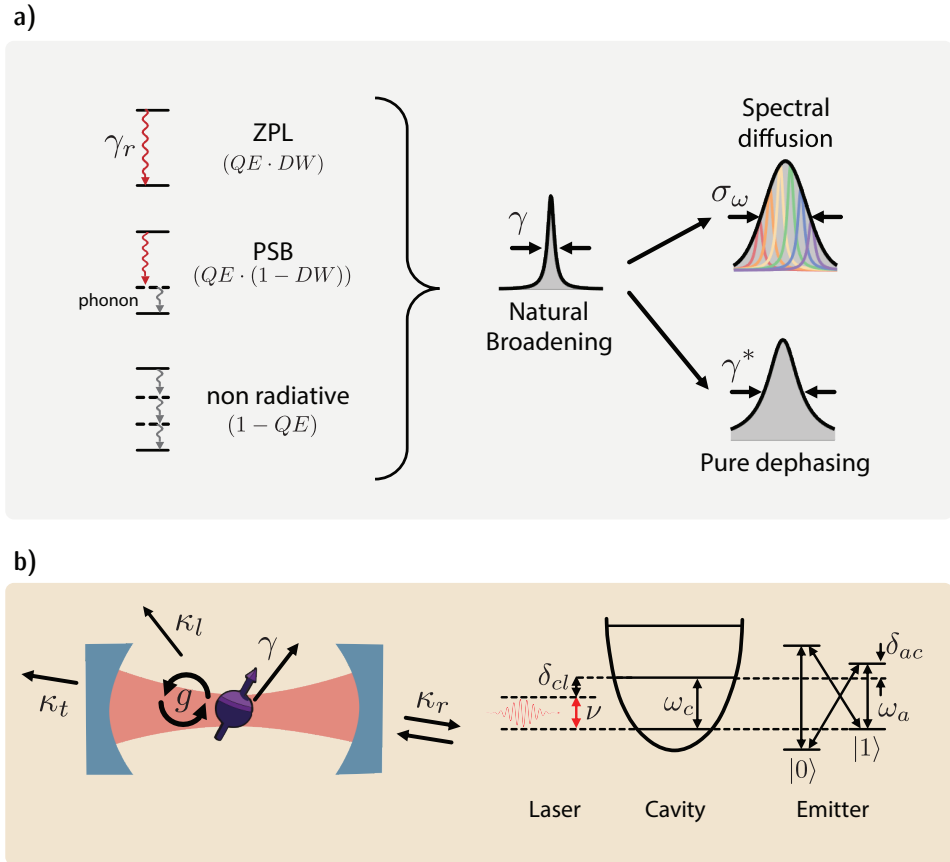


Figure 5.7: **The quantum modeling layer — spin-photon interface.** (a) The inefficiencies and noises of the optical transition in the spin-photon interface. Left: zero-phonon-line (ZPL) decay (γ_r), phonon-sideband (PSB) decay, and nonradiative decay combined give a total decay rate γ , resulting in the natural broadening (Lorentzian). The ratios of the transitions are expressed with an internal quantum efficiency (QE) and Debye-Waller factor (DW). Right: additional slow noise adds Gaussian spectral diffusion with a standard deviation of σ_ω , while the fast noise gives Lorentzian pure dephasing of line width γ^* . (b) Left: the cavity-QED system parameters. g is the vacuum Rabi frequency, γ is the spontaneous-emission rate, and κ_r, κ_t , and κ_l are the cavity decay rates to the reflection, transmission, and loss ports, respectively. Right: the level diagram of the laser, cavity, and spin. We assume that the $|1\rangle$ state of spins is desirably interacting with photons; interaction with the $|0\rangle$ state is negligible when $\gamma \ll \delta_{01}, g$.

phonon scattering induce homogeneous broadening of the transition. In this limit, the frequency and phase noises are indistinguishable: $S_{\delta\omega_1}(\omega) = S_{\delta\phi_1}(\omega) \cdot \omega^2$, where $S(\omega)$ is the power spectral density and the subscript of S refers to the random process. The noise is modeled as random phase flips or, equivalently, pure dephasing without longitudinal relaxation. For pure dephasing γ^* , the transition is further broadened by γ^* from radiative broadening and the line shape is Lorentzian. If the fluctuation time scale of a noise is in an intermediate regime, the dynamics of the spin-photon interfaces and the resulting fidelity of entanglement requires a complete specification of the noise as a stochastic random process.

Furthermore, especially in solid-state emitters, in addition to the coherent transition without the involvement of phonons — the zero-phonon line — there are phonon-assisted optical transitions, called phonon sidebands. Moreover, nonradiative, multi-phonon processes make the excited-state population decay without emitting photons. The quantum efficiency (QE) is defined as the ratio between the rates of all radiative processes to those of all processes:

$$QE = \frac{\Gamma_{\text{rad}}}{\Gamma_{\text{rad}} + \Gamma_{\text{nonrad}}}. \quad (5.3)$$

The decay rate of the zero-phonon line relative to the phonon sideband is the Debye-Waller factor (DW). In remote-entanglement settings, a large $QE \cdot DW$ is helpful for an efficient spin-photon interface, since only the coherent photons of the zero-phonon line are usable for entanglement protocols.

Other noise sources, such as a magnetic field or strain fluctuations, can also influence the transition through Zeeman shifts or mechanical deformation of the substrate, altering the energy levels. Moreover, in platforms other than solid-state emitters, such as trapped ions or superconducting qubits, other sources of noise, such as thermal fluctuations or coupling to nearby qubits, can play a significant role.

5.6.2. PHOTONIC CAVITY

A bare emitter can be used as a spin-photon interface, but it is advantageous to enhance the emitter properties and the collection efficiency of photons by means of an optical cavity. Other devices can be used to achieve the same goal, such as coupling the emitter to (photonic crystal) waveguides or optical fibers. However, the use of a cavity is the most common approach and, often, other devices can be described as a special case of cavity-emitter coupling [74, 75]. Quantum optical modeling of a two-level system coupled to an optical cavity is a well-studied subject [38]. See also Refs. [76, 77] for various cavity designs and the operations of cavities, including ring resonators [78].

Figure 5.7(b) shows relevant quantities of the emitter-cavity system. The dynamics of an emitter-cavity coupled system are governed by three parameters, γ , κ , and g . The emitter (cavity) transition line width γ (κ) is the inverse time of emitter decay (cavity relaxation). Photons spontaneously emitted into free space, nonradiative decays, and decays into phonon sidebands fall outside the coherent cavity-emitter interactions and

are considered as a relaxation channel of the system, incorporated in γ . The dynamics of a cavity-emitter coupled system are governed by the coupling rate g . Physically, g is the Rabi frequency when the emitter is driven by a vacuum cavity electric field (the zero-point electric field multiplied by the transition dipole moment).

The cooperativity of the system is defined as

$$C = \frac{4g^2}{\kappa\gamma}. \quad (5.4)$$

The cooperativity gauges the strength of coherent interaction relative to the dissipation and a higher cooperativity improves the efficiency of spin-photon interfaces. In REPs, this translates directly to the rate and the fidelities, as we will see in Sec. 5.8.

While κ , g , and γ are usually set parameters once the device is realized, the operation point of the cavity-emitter system can often be tuned. On the right-hand side of Fig. 5.7(b), we indicate the energy relations that determine the operation point. The frequencies ω_c, ω_a , and ν are related to the energies of the cavity mode, the atomic transition, and the external source (laser or single photon). The detuning between the cavity and emitter, δ_{ac} , determines how the emitter and cavity couple and what is the amplitude and phase response of the system. The external source frequency, which we define with respect to the cavity as δ_{cl} , can be optimized to obtain the desired phase or amplitude when interacting with the cavity. Realistically, there are often additional optical transitions that couple (or are close) to the cavity. Here, we depict a common level scheme for solid-state emitters, the Voigt configuration. When the energy difference between the target transition (here involving the bright state $|1\rangle$) and other transitions is comparable to the cavity line width, the emitter line width, or the coupling rate, or the input light is not far detuned, undesired interaction of the dark $|0\rangle$ state can lead to errors.

The cavity loss channels, $\kappa_{t,r,l}$, determine the cavity behavior. It is useful to relate the losses to the cavity input channel, which we take to be κ_r . In this way, we can define the cavity output coupling as critically coupled ($\kappa_l + \kappa_t = \kappa_r$), undercoupled ($\kappa_l + \kappa_t > \kappa_r$) or overcoupled ($\kappa_l + \kappa_t < \kappa_r$). The first and latter regimes are particularly interesting for a cavity-based spin-photon interface: an overcoupled cavity is sometimes called a single-sided cavity as the preferential output channel is the one used for probing the cavity; therefore emitted photons will be funneled in the collected optical mode, while an incident photon will almost always be reflected back to the same port; this cavity is used in the conditional-phase-reflection PBB. A critically coupled cavity allows both transmission and reflection to potentially be used as output channels. This is the cavity used for a conditional-amplitude-reflection PBB.

Emission-based spin-photon interfaces can be realized using a bare emitter, though this can pose a severe limitation to the entanglement-generation rate when quantum efficiencies and/or Debye-Waller factors are low. In addition, especially for spontaneous emission, spectral diffusion and dephasing directly affect the photon indistinguishabil-

ity and thus the entanglement fidelity. The efficiency and the fidelity of a spin-photon interface can be improved with a cavity: the Purcell effect enhances the emission of the optical transition by decreasing the lifetime and increasing the fraction of photons emitted by the target transition (e.g., the zero-phonon line for solid-state spins). At the same time, the optical-line-width broadening coming from the lifetime reduction decreases the relative effect of incoherent broadening mechanisms. The Purcell factor is defined as

$$F_p = 4g^2/\kappa\gamma_r = \frac{3}{4\pi^2} \frac{Q}{V} \left(\frac{\lambda}{n}\right)^3, \quad (5.5)$$

where Q is the cavity quality factor, λ is the resonant wavelength, n is the refractive index of the host material, and V is the effective mode volume. The effective mode volume is calculated with the electric field profile of the cavity mode, $E(\vec{r})$:

$$V = \int dV \epsilon(\vec{r}) |E(\vec{r})|^2 / \epsilon(\vec{r}_e) |E(\vec{r}_e)|^2, \quad (5.6)$$

for the emitter located at \vec{r}_e , where $\epsilon(\vec{r})$ is the permittivity as a function of the coordinates [38, 79]. If the cavity has a sufficiently high quality factor and a small mode volume, resulting in $g > \kappa, \gamma$, the system enters the strong-coupling regime [38], and the overall outcoupling efficiency of the emitted photons can become inefficient. This is because the cavity photon can be reabsorbed into the emitter before escaping the cavity. In the strong-coupling regime, the outcoupling efficiency is

$$\eta_{\text{out}} = \frac{\kappa_r}{\kappa} \cdot \frac{\kappa}{\kappa + \gamma}, \quad (5.7)$$

assuming that $\kappa_t = 0$ and where κ_r is the output port of the emitted photons. Equation (5.7) separates the contribution of cavity outcoupling and the fractional photon decay through the cavity. Thus, for example, reducing κ_r does not help the efficiency, as it decreases both factors. Furthermore, in the strong-coupling regime, the wave packet of photons oscillates with a coupling rate g , which makes the indistinguishability significantly susceptible to both g and $\kappa + \gamma$. When designing a cavity for entanglement, optimal parameters should be chosen within the trade-off space, rather than just strengthening the interaction, which often places the system in weak-coupling or bad-cavity regimes ($\kappa \gg g \gg \gamma$).

Spin-photon-gate and spin-photon-projector LBBs, by contrast, are based on the efficient coherent scattering of a single-photon or a weak coherent state by the emitter, which in turn requires strong interaction between the dipole of the emitter and a photonic mode. Spatial confinement of an optical mode by means of optical cavities or light-guiding structures (i.e., waveguides or optical fibers) enables this strong interaction. Here, we will focus on the use of cavities, as the scattering and emission of an emitter are similar [74, 75] except for the numerical calculation of the coupling (for multi-emitter cases, see Ref. [80]). In the strong-coupling regime, the response of the cavity to incoming photons with the cavity system is modulated in amplitude and phase by the state of the emitter. The cavity-emitter parameters and chosen operation points (in

terms of the cavity-emitter detuning and the photon frequency) can be used together with the system input-output formalism relations (see Sec. 5.10.c and Refs. [74, 75]) to determine the response of the system, in terms of reflection and transmission coefficients and loss. The spin-dependent reflection and transmission coefficients are complex valued and describe the amplitude and phase of the photon after the interaction. They are used to realize spin-photon gates and spin-photon projectors. In practice, this can be changing either the amplitude or the phase of the photonic state, conditioned on the spin being in the bright state, as shown in the last two rows of Fig. ??(a). When modulating phase, it is convenient to use a single-sided cavity, as almost all photons will be reflected optimizing the efficiency, while amplitude modulation benefits from a critically coupled cavity, maximizing the contrast of the field amplitudes. As anticipated, it is possible that the unwanted transition is spectrally close in frequency and it also couples to the cavity. In such cases, the relative phase or amplitude contrast between the system responses has to be optimized for high fidelity of the spin-photon emission. This can be done by changing the operation point, i.e. the emitter-cavity detuning and the input photon frequency.

5

5.6.3. QUANTUM CHANNEL DESCRIPTION OF PBB

The systematic and modular treatment of quantum channels is the key role of the PBB layer. Quantum channels can be additive and multiplicative; e.g., an optical π -pulse emission spin-photon interface and a weak excitation spin-photon interface, respectively. Table 5.1 lists the representative PBBs, which we use in Sec. 5.8 for benchmarking REPs. In the following sections, we explain the items of Table 5.1.

SPIN PBB

The state-preparation block outputs the desired state $|\psi\rangle$ with fidelity F_{state} . Our model assumes that a probabilistic error switches the state to an orthogonal state with probability $1 - F_{\text{state}}$. The density matrix of the system is an incoherent mixture of the two components weighted with the probabilities $\hat{\rho} = F_{\text{state}} |\psi\rangle\langle\psi| + (1 - F_{\text{state}}) |\psi^\perp\rangle\langle\psi^\perp|$.

Note that the quantum channel description of PBBs depends on the model of the physical systems. Let us assume that one rotates a perfectly prepared $|0\rangle$ state for the preparation of $\hat{R}_x(\theta)|0\rangle$, where $\hat{R}_x(\theta)$ is the single-qubit rotation around the x axis by θ . However, if θ has a bias error of ϵ , then $\rho_{\text{out}} = \hat{R}_x(\theta + \epsilon)|0\rangle\langle 0| \hat{R}_x^\dagger(\theta + \epsilon)$ will be more accurate. Choosing a realistic and accurate model is important. Our model-flexible description of PBBs enables the framework to cover all possible quantum hardware, as far as its quantum modeling can be made.

The most widely used error model for qubit operations (gates) is the depolarization channel. This channel maps the portion of the qubits population into a maximally mixed state, which is achieved with the uniformly probable application of Pauli operators (for n -qubit gates, the n -tensor product of Paulis and the identity operator, except for $I^{\otimes n}$).

Table 5.1: Physical building blocks as a quantum channel.

| QBB | Quantum Channel | Operator |
|---|--|--|
| | Spin PBB | |
| State Preparation | $\rho_{\text{out}} = F_{\text{state}} \psi\rangle\langle\psi + (1 - F_{\text{state}}) \psi^\perp\rangle\langle\psi^\perp $ | $\langle\psi \psi^\perp\rangle = 0$ |
| Qubit Error | $\hat{\rho}_{\text{out}} = F_1 \hat{\rho}_{\text{in}} + \frac{1-F_1}{3} (\hat{\sigma}_x \hat{\rho}_{\text{in}} \hat{\sigma}_x + \hat{\sigma}_y \hat{\rho}_{\text{in}} \hat{\sigma}_y + \hat{\sigma}_z \hat{\rho}_{\text{in}} \hat{\sigma}_z)$ | |
| Two-Qubit Error | $\hat{\rho}_{\text{out}} = F_2 \hat{\rho}_{\text{in}} + \frac{1-F_2}{15} \sum_{\hat{A}, \hat{B} = I, \hat{\sigma}_x, \hat{\sigma}_y, \hat{\sigma}_z} (\hat{A}^\dagger \otimes \hat{B}^\dagger) \hat{\rho}_{\text{in}} (\hat{A} \otimes \hat{B})$ | |
| | | $\langle \hat{A}, \hat{B} \rangle = I, \hat{\sigma}_x, \hat{\sigma}_y, \hat{\sigma}_z$ $\langle \hat{A}, \hat{B} \rangle \neq I \otimes I$ |
| | Photonic PBB | |
| Photonic Loss | $\rho_{\text{out}} = \text{tr}_L [\hat{U}(\rho_{\text{in}} \otimes 0_L\rangle\langle 0_L) \hat{U}^\dagger]$ | $\hat{U} = \exp[\theta_L(\hat{a}_L^\dagger - \hat{a}_L)]$ ¹ |
| Mode Mixing | $\rho_{\text{out}} = \hat{U} \rho_{\text{in}} \hat{U}^\dagger$ | $\hat{U} = \exp[\pi/4(\hat{a}\hat{b}^\dagger - \hat{a}^\dagger\hat{b})]$ |
| Photodetection | $\rho_{\text{out}} = \hat{\Pi} \rho_{\text{in}} \hat{\Pi}^\dagger$ | $\hat{\Pi} = \hat{I} - 0_p\rangle\langle 0_p (1_p\rangle\langle 1_p)$ |
| Entangled Pair Source (SPDC) | $\rho_{\text{out}} = \hat{S}_2(\zeta) 0000\rangle\langle 0000 \hat{S}_2^\dagger(\zeta)$ | $\hat{S}_2(\zeta) = \exp[\zeta(\hat{a}_H^\dagger \hat{b}_V^\dagger + \hat{a}_V^\dagger \hat{b}_H^\dagger) + \text{h.c.}]$ |
| | Spin-photon PBB | |
| Spontaneous Emission (optical π -pulse) | $\rho_{\text{out}} = C \rho_{\text{in}} C^\dagger + p_{\text{incoh}} \hat{C}_{\text{incoh}} \rho_{\text{in}} \hat{C}_{\text{incoh}}^\dagger + p_{\text{2ph}} \hat{C}_{\text{2ph}} \rho_{\text{in}} \hat{C}_{\text{2ph}}^\dagger$ | $\hat{C} = \sqrt{p_{\text{coh}}} \hat{C}_{\text{coh}} + \sqrt{p_{\text{loss}}} \hat{C}_{\text{loss}}$ $\hat{C}_{\text{coh}} = 0_s\rangle\langle 0_s \otimes \hat{I} + 1_s\rangle\langle 1_s \otimes \hat{a}^\dagger$ $\hat{C}_{\text{loss}} = 1_s\rangle\langle 1_s \otimes \hat{a}_{\text{loss}}^\dagger$ $\hat{C}_{\text{incoh}} = 1_s\rangle\langle 1_s \otimes \hat{a}_{\text{incoh}}^\dagger$ $\hat{C}_{\text{2ph}} = 1_s\rangle\langle 1_s \otimes \frac{1}{\sqrt{2}} \hat{a}^\dagger \hat{a}^\dagger$ |
| Coherent Scattering | $\rho_{\text{out}} = \sum_k P_\beta(k) \hat{C}_{\text{incoh}}(k) (\hat{C}_{\rho_{\text{in}}} \hat{C}^\dagger)_{\text{incoh}}^\dagger(k)^2$ | $\hat{C} = 0_s\rangle\langle 0_s \otimes \hat{I} + 1_s\rangle\langle 1_s \otimes \hat{D}_d(\alpha) \otimes \hat{D}_{a_{\text{loss}}}(\alpha_L)$ $\hat{C}_{\text{incoh}}(k) = 0_s\rangle\langle 0_s \otimes \hat{I} + 1_s\rangle\langle 1_s \otimes \frac{1}{\sqrt{k_i}} (\hat{a}_{\text{incoh}}^\dagger)^k$ |
| Conditional Phase Reflection | $\rho_{\text{out}} = \text{tr}_L (\hat{C}_z \rho_{\text{in}} \hat{C}_z^\dagger)$ | $\hat{C}_z = \sum_{k_s=0,1} k_s\rangle\langle k_s \otimes \exp\left(i(\angle r_k \hat{a}^\dagger + \angle l_k \hat{a}_{\text{loss}}^\dagger \hat{a}_{\text{loss}})\right) \exp\left[\theta_k (\hat{a}^\dagger \hat{a}_{\text{loss}} - \hat{a} \hat{a}_{\text{loss}}^\dagger)\right]$ ³ |

² $P_\beta(k) = \frac{|\beta|^{2k} \exp^{-|\beta|^2}}{k!}$. Note that this assumes perfect incoherent photon filtering afterward. For the case of imperfect filtering, two incoherent modes for collection and loss should be counted separately (then, filtering modifies the collection incoherent mode only).

³ $\theta_k = \arcsin(\sqrt{L_k})$, r_k (l_k) are the complex coefficient of reflection (loss) of a photon for spin state $|k_s\rangle$. " $\angle(\cdot)$ " is the phase of the following complex coefficient.

Table 5.1 lists the one- and two-qubit gate errors as they are often used,

$$\hat{\rho}_{\text{out}} = F_1 \hat{\rho}_{\text{in}} + \frac{1 - F_1}{3} (\hat{\sigma}_x^\dagger \hat{\rho}_{\text{in}} \hat{\sigma}_x + \hat{\sigma}_y^\dagger \hat{\rho}_{\text{in}} \hat{\sigma}_y + \hat{\sigma}_z^\dagger \hat{\rho}_{\text{in}} \hat{\sigma}_z) \quad (5.8)$$

$$\hat{\rho}_{\text{out}} = F_2 \hat{\rho}_{\text{in}} + \frac{1 - F_2}{15} \sum_{\substack{\hat{A}, \hat{B} = \hat{I}, \hat{\sigma}_x, \hat{\sigma}_y, \hat{\sigma}_z \\ \hat{A} \otimes \hat{B} \neq \hat{I} \otimes \hat{I}}} (\hat{A}^\dagger \otimes \hat{B}^\dagger) \hat{\rho}_{\text{in}} (\hat{A} \otimes \hat{B}). \quad (5.9)$$

In the simulation of color centers in Sec. 5.8, we assume that spin PBBs are perfect because these operations have errors that are an order of magnitude smaller than those of photonic or spin-photon PBBs.

PHOTONIC PBB

A photon lost while traveling through the fiber by absorption or scattering can project the spin-photon entangled state to a trivial state. A popular way to describe the process is via the Lindblad master equations [81]. This is equivalent to unitary evolution with an auxiliary mode and partial tracing (see the Table 5.1 element). The unitary evolution is equivalent to the beam-splitter operation, the angle of which is determined from the loss ($\theta_L = \arcsin \sqrt{L}$; see Sec. 5.10.c). The same unitary evolution also describes the mode mixing for erasing “which path information”. Here, we have listed the perfect mode mixing with $\theta = \pi/4$ but imperfect mode mixing can be set with different values of θ for the biased case or even combinations of θ values for stochastic description.

We can implement the photodetection on a specific mode (p subscription in Table 5.1) with a projection operator. Here, we have used the projection of a Fock-state encoded photonic mode but one can use the eigenstate of a different basis for the projection operator.

Lastly, we present the PBB for entangled photon-pair sources. Among many implementations and photon encodings, we specifically consider spontaneous parametric down-conversion (SPDC), the polarization-encoded photon-pair state [82, 83],

$$\rho_{\text{out}} = |\text{SPDC}\rangle \langle \text{SPDC}|, \quad (5.10)$$

$$|\text{SPDC}\rangle = \hat{S}_2(\zeta) |0000\rangle = e^{-|\zeta|^2/2} \cdot \left[|0000\rangle + \zeta (|1_{a,H} 0_{a,V} 0_{b,H} 1_{b,V}\rangle + |0_{a,H} 1_{a,V} 1_{b,H} 0_{b,V}\rangle) + \dots \right], \quad (5.11)$$

where $\hat{S}_2(\zeta) = \exp[\zeta(\hat{a}_H^\dagger \hat{b}_V^\dagger + \hat{a}_V^\dagger \hat{b}_H^\dagger) + \text{h.c.}]$ is the SPDC operator, ζ denotes the numerical parameter determined by pump field, \hat{a} and \hat{b} are two spatial photonic modes, H and V indicate two polarization modes, and “h.c.” refers to Hermitian-conjugate terms. It is worth noting that $|HV\rangle + |VH\rangle = |1_{a,H} 0_{a,V} 0_{b,H} 1_{b,V}\rangle + |0_{a,H} 1_{a,V} 1_{b,H} 0_{b,V}\rangle$ in the literature for simplicity, whereas we explicitly specify photon numbers in each photonic mode to align with other PBBs.

SPIN-PHOTON PBB

The ideal operation of the emission spin-photon interface using an optical π pulse is described with the coherent channel subscripted with “coh”. When the spin is in

the dark state ($|0\rangle$), it does not affect the state of the photonic mode (\hat{I}). When the spin is in the bright state ($|1\rangle$), the desired outcome is the creation of a single photon in the mode of interest, \hat{a} . This results in the Kraus operator $\hat{C}_{\text{coh}} = |0_s\rangle\langle 0_s| \otimes \hat{I} + |1_s\rangle\langle 1_s| \otimes \hat{a}^\dagger$.

In realistic devices, ideal events only happen with probability p_{coh} . With probability, p_{incoh} , the incoherent channel, labeled by “incoh”, adds a photon with a random phase that does not coherently interfere, which reflects the non-unity indistinguishability. This can be modeled with the addition of photon to the incoherent mode \hat{a}_{incoh} that will not be interfered with by the mode-mixing PBB. Likewise, double excitation and finite efficiencies contribute additively to the density matrix through $\hat{C}_{2\text{ph}}$ and \hat{C}_{loss} , with $p_{2\text{ph}}$ and p_{loss} (see Table 5.1 and Sec. 5.10.d). Again, these PBBs can add more channels such as ionization or remove some if they are not wanted.

All the parameters including probabilities are calculated at the quantum optical modeling layer, and PBBs require these numerical values for the calculation of ρ_{out} . For the calculation of PBB parameters from physically characterized ones, see Sec. 5.10.d.

Instead of a short strong optical pulse, one can weakly drive the transition by coherently scattering the field. Scattered in this way, the field is in a coherent state with amplitude α . The process can be encapsulated by the displacement operator $\hat{D}_{\hat{a}}(\alpha)$ where \hat{a} represents the mode that the operator acts on ($\hat{D}(\alpha)|0\rangle = |\alpha\rangle$). At the same time, the excitation field is also scattered to unwanted mode \hat{a}_{loss} . Moreover, incoherent scattering due to noise adds photons to another mode with Poisson statistics. We can express the loss-mode part of the density matrix as

$$\hat{\rho}_{\text{loss}} = \sum_i \frac{n_{\text{loss}}^i \exp\{-n_{\text{loss}}\}}{i!} |i\rangle\langle i|, \quad (5.12)$$

where n_{loss} is the average number of photons added to the loss mode. $|n \neq 0\rangle$ components of the density matrix reduce the fidelity of the fidelity of spin-photon entanglement and subsequent spin-spin entanglement, because they leak information on the quantum state (only the bright state, $|1_s\rangle$, adds the photon to the loss mode).

5.7. SOFTWARE IMPLEMENTATION OF THE FRAMEWORK

The layered and modular framework lends itself well to implementation in simulation code. Our QuREBB (Quantum Remote-Entanglement Building Blocks) simulation repository is available on GitHub [24] and we have used it to simulate and compare different REPs (Sec. 5.8). One can reuse implemented codes with minimal corrections due to our modular framework, even for different protocol topologies (with modifications of LBBs) or different physical systems (with modifications of quantum modeling).

The code is based on the QuTiP package [84], written in (python). For the simulation of REPs, it is important to represent composite quantum systems (involving stationary qubits and multiple photonic modes), track all modes, and trace out photonic loss modes when needed. QuTiP references subsystems by indices and partial traces modify

the indices. We have improved the indexing capabilities of the quantum object (Qobj) in QuTiP and we refer to a quantum mode with a string such that each subsystem can be properly named (a dictionary). We have created an inherited class, “named quantum object” (NQobj), that is compatible with the QuTiP standard functions and we have described the names of the subsystems in an attribute “names”. With this new attribute in place, one can allow for operations with NQobjs of different sizes. For example, when a density matrix evolves with a unitary, one can omit the identities for the subsystems that are not involved, as this is inferred from the names of the objects. For a modular use of the code, this is an essential feature, as it allows us to write code for the building blocks without knowledge of the whole system. Moreover, it allows us to trace out loss modes anywhere in the calculations, as they can be indexed by name, without the risk of shifting all the indices of the other modes by removing the loss mode.

The state of the system is represented by a non-normalized density matrix. In this way, both the state and the success probability are represented by one object. The state is the normalized density matrix and the success probability is the trace of the density matrix. These non-normalized density matrices act as the interface between the PBBs, which are the quantum operators on the density matrix.

5

The quantum modeling of the spin-photon interface favors the description with creation and annihilation operators (the Heisenberg picture), while the nonunitary evolution of quantum systems favors density matrices (the Schrödinger picture). To bridge the gap, one needs descriptions such as one of the beam splitters in Table 5.1: $\hat{U} = \exp[\theta(\hat{a}\hat{b}^\dagger - \hat{a}^\dagger\hat{b})]$. We have modeled the cavities as a composite system of beam splitters and phase shifters (see Sec. 5.10.c). The method is advantageous in directly describing arbitrary big Fock-state space in QuTiP as users can choose the size of the creation and annihilation operators accordingly. The code is directly extendable to the simulation of weak coherent states with non-negligible multiphoton states.

While our package covers the low-level description of quantum systems to the protocol-level description of elementary entanglement links, it complements other tools at the link layer or above. This includes NetSquid [85], an event-driven network simulator that can cover a link layer [86] or a higher level with a large number of nodes [2], as well as QuNetSim [87] and others [88, 89].

5.8. SIMULATING AND BENCHMARKING ENTANGLEMENT PROTOCOLS

In this section, we show an example of how the proposed framework can be used to break down three different entanglement protocols into realistic PBBs, and we use the software introduced in Sec. 5.7 to simulate the performance and compare them. We set the physical platform used for all the protocols to be the silicon-vacancy (SiV) center in a diamond coupled to an optical cavity.

We outline our simulation comparison in Fig. 5.8. The hardware platform that we have chosen is the SiV color center in diamond, and we consider photonic crystal cavities

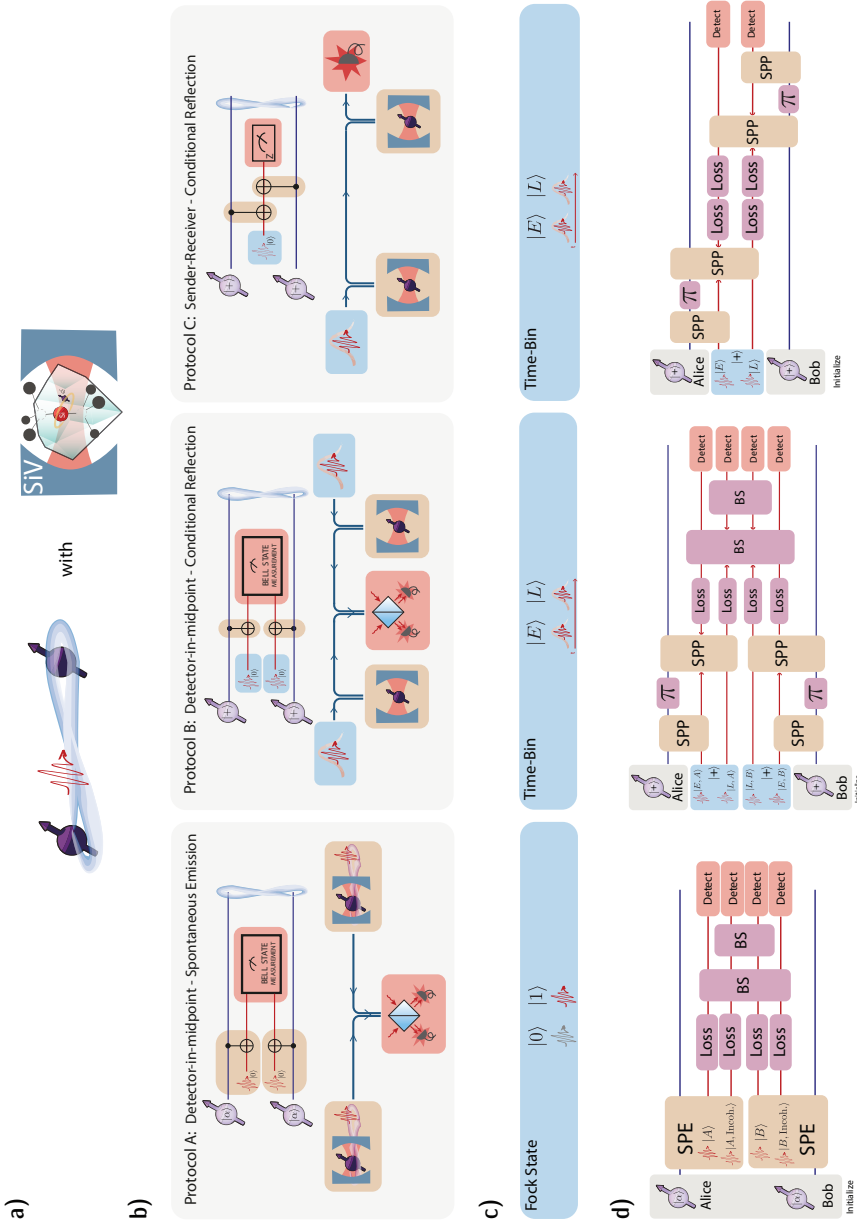


Figure 5.8: **A comparison of different protocols for entanglement generation** using the SIV center in diamond coupled to an optical cavity as a spin-photon interface. (b) The circuit diagram and LBB descriptions of the protocols under investigation. (c) The photonic encodings for each protocol. (d) The protocol after the LBBs are compiled to hardware-aware PBBs and including imperfections such as loss. The photon states are labeled by node of interaction (A and B for Alice and Bob), by time-bin encoding (E and L for the early and late modes), and whether the photon is resulting from incoherent emission (Incoh.). The initial photon state is defined as $|+\rangle = 1/\sqrt{2}(|E\rangle + |L\rangle)$.

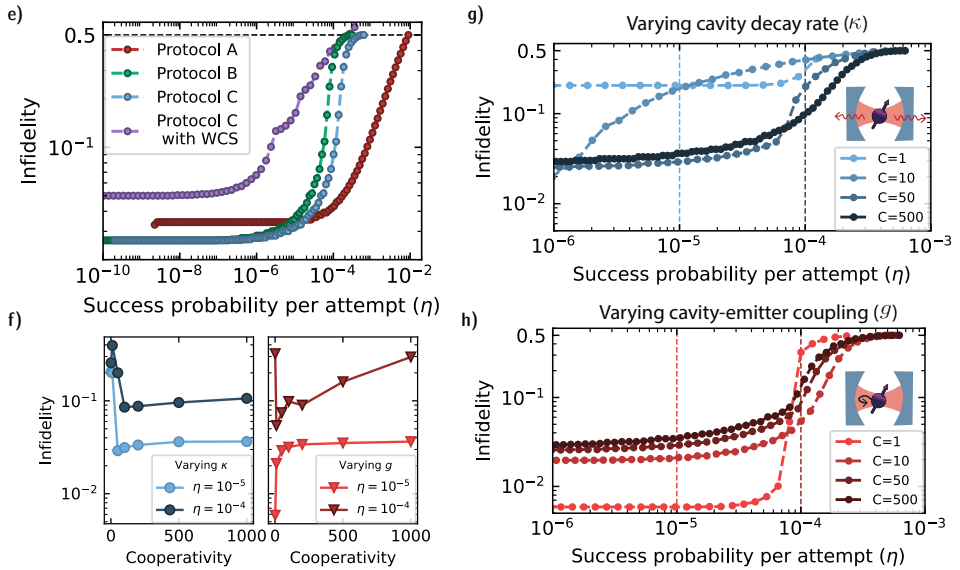


Figure 5.9: **Comparison of different protocols for entanglement generation - Simulations.** (e) Simulated success probability-infidelity curves for the different protocols using the parameters of Table 5.3. Protocol C is also simulated for a weak-coherent-state (WCS) input instead of single photons. (f)-(h) The performance of protocol C when the cooperativity is changed by improving either the cavity decay rate κ or the emitter-cavity coupling g , following Eq. (5.4). (f) The fidelity for two different success probabilities η when varying κ or g (left and right graphs, respectively) (g), (h) The success-probability-infidelity curves for some of the cooperativities. The dashed lines mark the values of η shown in (f).

to either enhance the spin-photon emission or to realize spin-photon projectors in the strong-coupling regime. The protocols that we compare are one emission-based protocol with detection-in-midpoint topology, where we use Fock-state encoding for the photon (protocol A in Fig. 5.8(b)) and two projector-based (protocols B and C) with the conditional-amplitude-reflection and the time-bin encoding, with a sender-receiver and detection-in-midpoint topology. The detailed implementation in terms of PBBs is shown for all protocols in Figs. 5.8(c) and 5.8(d). More details on the quantum optical modeling used can be found in Sections 5.10.c and 5.10.d.

We compare the performance of the protocols according to the simulation results. For each simulation, we start with realistic experimental values for the particular system that can be found in the literature (see Table 5.3) and we search for the optimal operation point of the spin-photon interface by sweeping a subset of the parameters (“sweep parameters”, indicated as *variable* in Table 5.3) and for each configuration we calculate the protocol outcome. We choose to optimize only parameters that are easily controllable in an experimental setting: the detuning between the cavity and the emitter and the detuning between the input photon and the cavity (which we call the operation frequency). The frequency difference between the two optical transitions involved, δ_{01} , can in principle be tuned by applying an external magnetic field and this can have a big impact on the performance of the protocol. However, as the magnetic field is intertwined with other features of the system, such as the cyclicity of the optical transition and the qubit frequency, we do not consider it here as a sweep parameter. Similarly, intrinsic properties of the cavity or the emitter are considered to be fixed parameters for the protocol optimization. Ultimately, the simulation gives us the infidelity and success probability with which the protocol achieves a definite target state, which is one of the four Bell states, as a function of the swept parameters. To benchmark the protocols we compare the trade-off between the infidelity and the success probability. We report the success probability of the protocol for each attempt, as obtained from the density matrix of the final state. The effective rate can be extracted from the success probability by accounting for the repetition rate of the protocol: this can give a more consistent comparison. Figure 5.9(e) shows the rate-infidelity curves for the three protocols with the starting values reported in Table 5.3. From these curves, one can see how, with these parameters and protocol implementations, protocol A is advantageous with respect to the others, except at low rates where the fidelity is limited by the incoherent emission due to dephasing. Here, protocols B and C allow us to obtain lower infidelity. We also simulate protocol C using a weak-coherent-state (WCS) input to approximate single photons. In this case, the success probability drops faster than in the single-photon implementation, as it scales with the average photon number in the WCS, and the infidelity is higher since the multiphoton components in the input cause protocol errors.

Finally, we simulate how protocol C performs for different values of the cooperativity. Again, we optimize for each point by sweeping the “sweep parameters” as above and, in addition to that, we vary only one of the intrinsic cavity parameters to change the cooperativity. The rate-infidelity curves are reported in Fig. 5.9(g) and (h). We test two ways

to change the cooperativity, as can be seen from Eq. (5.4). In Fig. 5.9(g) we do this by varying the cavity decay rate κ , which is related to the cavity quality factor Q , at fixed cavity-emitter coupling g . In Fig. 5.9(h), we keep κ fixed and we vary the cavity-emitter coupling g , which can be realized in practice by changing the cavity-mode volume, the overlap between the emitter dipole and the field distribution, or the quantum efficiency and Debye-Waller factor of the optical system. In Fig. 5.9(f), we report the infidelity at two different success probabilities. Interestingly, increasing the cooperativity by only optimizing a subset of the parameters does not always lead to better performance. This can be attributed to the Purcell broadening of the optical line width which, when a second optical transition is close in frequency (δ_{01} is small compared to the Purcell-broadened line width and cannot be optimized), can cause a decrease in fidelity due to undesired interaction with the wrong spin state. Varying the cavity line width (κ) or varying the coupling g can affect this phenomenon differently, especially at low cooperativities. Furthermore, when increasing the cooperativity in Fig. 5.9 by only changing either κ or g , we pass from the bad-cavity regime ($\kappa \gg g$) to the strong-coupling one ($g \gg \kappa$). As discussed in Sec. 5.6.2, this regime is not necessarily optimal for entanglement generation, especially if the system is not optimized accordingly.

5.9. CONCLUSIONS

In this work, we have introduced a modular framework to describe photon-mediated remote-entanglement protocols. Our framework divides the remote-entanglement protocols into four different layers, allowing a perspective of the entanglement protocol from an abstract and hardware-agnostic overview to a detailed description of each component and physical implementation. We have described the function of the different layers and provided examples of their realization, including detailed modeling of cavity-based spin-photon interfaces. Finally, using a software implementation that directly reflects the modular approach of the framework, we have simulated different remote-entanglement-protocol topologies based on a realistic experimental platform and investigated how they perform under different parameter regimes.

For future work, our framework can be expanded into both higher-level uses and lower-level descriptions. At the higher level, leveraging the logical operations of the LBB layer can construct error-corrected encoded quantum networks [23]. The incorporation of error-correction schemes into our framework would enable the simulation of fault-tolerant quantum applications. On the other hand, the integration of material-level details of physics (for the case of color centers see, e.g., Ref. [90]), into our quantum optical modeling can help the choice of quantum systems to optimally configure the network. This inclusion of finer-grained aspects will enhance the accuracy of our simulations as well. In addition, we believe that our framework can be extended to apply to continuous-variable entanglement distribution [91] and qudit entanglement distribution [92].

5.10. METHODS

5.10.A. NOMENCLATURE

Table 5.2: Nomenclature used in this tutorial

| | |
|---------------------------------|----------------------------------|
| Topology | |
| Detection-in-midpoint | |
| Sender-receiver | |
| Source-in-midpoint | |
| Logical Building Blocks | |
| Spin | Initialization |
| | Gate |
| | Measurement |
| Photon | Photon source |
| | Photon pair source |
| | Measurement |
| | Bell state measurement |
| | Photon gate |
| Spin-Photon | Spin-photon emission |
| | Spin-photon gate |
| | Spin-photon projector |
| | Spin-photon absorption |
| Encoding | |
| Fock state | |
| Time-bin | |
| Polarization | |
| Dual-rail | |
| Frequency | |
| Physical Building Blocks | |
| Spin | Initialization |
| | Gate |
| | Measurement |
| Photon | Initialization |
| | Measurement |
| | Mode mixing |
| | Z-Rotation |
| | X-Rotation |
| Spin-photon | Spontaneous emission |
| | Coherent scattering |
| | Raman scattering |
| | Conditional amplitude reflection |
| | Conditional phase reflection |

5.10.B. NOTATION AND SIMULATION PARAMETERS

Table 5.3: SIV parameters for simulations

| Name | Symbol | Spin-Photon Projector | Spin-Photon Emission |
|------------------------------------|-------------------------------|-----------------------|--|
| Emitter Resonance Frequency | ω_a | | 406.706 THz |
| Cavity Resonance Frequency | ω_c | | Variable |
| Laser Frequency | ν | | Variable |
| Laser-Cavity Detuning | Δ_{lc} | | Variable |
| Cavity-Emitter Detuning | Δ_{ce} | | Variable |
| Laser-Emitter Detuning | Δ_{le} | | Variable |
| Emitter Radiative Decay Rate (ZPL) | γ_r | | 13.1 MHz ^a |
| Emitter Total Decay Rate | γ | 92.5 MHz ^a | 100 MHz |
| Pure Dephasing Spectral Diffusion | γ^* σ_ω | | 30.5 MHz ^{b,c} N/A ^d |
| Total Emitter Linewidth | Γ | 123 MHz ^b | N/A |
| Optical Transitions Detuning | δ_{01} | | 1 GHz |
| Emitter-Cavity Coupling | g | 8.38 GHz ^b | 6.81 GHz |
| Cavity Decay Rate | κ | 21.8 GHz ^b | $\kappa_l + \kappa_t = 89$ GHz, $\kappa_r = 240$ GHz ^e |
| Cavity Quality Factor | Q | 18,700 ^b | 1,237 |
| Cavity Cooperativity | C | 105 | 4.3 ^f |
| Debye-Waller Factor | DW | | 0.7 ^g |
| Quantum Efficiency | QE | | 0.2 |
| Link Loss | - | | 0.9 |
| Device Insertion Loss | - | | 0.5 |

^a [90]^b [35]^c This data for over-coupled cavity does not exist. We assume that it is the same as the critically-coupled case.^d To the best of our knowledge, there are no spectroscopic results resolving pure dephasing and spectral diffusion of SIV. In this work, we simply assume that the broadening in [35] is from the pure dephasing considering the Lorentzian lineshape.^e [93]^f Note that this number is converted with pure dephasing assumed.^g [94]

5.10.C. MODELING CONDITIONAL REFLECTION SPIN-PHOTON INTERFACE WITH UNITARIES

We model the conditional reflection spin-photon interfaces using input-output formalism [74, 75]. This describes the response of the system in terms of r , t , and l as the complex coefficients of reflection, transmission, and loss, respectively. To calculate the unitary operator in the Fock state basis, we use the beamsplitter configuration in Fig. 5.10 and the description of a beamsplitter

$$U = \exp\left\{\left[\theta(a^\dagger b - ab^\dagger)\right]\right\} \quad (5.13)$$

$L = |l|^2$ is the loss. For example, if 30% of photons are lost, then $L = 0.3$.

$$U_1 = \exp\left\{\left[\theta_1(a^\dagger l - al^\dagger)\right]\right\}. \quad (5.14)$$

$$\theta_1 = \arctan\left(\frac{\sqrt{L}}{\sqrt{1-L}}\right). \quad (5.15)$$

Then, from r and t , we calculate the normalized r' and t' ;

$$r' = r / \sqrt{|r|^2 + |t|^2} \quad (5.16)$$

$$t' = t / \sqrt{|r|^2 + |t|^2}. \quad (5.17)$$

The unitary for the splitting is

$$U_2 = \exp\left\{\left[\theta_2(a^\dagger b - ab^\dagger)\right]\right\} \quad (5.18)$$

$$\theta_2 = \arctan\left(\frac{|t'|}{|r'|}\right) \quad (5.19)$$

For adjusting the phases,

$$U_3 = \exp\left[i(\angle r a^\dagger a + \angle t b^\dagger b)\right] \quad (5.20)$$

The total unitary for loss-reflection-transmission is,

$$U = U_3 \cdot U_2 \cdot U_1. \quad (5.21)$$

One can use both ports of the cavity with dual rail encoding. The interference of fields is reflected in the interference of the reflection/transmission coefficient derived from the coherence of the spins. Figure 5.10 shows the two-port-to-three-port unitary decomposition. The splitting ratio of BS1 is determined by the loss of input port 1, while that of BS2 is by the loss of input port 2. BS3 combines the output ports of BS1 and BS2 to generate reflection and transmission. A total of five phase shifters are added between the beamsplitters and at the output port for the phase adjustment.

For a larger number of input/output ports, we can use Reck [95] or Clements [96] decomposition.

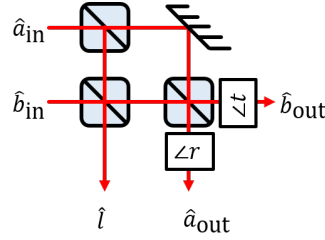


Figure 5.10: Two-port-to-three-port unitary construction with beamsplitters.

5.10.D. QUANTUM MODELED PHYSICAL PARAMETERS

Here, we discuss the PBB parameters calculated from the quantum modeling layer.

SPONTANEOUS-EMISSION PBB

$$p_{\text{coh}} = \langle 1 | \rho_{\text{in}} | 1 \rangle \cdot \frac{\kappa_r}{\kappa} \cdot \frac{C}{C+1} \cdot \frac{F_p \gamma_r}{\Gamma + F_p \gamma_r} + \langle 0 | \rho_{\text{in}} | 0 \rangle \quad (5.22)$$

$$p_{\text{incoh}} = \langle 1 | \rho_{\text{in}} | 1 \rangle \cdot \frac{\kappa_r}{\kappa} \cdot \frac{C}{C+1} \cdot \frac{\gamma^* + \sigma_\omega}{\Gamma + F_p \gamma_r} \quad (5.23)$$

$$p_{2\text{ph}} = 0 \quad (5.24)$$

$$p_{\text{loss}} = 1 - p_{\text{coh}} - p_{\text{incoh}} - p_{2\text{ph}} \quad (5.25)$$

$$(5.26)$$

The double-excitation probability $p_{2\text{ph}}$ is a function of the lifetime, pulse width, and ionization probability. Here, we neglect the two-photon emission for simplicity. This is made possible by adjusting the pulse area so that one transition is an odd-multiple π pulse and the other is an even-multiple π pulse.

COHERENT-SCATTERING PBB

$$\alpha_{\text{tot}} = \alpha + \alpha_L \quad (5.27)$$

$$\alpha_{\text{tot}} = \eta \alpha \quad (5.28)$$

$$\alpha_L = \frac{1 - \eta}{\eta} \alpha \quad (5.29)$$

$$\eta = \frac{\kappa_r}{\kappa} \cdot \frac{F_p}{F_p + 1} \quad (5.30)$$

$$|\beta|^2 = \left[\frac{\gamma^*}{\Gamma' - \gamma^*} + \frac{1 - QE' \cdot DW'}{QE' \cdot DW'} \right] |\alpha_{\text{tot}}|^2 \quad (5.31)$$

$$\Gamma' = \Gamma + F_p \gamma_r \quad (5.32)$$

$$DW' = \frac{(F_p + 1)DW}{F_p \cdot DW + 1} \quad (5.33)$$

$$QE' = \frac{QE \cdot (F_p \cdot DW + 1)}{1 + F_p \cdot QE \cdot DW} \quad (5.34)$$

where η is the collection efficiency of the coherent emission. The prime represents the cavity-modified rate or the ratio of transitions. In Eq. (5.31), the first term is for incoherent emission and the second term is for inefficiencies.

5.10.E. SIMULATIONS PARAMETER SWEEP AND DETAILS

To optimize the fidelity and success probability of the simulations in Fig. 5.8 we perform the parameter sweep in Table 5.4.

| Protocol | Parameters | Range | Number of points |
|----------|-------------------------------|------------------|------------------|
| A | α (initial spin state) | $[10^{-7}, 0.3]$ | 500 |
| B,C | Δ_{la} | $[-18, 0]$ GHz | 1000 |
| | Δ_{ac} | $[0, 120]$ GHz | 60 |
| C (WCS) | α (WCS) | $[0.001, 2]$ | 10 |
| | Δ_{la} | $[-15, -2]$ GHz | 1200 |
| | Δ_{ac} | $[0, 120]$ GHz | 50 |

Table 5.4: Sweep parameters for simulations of Fig. 5.8

For the cooperativity sweep, by varying κ we use the same values as in the table. For the sweep by varying g , the cavity-emitter spectrum changes significantly; therefore, the range has to be optimized for each simulation. The ranges can be found in the simulation notebooks [24].

The simulations were run on a desktop computer (Intel Xenon CPU, 3.50 GHz, quad core, eight threads, 32-GB RAM). The simulation of a single protocol run takes approximately 350 ms for protocols A and C and approximately 550 ms for protocol B (mostly dependent on the size of the Hilbert space). By using basic PYTHON multiprocessing functions, we can speed up the parameter sweep by a factor ~ 5 compared to just looping the protocol over the whole parameter space. This results on a runtime of ~ 2 min for Protocol A, ~ 2 hours for Protocol B, ~ 1 hour for protocol C and ~ 10 hours for the WCS simulation.

BIBLIOGRAPHY

- [1] H. J. Kimble, *The quantum internet*, Nature **453**, 1023 (2008).
- [2] S. Wehner, D. Elkouss and R. Hanson, *Quantum internet: A vision for the road ahead*, Science **362**, eaam9288 (2018).
- [3] M. Ruf, N. H. Wan, H. Choi, D. Englund and R. Hanson, *Quantum networks based on color centers in diamond*, Journal of Applied Physics **130**, 070901 (2021).
- [4] C. Cabrillo, J. I. Cirac, P. García-Fernández and P. Zoller, *Creation of entangled states of distant atoms by interference*, Physical Review A **59**, 1025 (1999).
- [5] L.-M. Duan, M. D. Lukin, J. I. Cirac and P. Zoller, *Long-distance quantum communication with atomic ensembles and linear optics*, Nature **414**, 413 (2001).

- [6] D. E. Browne, M. B. Plenio and S. F. Huelga, *Robust Creation of Entanglement between Ions in Spatially Separate Cavities*, Physical Review Letters **91**, 067901 (2003).
- [7] L.-M. Duan and H. J. Kimble, *Efficient Engineering of Multiatom Entanglement through Single-Photon Detections*, Physical Review Letters **90**, 253601 (2003).
- [8] C. Simon and W. T. M. Irvine, *Robust Long-Distance Entanglement and a Loophole-Free Bell Test with Ions and Photons*, Physical Review Letters **91**, 110405 (2003).
- [9] S. D. Barrett and P. Kok, *Efficient high-fidelity quantum computation using matter qubits and linear optics*, Physical Review A **71**, 060310 (2005).
- [10] N. Sangouard *et al.*, *Long-distance entanglement distribution with single-photon sources*, Physical Review A **76**, 050301 (2007).
- [11] M. Pompili *et al.*, *Realization of a multinode quantum network of remote solid-state qubits*, Science **372**, 259 (2021).
- [12] S. L. N. Hermans *et al.*, *Qubit teleportation between non-neighbouring nodes in a quantum network*, Nature **605**, 663 (2022).
- [13] N. H. Nickerson, J. F. Fitzsimons and S. C. Benjamin, *Freely Scalable Quantum Technologies Using Cells of 5-to-50 Qubits with Very Lossy and Noisy Photonic Links*, Physical Review X **4**, 041041 (2014).
- [14] W. J. Munro, K. Azuma, K. Tamaki and K. Nemoto, *Inside Quantum Repeaters*, IEEE Journal of Selected Topics in Quantum Electronics **21**, 78 (2015).
- [15] E. T. Khabiboulline, J. Borregaard, K. De Greve and M. D. Lukin, *Optical Interferometry with Quantum Networks*, Physical Review Letters **123**, 070504 (2019).
- [16] D. L. Moehring *et al.*, *Entanglement of single-atom quantum bits at a distance*, Nature **449**, 68 (2007).
- [17] S. Ritter *et al.*, *An elementary quantum network of single atoms in optical cavities*, Nature **484**, 195 (2012).
- [18] J. Hofmann *et al.*, *Heralded Entanglement Between Widely Separated Atoms*, Science **337**, 72 (2012).
- [19] A. Delteil *et al.*, *Generation of heralded entanglement between distant hole spins*, Nature Physics **12**, 218 (2016).
- [20] R. Stockill *et al.*, *Phase-Tuned Entangled State Generation between Distant Spin Qubits*, Physical Review Letters **119**, 010503 (2017).
- [21] H. Bernien *et al.*, *Heralded entanglement between solid-state qubits separated by three metres*, Nature **497**, 86 (2013).
- [22] P. C. Humphreys *et al.*, *Deterministic delivery of remote entanglement on a quantum network*, Nature **558**, 268 (2018).

- [23] L. Jiang *et al.*, *Quantum repeater with encoding*, Physical Review A **79**, 032325 (2009).
- [24] H. K. C. Beukers *et al.*, *QuREBB*, *GitHub repository*, <https://github.com/QuTech-Delft/QuREBB> (2023).
- [25] V. Dobrovitski, G. Fuchs, A. Falk, C. Santori and D. Awschalom, *Quantum Control over Single Spins in Diamond*, Annual Review of Condensed Matter Physics **4**, 23 (2013).
- [26] F. Flamini, N. Spagnolo and F. Sciarrino, *Photonic quantum information processing: A review*, Reports on Progress in Physics **82**, 016001 (2018).
- [27] M. A. Nielsen and I. L. Chuang, *Quantum Computation and Quantum Information*, 10th ed. (Cambridge University Press, Cambridge ; New York, 2010).
- [28] C. Jones, D. Kim, M. T. Rakher, P. G. Kwiat and T. D. Ladd, *Design and analysis of communication protocols for quantum repeater networks*, New Journal of Physics **18**, 083015 (2016).
- [29] J. I. Cirac, P. Zoller, H. J. Kimble and H. Mabuchi, *Quantum State Transfer and Entanglement Distribution among Distant Nodes in a Quantum Network*, Physical Review Letters **78**, 3221 (1997).
- [30] I. Dror, A. Sandrov and N. S. Kopeika, *Experimental investigation of the influence of the relative position of the scattering layer on image quality: The shower curtain effect*, Applied Optics **37**, 6495 (1998).
- [31] S. Pirandola, *Satellite quantum communications: Fundamental bounds and practical security*, Physical Review Research **3**, 023130 (2021).
- [32] S. Daiss *et al.*, *A quantum-logic gate between distant quantum-network modules*, Science **371**, 614 (2021).
- [33] H. Bernien *et al.*, *Two-Photon Quantum Interference from Separate Nitrogen Vacancy Centers in Diamond*, Physical Review Letters **108**, 043604 (2012).
- [34] C. W. Chou *et al.*, *Measurement-induced entanglement for excitation stored in remote atomic ensembles*, Nature **438**, 828 (2005).
- [35] M. K. Bhaskar *et al.*, *Experimental demonstration of memory-enhanced quantum communication*, Nature **580**, 60 (2020), arxiv:1909.01323 .
- [36] M. L. Chan *et al.*, *Quantum state transfer between a frequency-encoded photonic qubit and a quantum-dot spin in a nanophotonic waveguide*, Physical Review A **105**, 062445 (2022).
- [37] S. Welte, B. Hacker, S. Daiss, S. Ritter and G. Rempe, *Cavity Carving of Atomic Bell States*, Physical Review Letters **118**, 210503 (2017).

- [38] A. Reiserer and G. Rempe, *Cavity-based quantum networks with single atoms and optical photons*, *Reviews of Modern Physics* **87**, 1379 (2015).
- [39] L. Heller, J. Lowinski, K. Theophilo, A. Padrón-Brito and H. de Riedmatten, *Raman Storage of Quasideterministic Single Photons Generated by Rydberg Collective Excitations in a Low-Noise Quantum Memory*, *Physical Review Applied* **18**, 024036 (2022).
- [40] N. Piro *et al.*, *Heralded single-photon absorption by a single atom*, *Nature Physics* **7**, 17 (2011).
- [41] A. D. Boozer, A. Boca, R. Miller, T. E. Northup and H. J. Kimble, *Reversible State Transfer between Light and a Single Trapped Atom*, *Physical Review Letters* **98**, 193601 (2007).
- [42] I. Aharonovich, D. Englund and M. Toth, *Solid-state single-photon emitters*, *Nature Photonics* **10**, 631 (2016).
- [43] N. Somaschi *et al.*, *Near-optimal single-photon sources in the solid state*, *Nature Photonics* **10**, 340 (2016).
- [44] P. J. Mosley *et al.*, *Heralded Generation of Ultrafast Single Photons in Pure Quantum States*, *Physical Review Letters* **100**, 133601 (2008).
- [45] C. P. Anderson *et al.*, *Electrical and optical control of single spins integrated in scalable semiconductor devices*, *Science* **366**, 1225 (2019).
- [46] T. Grange *et al.*, *Cavity-Funneled Generation of Indistinguishable Single Photons from Strongly Dissipative Quantum Emitters*, *Physical Review Letters* **114**, 193601 (2015).
- [47] H. Choi, D. Zhu, Y. Yoon and D. Englund, *Cascaded Cavities Boost the Indistinguishability of Imperfect Quantum Emitters*, *Physical Review Letters* **122**, 183602 (2019).
- [48] Q. Zhang *et al.*, *Demonstration of a scheme for the generation of “event-ready” entangled photon pairs from a single-photon source*, *Physical Review A* **77**, 062316 (2008).
- [49] K. C. Chen *et al.*, *Zero-Added-Loss Entangled-Photon Multiplexing for Ground- and Space-Based Quantum Networks*, *Physical Review Applied* **19**, 054029 (2023).
- [50] F. Ewert and P. van Loock, *Efficient Bell Measurement with Passive Linear Optics and Unentangled Ancillae*, *Physical Review Letters* **113**, 140403 (2014).
- [51] K. De Greve *et al.*, *Quantum-dot spin–photon entanglement via frequency downconversion to telecom wavelength*, *Nature* **491**, 421 (2012).
- [52] A. Tchebotareva *et al.*, *Entanglement between a Diamond Spin Qubit and a Photonic Time-Bin Qubit at Telecom Wavelength*, *Physical Review Letters* **123**, 063601 (2019).

- [53] J. Metz and S. D. Barrett, *Effect of frequency-mismatched photons in quantum-information processing*, Physical Review A **77**, 042323 (2008).
- [54] T.-M. Zhao *et al.*, *Entangling Different-Color Photons via Time-Resolved Measurement and Active Feed Forward*, Physical Review Letters **112**, 103602 (2014).
- [55] P. Kok *et al.*, *Linear optical quantum computing with photonic qubits*, Reviews of Modern Physics **79**, 135 (2007).
- [56] V. Krutyanskiy *et al.*, *Entanglement of Trapped-Ion Qubits Separated by 230 Meters*, Physical Review Letters **130**, 050803 (2023).
- [57] A. Pickston *et al.*, *Optimised domain-engineered crystals for pure telecom photon sources*, Optics Express **29**, 6991 (2021).
- [58] A. O. C. Davis, P. M. Saulnier, M. Karpiński and B. J. Smith, *Pulsed single-photon spectrometer by frequency-to-time mapping using chirped fiber Bragg gratings*, Optics Express **25**, 12804 (2017).
- [59] C. Figgatt *et al.*, *Parallel entangling operations on a universal ion-trap quantum computer*, Nature **572**, 368 (2019).
- [60] A. Reiserer *et al.*, *Robust Quantum-Network Memory Using Decoherence-Protected Subspaces of Nuclear Spins*, Physical Review X **6**, 021040 (2016).
- [61] K. Bergmann, N. V. Vitanov and B. W. Shore, *Perspective: Stimulated Raman adiabatic passage: The status after 25 years*, The Journal of Chemical Physics **142**, 170901 (2015).
- [62] S. Maity *et al.*, *Coherent acoustic control of a single silicon vacancy spin in diamond*, Nature Communications **11**, 193 (2020).
- [63] B. Pingault *et al.*, *Coherent control of the silicon-vacancy spin in diamond*, Nature Communications **8**, 15579 (2017).
- [64] G. de Lange, Z. H. Wang, D. Ristè, V. V. Dobrovitski and R. Hanson, *Universal Dynamical Decoupling of a Single Solid-State Spin from a Spin Bath*, Science **330**, 60 (2010).
- [65] C. T. Nguyen *et al.*, *Quantum Network Nodes Based on Diamond Qubits with an Efficient Nanophotonic Interface*, Physical Review Letters **123**, 183602 (2019).
- [66] P.-J. Stas *et al.*, *Robust multi-qubit quantum network node with integrated error detection*, Science **378**, 557 (2022).
- [67] L. Childress, J. M. Taylor, A. S. Sørensen and M. D. Lukin, *Fault-tolerant quantum repeaters with minimal physical resources and implementations based on single-photon emitters*, Physical Review A **72**, 052330 (2005).
- [68] C. H. Bennett *et al.*, *Purification of Noisy Entanglement and Faithful Teleportation via Noisy Channels*, Physical Review Letters **76**, 722 (1996).

- [69] D. Deutsch *et al.*, *Quantum Privacy Amplification and the Security of Quantum Cryptography over Noisy Channels*, *Physical Review Letters* **77**, 2818 (1996).
- [70] E. T. Campbell and S. C. Benjamin, *Measurement-Based Entanglement under Conditions of Extreme Photon Loss*, *Physical Review Letters* **101**, 130502 (2008).
- [71] N. Kalb *et al.*, *Entanglement distillation between solid-state quantum network nodes*, *Science* **356**, 928 (2017).
- [72] T. Wilk, S. C. Webster, A. Kuhn and G. Rempe, *Single-Atom Single-Photon Quantum Interface*, *Science* **317**, 488 (2007).
- [73] G. Wolfowicz *et al.*, *Quantum guidelines for solid-state spin defects*, *Nature Reviews Materials* **6**, 906 (2021).
- [74] A. H. K\"{u}ilerich and K. M\"{o}lmer, *Input-Output Theory with Quantum Pulses*, *Physical Review Letters* **123**, 123604 (2019).
- [75] A. H. K\"{u}ilerich and K. M\"{o}lmer, *Quantum interactions with pulses of radiation*, *Physical Review A* **102**, 023717 (2020).
- [76] B. E. Saleh and M. C. Teich, *Chapter 11*, in *Fundamentals of Photonics* (Wiley, 2019).
- [77] A. Yariv and P. Yeh, *Photonics: Optical Electronics in Modern Communications* (Oxford University Press, 2007).
- [78] K. Ngan, Y. Zhan, C. Dory, J. Vučković and S. Sun, *Quantum Photonic Circuits Integrated with Color Centers in Designer Nanodiamonds*, *Nano Letters* **23**, 9360 (2023).
- [79] H. Choi, M. Heuck and D. Englund, *Self-Similar Nanocavity Design with Ultrasmall Mode Volume for Single-Photon Nonlinearities*, *Physical Review Letters* **118**, 223605 (2017).
- [80] A. S. Sheremet, M. I. Petrov, I. V. Iorsh, A. V. Poshakinskiy and A. N. Poddubny, *Waveguide quantum electrodynamics: Collective radiance and photon-photon correlations*, *Reviews of Modern Physics* **95**, 015002 (2023).
- [81] M. O. Scully and M. S. Zubairy, *Quantum Optics* (Cambridge University Press, 1999).
- [82] P. G. Kwiat *et al.*, *New High-Intensity Source of Polarization-Entangled Photon Pairs*, *Physical Review Letters* **75**, 4337 (1995).
- [83] C. Couteau, *Spontaneous parametric down-conversion*, *Contemporary Physics* **59**, 291 (2018).
- [84] J. R. Johansson, P. D. Nation and F. Nori, *QuTiP: An open-source Python framework for the dynamics of open quantum systems*, *Computer Physics Communications* **183**, 1760 (2012).
- [85] T. Coopmans *et al.*, *NetSquid, a NETWORK Simulator for QUantum Information using Discrete events*, *Communications Physics* **4**, 1 (2021).

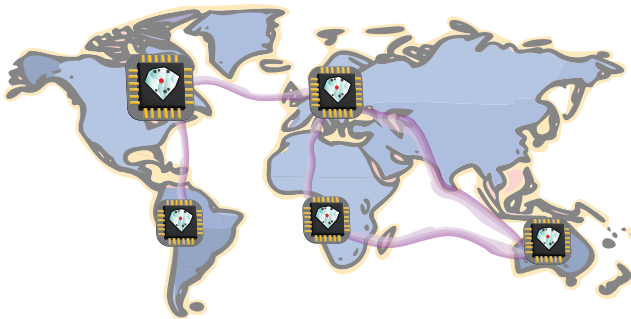
- [86] A. Dahlberg *et al.*, *A link layer protocol for quantum networks*, in *Proceedings of the ACM Special Interest Group on Data Communication, SIGCOMM '19* (Association for Computing Machinery, Beijing, China, 2019) pp. 159–173.
- [87] S. Diadamo, J. Nötzel, B. Zanger and M. M. Beşe, *QuNetSim: A Software Framework for Quantum Networks*, *IEEE Transactions on Quantum Engineering* **2**, 1 (2021).
- [88] T. Matsuo, C. Durand and R. Van Meter, *Quantum link bootstrapping using a RuleSet-based communication protocol*, *Physical Review A* **100**, 052320 (2019).
- [89] B. Bartlett, *A distributed simulation framework for quantum networks and channels*, (2018), arxiv:1808.07047 [physics, physics:quant-ph] .
- [90] G. Thiering and A. Gali, *Ab Initio Magneto-Optical Spectrum of Group-IV Vacancy Color Centers in Diamond*, *Physical Review X* **8**, 021063 (2018).
- [91] J. Dias, M. S. Winnel, N. Hosseinidehaj and T. C. Ralph, *Quantum repeater for continuous-variable entanglement distribution*, *Physical Review A* **102**, 052425 (2020).
- [92] Y. Zheng, H. Sharma and J. Borregaard, *Entanglement Distribution with Minimal Memory Requirements Using Time-Bin Photonic Qudits*, *PRX Quantum* **3**, 040319 (2022).
- [93] E. N. Knall *et al.*, *Efficient Source of Shaped Single Photons Based on an Integrated Diamond Nanophotonic System*, *Physical Review Letters* **129**, 053603 (2022).
- [94] R. E. Evans, *An Integrated Diamond Nanophotonics Platform for Quantum Optics*, Ph.D. thesis, Harvard University (2018).
- [95] M. Reck, A. Zeilinger, H. J. Bernstein and P. Bertani, *Experimental realization of any discrete unitary operator*, *Physical Review Letters* **73**, 58 (1994).
- [96] W. R. Clements, P. C. Humphreys, B. J. Metcalf, W. S. Kolthammer and I. A. Walmsley, *Optimal design for universal multiport interferometers*, *Optica* **3**, 1460 (2016).



6

CONCLUSIONS AND OUTLOOK

In this thesis, we reported experimental results on a spin-photon interface based on tin-vacancy (SnV) centers in diamond nanophotonic waveguides and introduced a theoretical framework for remote entanglement protocols. Here, we summarize the results and elaborate on the challenges and opportunities for the SnV center and diamond integrated photonics. In the context of group-IV color centers, we discuss how our framework can be used to gain relevant insights toward realizing large-scale, integrated quantum network nodes.



6.1. SUMMARY

This thesis discussed how to realize entanglement between spin-photon interfaces, and showed experimental results on a promising candidate for this task: tin-vacancy (SnV) centers integrated in diamond nanophotonic waveguides. The main results can be summarized as follows:

- **Chapter 3** discussed the fabrication of SnV implanted samples, showing how the inhomogeneous distribution of the optical transitions differs in different sample conditions. Here we also looked into the properties and stability of the SnV transition both in bulk diamond and integrated in nanophotonic waveguides, where we see narrow optical lines. Finally, after discussing theory and simulations for waveguide integration, we show the extinction of the transmission through the waveguide caused by interaction with a single SnV, with a contrast of $(35 \pm 1)\%$.
- In **Chapter 4** we investigated further the interaction between a single SnV in a waveguide and a coherent input field. We measure the effect of this interaction on the photon statistics of the transmitted and reflected fields. In the latter, we observe tunable interference between coherently scattered single photons and classical reflections of the driving field, which result in different photon statistics for different interference conditions. All the results agree very well with our theoretical model.
- **Chapter 5** introduced a modular theoretical framework for photon-mediated remote entanglement protocols. This framework provides a method to understand and categorize entanglement protocols in terms of abstract building blocks, and a playground to investigate and test new protocols by linking the building blocks to a specific hardware. To exemplify how the framework can be used, in this chapter we simulated the performance of different entanglement protocols using silicon-vacancy centers in diamond cavities as hardware. The framework allows to compare protocols at different levels of abstraction and experimental detail, which can provide useful insights in the choice of the best protocol for a specific hardware, or vice-versa the best hardware for a protocol.

6

We can use these results to outline a way to investigate architectures for the next generation of quantum network nodes. In a "top-down" approach, one can start by looking at the entanglement protocols in an abstract way, find the most suited type of spin-photon interface to implement them, and finally, quantum hardware to experimentally realize the spin-photon interface. We now take a "bottom-up" approach, as we loosely hint at with the structure of this thesis. We start from promising hardware (in our case the SnV center), investigate devices to enhance the spin-photon interface and create a scalable platform, and finally consider different protocols that are compatible with the latter.

6.2. HARDWARE: SNV CENTERS IN DIAMOND

As we have seen in Chapter 2, the SnV center offers promising features for realizing a scalable and efficient spin-photon interface. Nanophotonic integration, allowed by the

native robustness of Group-IV centers in noisy charge environments, is a strong motivation to go beyond the NV center as it paves the way for scalable integrated devices and enhancing the efficiency of the spin-photon interface. Within Group-IV centers the SnV shines as an advantageous platform for two main reasons. First, the overall efficiency of the optical transition, higher than for SiV and GeV, aside from allowing intrinsic higher entanglement generation rates, also translates into relaxed fabrication requirements to reach a significant cavity cooperativity or waveguide coupling. Second, the large ground state splitting grants operation at temperatures above or around 1.5 K, that can be reached without need for dilution refrigerators and thus relieve experimental complexity and cost, with the added advantage that it is easier to obtain higher cooling power.

6.2.1. THE OPEN CHALLENGES

There are still open challenges in the way of using the SnV as a quantum node.

Spin Control - Coherent microwave control of the SnV spin has been shown [1, 2]. The limited efficiency of driving the spin transition, which requires high powers and can result in detrimental heating of the diamond, keeps the integration of microwave delivery lines on-chip (as done with SiV [3]) still challenging. One way to address this is to use superconducting materials, although given the high current densities and high magnetic field usually involved in SnV experiments not all materials are suited and this approach is still under investigation. Hybrid integration could allow to thermally isolate the signal delivery lines, mitigating the issue. Working with highly strained SnVs, as done in Ref. [2], offers the twofold advantage of enhanced microwave susceptibility and tolerance to higher temperatures. However, making this approach scalable and high yield requires a way to consistently apply a controlled amount of strain in a device. Working in specific regimes of magnetic field orientation could allow efficient microwave control with lower power requirements [4], but it introduces a tradeoff with other system parameters such as the optical cyclicity. Microwave control is a flexible and scalable mechanism for spin control, but other techniques can be used: experimental demonstrations for SnV include all-optical coherent spin control in bulk diamond [5] and acoustic spin driving in a hybrid integrated device [6].

Frequency Tuning - Second-order electric field tuning [7, 8] and strain-based tuning using hybrid piezo devices and waveguides [6] have shown promising results and would be compatible with an on-chip architecture, but the tuning range is still limited to few GHz (up to 25 GHz on-chip for optimal position of the color center in the device). This challenge could be addressed by improving the inhomogeneous distribution [9] so that the range becomes sufficient for tuning most color centers present in the device. Quantum frequency conversion [10] of color centers to telecom wavelengths has been successfully employed in long-distance entanglement experiments for matching the frequency of color centers, with little technical overhead as it is required anyway for low-loss fiber transmission. Recently demonstrated hybrid integration of diamond nanostructures with thin-film lithium niobate photonics [11] could open the way to using quantum frequency conversion also in on-chip architectures [12].

Deterministic and Reliable Fabrication - While proof-of-principle experiments with SnV are gradually ticking the box of the main tasks and features required for quantum node operation, the overall yield of devices with suitable properties is often still limited, and spectral jumps or unstable optical behavior are observed for implanted Group-IV centers [13–15]. To increase the yield and scalability, the ideal case is to have a reliable and reproducible recipe for the fabrication of SnVs with stable optical properties and narrow frequency distribution and control over the position of the color centers to maximize the coupling to devices. There is ongoing work on improving SnV fabrication, aiming at reducing or healing the implantation damage [9, 16]. Tackling the spectral instability can also be done by addressing the local charge environment using laser light [17, 18] as demonstrated in Group-IV centers, or by modifying the diamond Fermi level [19, 20]. Even in the presence of some spectral diffusion, using charge-resonance heralding [21] can make sure that it does not affect the coherence during experiments. Towards more controlled defect fabrication, an interesting approach is to use focused ion beam (FIB) implantation, which allows for heralded and localized ion implantation and combined with laser-induced local generation of vacancies and annealing [22] could lead to near-unity yield, site-controlled generation of SnV centers.

6.2.2. THE OPPORTUNITIES

Memory Qubits - The use of nuclear spins in the diamond crystal as quantum memories would enable advanced applications in a quantum network [23], such as distributed computing and quantum error correction. Control of a single ^{13}C nuclear spin in the surrounding of a SiV center [3] was demonstrated, although with modest electron-nuclear gate fidelity of $\sim 59\%$. Building upon the tools established for ^{13}C control with the NV [24] could improve the fidelity of the nuclear spin control for Group-IV centers. Isotopes of Sn with non-zero nuclear spin [25], the most abundant being ^{117}Sn and ^{119}Sn , can also be used as an additional qubit. In SiV, using the spin of a ^{29}Si isotope [26] enables electron-nuclear gates with fidelity up to $\sim 99\%$, generation of nuclear spin-photon entanglement with fidelity up to 85% with the possibility of error correction, and operation at 4.3 K leveraging the more robust temperature response of the nuclear spin. The use of ^{117}SnV centers has already shown high fidelity initialization and readout of the nuclear spin in a waveguide [27].

High Temperature Operation - The temperature of operation of SnV of $\sim 1.5\text{ K}$ gives an advantage over other Group-IV centers. Existing approaches could increase even more the operation temperature, above $\sim 3\text{ K}$ which is easily reached in closed-cycle cryostats. We mentioned in Chapter 2 how, similarly to previous results in highly strained SiV [26, 28], SnV center with significant strain ($\Delta_{\text{GS}} \approx 1300\text{ GHz}$) have shown spin spin coherence in the $\sim \mu\text{s}$ range and average gate fidelity of $\sim 95\%$ at 4 K [2]. Devices that dynamically control [29] or induce static strain [30] can be leveraged to increase this effect even further. An alternative approach is to engineer the phononic density of states to suppress the phonon transition corresponding to the ground state energy splitting. This has led to increased orbital relaxation time for SiV in phononic crystals [31] and nanodiamonds [32]. However, for SiV where $\Delta_{\text{GS}} \approx 50\text{ GHz}$ the feature sizes needed for such devices are as small as $\sim 20\text{ nm}$. For SnV, with $\Delta_{\text{GS}} \approx 830\text{ GHz}$, this would require features

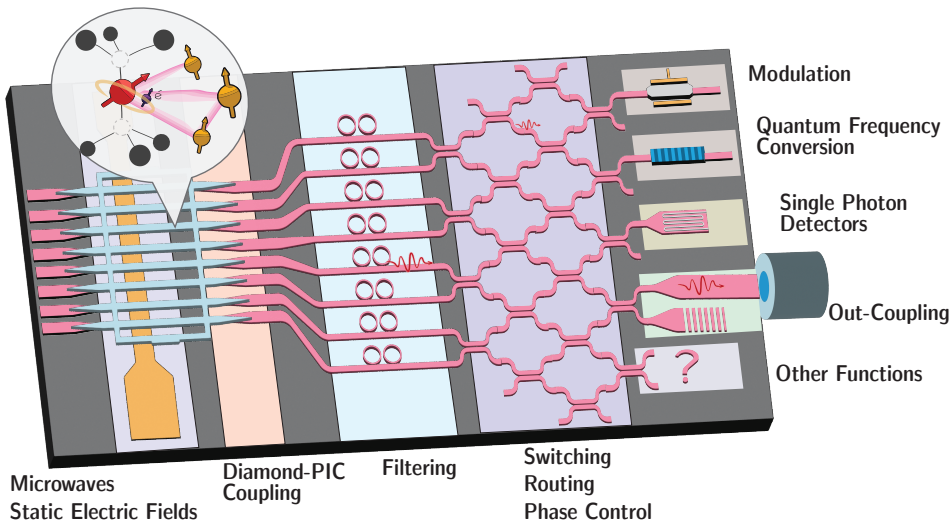


Figure 6.1: Depiction of a **Hybrid Integrated Quantum Device**. A color center with a nuclear spin register embedded in a diamond device is coupled to an integrated photonic and electronic circuit providing functionalities for spin control and photon operations.

of a few nm in size, which are currently extremely challenging to fabricate. Pushing the temperature of operation for the SnV would make for less demanding and more effective experimental systems, which offers a significant advantage for a scalable quantum network node.

6.3. AN INTEGRATED SPIN-PHOTON INTERFACE

6.3.1. CHALLENGES AND PROSPECTS FOR DIAMOND NANOPHOTONICS

Nanofabrication of photonic structures in diamond for color centers [33, 34] is a fast-developing field, and different approaches hold promises to overcome the current limitations. Fabrication by structuring devices in bulk diamond using angled plasma etch [35] or quasi-isotropic undercut [36] has led to good results, but the possible device designs are limited by orientation-dependent and directional etch recipes. Both methods do not allow arbitrary curves and thicknesses. For this reason, these approaches are especially interesting for hybrid integration where complex photonic structures are not fabricated in the diamond material. Quasi-isotropic undercut also allows for two-dimensional devices such as microdisks [37] and 2D photonic crystals [38], which can potentially be interesting for optomechanics applications [39]. Device fabrication in diamond membranes would enable more flexible designs, but it is currently limited by the challenges of reliably obtaining nanometer-thin membranes bonded to a substrate. Thinning down membranes from substrates that are several micrometers thick [40, 41]

is possible but requires a very long etch and often results in rough and uneven surfaces and micromasking. Using a smart-cut method [42] already demonstrated high-quality diamond membranes down to 10 nm thin and bonded to a variety of substrate materials [43], but further development is needed to make this technique scalable and increase the membrane size.

6.3.2. HYBRID PHOTONIC INTEGRATION

Diamond is an excellent material for quantum devices, but it lacks the flexibility of other platforms with more established fabrication techniques. A solution is to integrate small diamond-based quantum chips with other materials that provide the photonic and electronic functionalities [44]. Silicon nitride is a mature visible photonic platform [45] and can be handled at a commercial scale in several foundries worldwide. Its broad transparency range, very low loss, and mature fabrication make it excellent for passive devices, however, it lacks strong non-linear effects which are needed for many active components. On the other hand, other materials such as aluminum nitride (AlN) [46] and lithium niobate (LN) [47] are emerging as flexible and resourceful platforms, combining low loss with sizable piezoelectric and non-linear optical coefficients, which can be leveraged to realize on-chip modulators, switches and frequency conversion devices. Diamond devices containing the quantum nodes can be integrated with the photonic integrated circuit (PIC) by transfer printing [48] or pick-and-place [11, 49].

6

Hybrid integration could enable scalable, modular and compact multi-qubit devices where the quantum systems, control lasers, photon routing and filtering and detection are combined in the same chip, as schematically depicted in Fig. 6.1, or interfaced in the same packaging. While many of these components already exist and are developed for classical integrated photonic, they still present high losses. Complete photon routing and control on-chip would require many high-speed switches and filters, which add significant loss. For many applications, a solution can be to limit the connectivity and trade-off between flexibility of the on-chip routing and loss tolerance. In the intermediate term, some functionalities can be realized off-chip or in free-space. For out-coupling light from chip to free-space or optical fibers several methods have been tested [50] but most work focuses on the telecom wavelength range, while for visible light the technology and commercial availability are still immature. Another challenging task is interfacing the different components. The experimental efficiency of the diamond-to-PIC coupling using evanescent field transfer in pick-and-place devices was measured up to ~ 40% with AlN [49] and ~ 90% with LN [11].

A different approach to hybrid integration that can solve this issue is to have devices not in diamond but in the PIC material and evanescently couple to color centers in diamond membranes [51] or nanodiamonds [52], leading to overall lower emitter-device coupling than diamond-based systems but potentially higher device quality and yield as it can make use of more established fabrication.

6.3.3. CAVITY OR WAVEGUIDE-BASED QUANTUM NODES

Thanks to the high optical transition efficiency, it is easier to obtain high cooperativity for SnV centers in cavities than it is for SiV. State-of-the-art experiments with SiV report a cooperativity up to $C = 38$ [3] for a cavity with quality factor $Q \approx 12000$. Results on SnV centers showed Purcell factors of $F_p = 37$ [53] and 25 [54] in cavities with $Q \sim 3000$ and ~ 2000 , respectively. Considering the optical transition efficiency $\zeta = 0.36$ we can estimate the corresponding cooperativities to be $C \sim 13$ and ~ 9 , which shows how significantly lower quality factors can already give competitive results. The recent realization of entanglement between two SiV centers uses devices with cooperativities of ~ 12 and 1.5, which is sufficient for a reflection contrast of $\sim 90\%$, meaning that current state-of-the-art devices with SnV centers would already give an improvement. Photonic crystal cavities in diamond at SnV wavelengths have been fabricated with quality factors up to $\sim 10^4$ [53], which can potentially be improved by using fabrication that minimizes the surface roughness or trying alternative designs that are more robust against fabrication errors [55].

The use of cavity-based devices offers the obvious advantage that the coupling strength can be engineered and increased, leading to more efficient and higher fidelity entanglement generation for spin-photon interfaces using either photon emission or conditional reflection. However, this comes at the cost of additional experimental complexity in the device fabrication and requires tuning mechanisms for the frequency of each cavity.

In waveguide-based devices, the emission in the waveguide single mode grants efficient photon collection [27, 56], and the single-photon coherent scattering can be used for conditional reflection [57], so it can be used as a spin-photon interface in a similar way to cavities. Waveguides are broadband, so they do not require tuning and can work for several emitters at different frequencies. Furthermore, they are far less demanding in terms of fabrication and positioning of the emitter. This makes waveguides a good candidate for large-scale on-chip systems, where the individual tuning of cavities and the associated drifts can add significant experimental overhead, and the broadband nature could potentially enable spectral multiplexing of the emitters. Waveguide devices require less precise fabrication and are less sensitive to imperfections than cavities, potentially resulting in more reliable production and higher device yield. This comes at the expense of lower efficiency of the spin-photon interface. The coupling is fundamentally limited by the transition efficiency to $\beta \leq 0.37$, which corresponds to a modulation of the transmission with a contrast of $\Delta T \leq 0.6$. It is possible to design entanglement protocols where the imperfect extinction does not affect the fidelity but only the success probability, thus this does not directly hinder the use of waveguide for conditional reflection. Using photonic crystal waveguides or working at the edge of a photonic bandgap, where the local density of states is enhanced for slow-light modes, could be a way to enhance the interaction. For quantum dots, this type of device can lead to $\beta > 0.9$ [58]. A similar approach could be used for SnV centers, keeping the advantage of relaxed tuning requirements since photonic crystal waveguides can have a large bandwidth, but at the cost of having fabrication challenges similar to photonic crystal cavities.

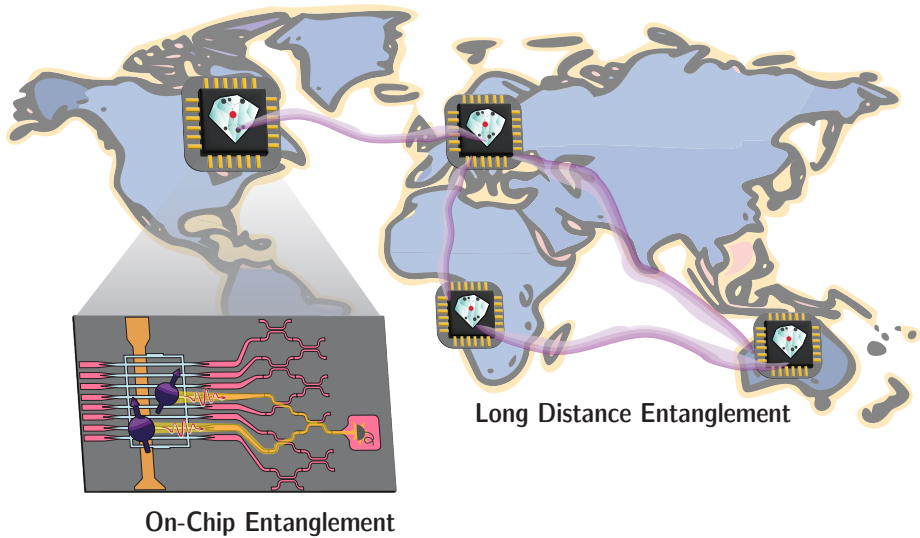


Figure 6.2: In the **long term vision**, local integrated devices where on-chip entanglement can connect several color centers form the basis of a larger, long-distance network.

6.4. FIND THE BEST ENTANGLEMENT PROTOCOL

6.4.1. COMPARING PROTOCOLS

The framework discussed in Chapter 5 can be useful to identify the most suited entanglement protocol for different hardware or experimental settings, such as long-distance or on-chip architectures, as depicted in Fig. 6.2.

On a low level, it is possible to complement the framework with arbitrary levels of details of the hardware, noise sources, and experiment protocol to gain insight into how to improve the spin-photon interface. For example, from the simulation results presented in Chapter 5 we can draw two conclusions for the platform we studied. First, increasing the cooperativity is not always necessary or advantageous to improve the entanglement protocol. We simulated this for conditional photon reflection, where a too high cooperativity results in a non-optimal cavity-emitter spectrum, especially approaching the strong coupling regime. Also in an emission-based spin-photon interface, having a short Purcell-enhanced lifetime entails experimental complications as the timescale for excitation pulses become extremely short and high powers are required. This conclusion suggests that increasing the cavity quality factors far beyond the current state of the art might not give a significant advantage, compared for example to working on reproducibility and robustness of the fabrication which would give better control of the system operation conditions. Second, using weak coherent states in place of single photons gives a significant disadvantage both in rate and fidelity. Using single photons is harder to implement experimentally, but the development of efficient single-photon

sources would make the use of scattering-based protocols more advantageous. Photon sources based on the same defect as the spin-photon interface (e.g. SnV or SiV) could be integrated in the same architecture. This shows how the framework can help in identifying the limitations and opportunities of a platform. Adding even more experimental details to the simulation and increasing the free parameters to sweep allows to find the optimal configuration for the spin-photon interface and where to invest efforts for improving it.

On a higher level, the framework can be used to extract relevant parameters on the entanglement protocols that can serve as a basis for software modeling of larger networks [59–61]. The abstract logical building blocks and topology can also provide a tool to inform the design of large-scale devices, better understanding how elements such as the connectivity between nodes, photon routing, and the practical constraints of sources, detectors, and spin-photon interfaces relate to the available protocols.

6.5. CONCLUSIONS

Color centers in diamond are at the forefront of quantum network experiments, with the prospect of serving as a flexible platform also for quantum simulation, computing and sensing. The integration in nanophotonic structures of Group-IV centers opens a new, wide playground for designing novel, scalable, and efficient quantum devices and entanglement protocols with the potential to push quantum science even faster in the transition to an applied and largely available technology.

BIBLIOGRAPHY

- [1] E. I. Rosenthal *et al.*, *Microwave Spin Control of a Tin-Vacancy Qubit in Diamond*, (2023), arxiv:2306.13199 [cond-mat, physics:quant-ph] .
- [2] X. Guo *et al.*, *Microwave-based quantum control and coherence protection of tin-vacancy spin qubits in a strain-tuned diamond membrane heterostructure*, (2023), arxiv:2307.11916 .
- [3] C. T. Nguyen *et al.*, *An integrated nanophotonic quantum register based on silicon-vacancy spins in diamond*, *Physical Review B* **100**, 165428 (2019).
- [4] G. Pieplow, M. Belhassen and T. Schröder, *Efficient Microwave Spin Control of Negatively Charged Group-IV Color Centers in Diamond*, (2023), arxiv:2312.02637 [quant-ph] .
- [5] R. Debroux *et al.*, *Quantum Control of the Tin-Vacancy Spin Qubit in Diamond*, *Physical Review X* **11**, 041041 (2021).
- [6] G. Clark *et al.*, *Nanoelectromechanical control of spin-photon interfaces in a hybrid quantum system on chip*, (2023), arxiv:2308.07161 [quant-ph] .
- [7] L. De Santis, M. Trusheim, K. Chen and D. Englund, *Investigation of the Stark Effect on a Centrosymmetric Quantum Emitter in Diamond*, *Physical Review Letters* **127**, 147402 (2021).
- [8] S. Aghaeimeibodi, D. Riedel, A. E. Rugar, C. Dory and J. Vučković, *Electrical Tuning of Tin-Vacancy Centers in Diamond*, *Physical Review Applied* **15**, 064010 (2021).
- [9] Y. Narita *et al.*, *Identical Photons from Multiple Tin-Vacancy Centers in Diamond*, (2022), arxiv:2208.06275 [quant-ph] .
- [10] A. Stolk *et al.*, *Telecom-Band Quantum Interference of Frequency-Converted Photons from Remote Detuned NV Centers*, *PRX Quantum* **3**, 020359 (2022).
- [11] D. Riedel *et al.*, *Efficient Photonic Integration of Diamond Color Centers and Thin-Film Lithium Niobate*, *ACS Photonics* **10**, 4236 (2023).
- [12] X. Wang *et al.*, *Quantum frequency conversion and single-photon detection with lithium niobate nanophotonic chips*, *npj Quantum Information* **9**, 1 (2023).
- [13] A. E. Rugar *et al.*, *Narrow-Linewidth Tin-Vacancy Centers in a Diamond Waveguide*, *ACS Photonics* **7**, 2356 (2020).
- [14] R. E. Evans *et al.*, *Photon-mediated interactions between quantum emitters in a diamond nanocavity*, (2018).
- [15] N. H. Wan *et al.*, *Large-scale integration of artificial atoms in hybrid photonic circuits*, *Nature* **583**, 226 (2020).

- [16] A. E. Rugar *et al.*, *Generation of Tin-Vacancy Centers in Diamond via Shallow Ion Implantation and Subsequent Diamond Overgrowth*, *Nano Letters* **20**, 1614 (2020).
- [17] J. A. Zuber *et al.*, *Shallow Silicon Vacancy Centers with lifetime-limited optical linewidths in Diamond Nanostructures*, (2023), arxiv:2307.12753 [cond-mat, physics:quant-ph] .
- [18] J. Görlitz *et al.*, *Coherence of a charge stabilised tin-vacancy spin in diamond*, *npj Quantum Information* **8**, 45 (2022).
- [19] B. C. Rose *et al.*, *Observation of an environmentally insensitive solid-state spin defect in diamond*, *Science* **361**, 60 (2018).
- [20] T. Murai *et al.*, *Engineering of Fermi level by *nin* diamond junction for control of charge states of NV centers*, *Applied Physics Letters* **112**, 111903 (2018).
- [21] J. M. Brevoord *et al.*, *Heralded initialization of charge state and optical transition frequency of diamond tin-vacancy centers*, (2023), arxiv:2311.11962 [quant-ph] .
- [22] Y.-C. Chen *et al.*, *Laser writing of individual nitrogen-vacancy defects in diamond with near-unity yield*, *Optica* **6**, 662 (2019).
- [23] M. H. M. A. Abobeih, *From Atomic-Scale Imaging to Quantum Fault-Tolerance with Spins in Diamond*, Ph.D. thesis (2021).
- [24] C. Bradley, *Order from Disorder: Control of Multi-Qubit Spin Registers in Diamond*, Ph.D. thesis, Delft University of Technology (2021).
- [25] I. B. W. Harris *et al.*, *Hyperfine Spectroscopy of Isotopically Engineered Group-IV Color Centers in Diamond*, (2023), arxiv:2306.00164 [quant-ph] .
- [26] P.-J. Stas *et al.*, *Robust multi-qubit quantum network node with integrated error detection*, (2022), arxiv:2207.13128 [quant-ph] .
- [27] R. A. Parker *et al.*, *A diamond nanophotonic interface with an optically accessible deterministic electronuclear spin register*, (2023), arxiv:2305.18923 .
- [28] Y.-I. Sohn *et al.*, *Controlling the coherence of a diamond spin qubit through its strain environment*, *Nature Communications* **9**, 2012 (2018).
- [29] S. Meesala *et al.*, *Strain engineering of the silicon-vacancy center in diamond*, *Physical Review B* **97**, 205444 (2018), arxiv:1801.09833 [cond-mat, physics:quant-ph] .
- [30] D. R. Assumpcao *et al.*, *Deterministic Creation of Strained Color Centers in Nanostructures via High-Stress Thin Films*, (2023), arxiv:2309.07935 [physics, physics:quant-ph] .
- [31] K. Kuruma *et al.*, *Engineering Phonon-Qubit Interactions using Phononic Crystals*, (2023), arxiv:2310.06236 [physics, physics:quant-ph] .

- [32] M. Klotz *et al.*, *Prolonged Orbital Relaxation by Locally Modified Phonon Density of States for the Si^{V} Center in Nanodiamonds*, Physical Review Letters **128**, 153602 (2022).
- [33] S. Mi, M. Kiss, T. Graziosi and N. Quack, *Integrated photonic devices in single crystal diamond*, Journal of Physics: Photonics **2**, 042001 (2020).
- [34] P. K. Shandilya *et al.*, *Diamond Integrated Quantum Nanophotonics: Spins, Photons and Phonons*, Journal of Lightwave Technology **40**, 7538 (2022).
- [35] M. J. Burek *et al.*, *Free-Standing Mechanical and Photonic Nanostructures in Single-Crystal Diamond*, Nano Letters **12**, 6084 (2012).
- [36] S. Mouradian, N. H. Wan, T. Schröder and D. Englund, *Rectangular photonic crystal nanobeam cavities in bulk diamond*, Applied Physics Letters **111**, 021103 (2017).
- [37] M. Mitchell, D. P. Lake and P. E. Barclay, *Realizing $Q > 300\,000$ in diamond microdisks for optomechanics via etch optimization*, APL Photonics **4**, 016101 (2019).
- [38] N. H. Wan, S. Mouradian and D. Englund, *Two-dimensional photonic crystal slab nanocavities on bulk single-crystal diamond*, Applied Physics Letters **112**, 141102 (2018).
- [39] A. H. Safavi-Naeini, D. V. Thourhout, R. Baets and R. V. Laer, *Controlling phonons and photons at the wavelength scale: Integrated photonics meets integrated phononics*, Optica **6**, 213 (2019).
- [40] M. Challier *et al.*, *Advanced Fabrication of Single-Crystal Diamond Membranes for Quantum Technologies*, Micromachines **9**, 148 (2018).
- [41] M. Ruf *et al.*, *Optically Coherent Nitrogen-Vacancy Centers in Micrometer-Thin Etched Diamond Membranes*, Nano Letters **19**, 3987 (2019).
- [42] X. Guo *et al.*, *Tunable and Transferable Diamond Membranes for Integrated Quantum Technologies*, Nano Letters **21**, 10392 (2021).
- [43] X. Guo *et al.*, *Direct-bonded diamond membranes for heterogeneous quantum and electronic technologies*, (2023), arxiv:2306.04408 [physics, physics:quant-ph] .
- [44] A. W. Elshaari, W. Pernice, K. Srinivasan, O. Benson and V. Zwiller, *Hybrid integrated quantum photonic circuits*, Nature Photonics **14**, 285 (2020).
- [45] C. Xiang, W. Jin and J. E. Bowers, *Silicon nitride passive and active photonic integrated circuits: Trends and prospects*, Photonics Research **10**, A82 (2022).
- [46] N. Li *et al.*, *Aluminium nitride integrated photonics: A review*, Nanophotonics **10**, 2347 (2021).
- [47] B. Desiatov, A. Shams-Ansari, M. Zhang, C. Wang and M. Lončar, *Ultra-low-loss integrated visible photonics using thin-film lithium niobate*, Optica **6**, 380 (2019).

- [48] L. Li *et al.*, *Heterogeneous integration of spin-photon interfaces with a scalable CMOS platform*, (2023), arxiv:2308.14289 [physics, physics:quant-ph] .
- [49] N. H. Wan *et al.*, *Efficient Extraction of Light from a Nitrogen-Vacancy Center in a Diamond Parabolic Reflector*, *Nano Letters* **18**, 2787 (2018).
- [50] G. Son, S. Han, J. Park, K. Kwon and K. Yu, *High-efficiency broadband light coupling between optical fibers and photonic integrated circuits*, *Nanophotonics* **7**, 1845 (2018).
- [51] S. Chakravarthi *et al.*, *Hybrid Integration of GaP Photonic Crystal Cavities with Silicon-Vacancy Centers in Diamond by Stamp-Transfer*, *Nano Letters* **23**, 3708 (2023).
- [52] K. G. Fehler *et al.*, *Hybrid Quantum Photonics Based on Artificial Atoms Placed Inside One Hole of a Photonic Crystal Cavity*, *ACS Photonics* **8**, 2635 (2021).
- [53] K. Kuruma *et al.*, *Coupling of a single tin-vacancy center to a photonic crystal cavity in diamond*, *Applied Physics Letters* **118**, 230601 (2021).
- [54] A. E. Rugar *et al.*, *Quantum Photonic Interface for Tin-Vacancy Centers in Diamond*, *Physical Review X* **11**, 031021 (2021).
- [55] T. Pregolato *et al.*, *Fabrication of Sawfish photonic crystal cavities in bulk diamond*, (2023), arxiv:2311.03618 [physics, physics:quant-ph] .
- [56] J. Arjona Martínez *et al.*, *Photonic Indistinguishability of the Tin-Vacancy Center in Nanostructured Diamond*, *Physical Review Letters* **129**, 173603 (2022).
- [57] M. L. Chan *et al.*, *On-chip spin-photon entanglement based on photon-scattering of a quantum dot*, *npj Quantum Information* **9**, 1 (2023).
- [58] M. Arcari *et al.*, *Near-unity coupling efficiency of a quantum emitter to a photonic-crystal waveguide*, *Physical Review Letters* **113**, 093603 (2014), arxiv:1402.2081 [physics, physics:quant-ph] .
- [59] T. Coopmans *et al.*, *NetSquid, a NETWORK Simulator for QUANTUM Information using Discrete events*, *Communications Physics* **4**, 1 (2021).
- [60] S. Diadamo, J. Nötzel, B. Zanger and M. M. Beşe, *QuNetSim: A Software Framework for Quantum Networks*, *IEEE Transactions on Quantum Engineering* **2**, 1 (2021).
- [61] B. Bartlett, *A distributed simulation framework for quantum networks and channels*, (2018), arxiv:1808.07047 [physics, physics:quant-ph] .



ACKNOWLEDGEMENTS

Finally, the last pages of this book are dedicated to those who, in different ways, made my PhD and in general the last 4+ years a unique experience.

Ronald, you manage to create an amazing mix of top-notch research, a fun and engaging team environment, and attention to the personal growth of each group member. Thank you for the opportunities and guidance you gave me: the experience I got and the amount I have learned from you and from the group over my PhD years can't be quantified (but it was for sure worth that exhausting bike ride to the beach on my interview day). It has been a pleasure to kick off the "tin" endeavor in the group. From our hours-long explorative paper readings of the first year to the brainstorming sessions of the later times, it has been an inspiring and enjoyable journey. I am sure Team Diamond will thrive on the new adventures and challenges ahead.

Carlos, since our first encounter in Boston I had the impression that you are a smart scientist and a kind person. I'm sure you will make for an amazing PI, both at the personal and the scientific level! Thanks for accepting to be my last-minute co-promotor. I enjoyed the scientific (and non-scientific) chats we had in this short period, and I hope we will have chances for more in the future.

Johannes, thanks for being my co-promotor while in Delft. It was truly useful and a lot of fun to have you involved in the tin project, always available to shed some light on my theory doubts or unexpected results. Good luck with your new endeavors in Boston!

Thanks to **Tim Schröder**, **Yiwen Chu**, **Miriam Blaauboer**, **Kobus Kuipers** and **Sander Otte** for accepting to join my committee. I'm looking forward to a nice discussion on the defense day!

The two people dressed up as penguins and standing next to me summarize very well the intertwined work and human environments that made a big part of my PhD years.

Hans, although you are a few phd-months younger, we basically went through this whole thing together. I love how we would end up in our "usual arguments" and always find a solution that pushes us further. I grew a lot thanks to this and all the experiences with you, who are always keen on sharing your endless curiosity. I'm happy that we *eventually* managed to go on our sea, mountain, and road trip adventures! I wish you, **Sophie** and **Hannah** a great load of happiness wherever life will bring you.

Nic, this penguin suit is for all the times you gave me a sofa when I was in need (and vice-versa), for when you endured my γιριλλας or the over-excited moments, and for the countless nights blowing off steam by playing tunes or shaking a cocktail. One of the best things you can wish for to go through a PhD is someone who's there and shares

your experiences. You(r face) have been this for me for the last years. Yo, thanks.

One of the most fulfilling parts of this journey has been to see the “Tin-Team” grow, and the motivation and verve that pushed the project where it is now. **Nina**, you can do magic with a pair of tweezers and a few beakers: we give you a plain, square piece of diamond and you make the most amazing nano-sculptures out of it. Thanks for these years of cheering up each other’s frustrations and celebrating big and small victories. **Chris**, you became part of my routine so fast, both inside and outside the lab, that at some point I couldn’t tell if it was your first year or if you’d been around all the time. Luckily, I had to order beers for you, which at least gave me a one-year time reference. Pingu is in good hands (noot-noot). **Tim**, you jumped straight into the action and I was really happy to be your “daily supervisor”. Whether it’s crafting mugs or fixing code, your relaxed and dynamic mood makes it always enjoyable to be around you. **Julia**, thanks for your cheerful energy and all the ideas and activities that keep Team Diamond the great environment it is. **Lorenzo**, it was nice to work with you at the start of the project and see you come back to Delft. Thanks for all the help, always delivered in the most calm and peaceful way. **Dani**, keep on asking your nasty but well-thought questions, I’m sure this will contribute to pushing the Tin-Team’s knowledge far. Good luck with VLT2! **Leo**, you will soon begin the PhD journey already as a senior group member and beholding extensive e-beam knowledge. That makes for a great start!

Christian, your contribution in building up the core project of my PhD, and in helping me become a better supervisor, was crucial. Thank you for this and the wine-assisted chats on the meaning of research and politics. I’m very happy that you joined the group and I’m looking forward to seeing what you will get out of those boiled silicon pieces. **Adriá**, we had some exciting times in the lab with a bunch of “first-time” measurements! I am very grateful for that and for all the troubles and cool results that we went through together. Good luck, and always keep up your ambitious goals.

Team Diamond is a great mix of people and makes for great *vibes*[™]. Thanks **Arian** for our US adventures and the related endless discussions, and for being my sommelier of electronic music. Looking forward to reading your propositions very soon. **Yanik**, I remember when you started with an empty lab and a packed-up cryostat, it’s amazing to see how far it got and I’m happy we eventually managed to put some tins in the cavity and bridge the two projects! Thanks for all the creative ideas and Diamond merch over the years. **Julius**, thanks for all the cavity-related discussions, always fun and enlightening. I’m sure you will do great with networks too, and keep the Hansonlab team strong in the Diamond Olympics to come. **Mariagrazia**, it’s always helpful to have a friendly face on the other side of the desk to complain about the everyday struggles, thanks for that! **Kian**, I enjoyed our drive through the canyons, and it’s always interesting to hear your view on the application side of quantum. Good luck with finishing up. **Niv**, it’s great that you’re bringing a theory perspective to the group. Good luck, and I hope you end up enjoying the lab too. **Max**, you guided me a lot at the beginning of my PhD both on the tins and starting up the Delft-MIT chats. Thanks a lot for this, and all the nights at your place with Ciao Ciao pizzas and home-brewed beers. **Matthew**, you were

of great help in getting me started in my early times, and I enjoyed working on cavities with you. Thanks! **Marie-Christine**, thanks for many cheering-up coffee-machine chats and for an amazing Viennese wedding. I wish you and **Josh** a lot of happiness! **Alejandro**, thanks for being the favorite Spanish postdoc of Team Diamond for a while. Have fun in London! **Matteo P. Sr.**, thanks for all the coding tips and for introducing me to Peperoncino. It was good to see you again in the US. **Sophie**, talking science with you was always insightful. It's great to see that you're already onto another 3-node network! **Simon**, I enjoyed the time with you in the group. Looking forward to seeing what comes out of your Innsbruck lab.

Thanks also to all the **MSc students** who contributed to building up both the scientific and social life of the group. In particular the brave ones who decided to jump in the unknowns of the tin project: **Chris, Kamiel, Sarel, Zarije, Caroline, Sezer, Elvis, Leo, Pepijn** and **Timo**.

With the rest of Team Diamond I shared a lot of daily coffee chats, both physics-related and not, regular TPKVs and drinks around Delft, occasional crazy conference experiences, and so on. **Tim T.**, your group and research results are really amazing and inspiring. **Hans B.**, it seems like yesterday we were sitting in LT2b trying to fix piezos. Good luck on the TNO side. **Laurens**, I enjoyed exploring Benasque with your Spanish alter-ego. Looking forward to seeing some more nice nano-pics and SiC results from you and **Gerben**. **Kai**, thanks for the fun times in Denver and for not completely bashing me at tiny-table-tennis. **Guido**, we survived the deep Minnesota countryside with bears and sketchy houses: the last steps of your PhD will be a piece of cake now. **Sjoerd**, thanks for the many jokes and funny chats, and for giving us King Fridge. Best of luck with your defense. **Benjamin v. O.**, you are a programming guru and always available to help. Thanks! **Margriet** and **Christina**, it was fun to play with you on the strings at the Christmas party! Thanks for all the nice lunch-table chats. **Jiwon**, I understood GST more thanks to your engaging vending machine presentations. **Damian**, thanks for the several times you helped me out with practical matters. I wish you all the best in Poland. **Benjamin P.**, your expertise on Group-IV centers was super useful at the start of my project. **Takashi**, with your cool grown diamonds you made my first SnV sample possible, thanks! **Anta**, see you soon on the beach in Barcelona. **Maarten**, we had quite some crazy and fun nights, from the Performance Bar to ADE. **Mohamed**, chatting with you always leaves precious insights. It was nice to visit you in Boston! **Joe**, it was fun to play music in the band with you for a bit. **Conor**, seeing you again around the QuTech corridors is a great throwback feeling. Good luck with your new adventure!

The "MIT-Delft family meetings" were a constant appointment during my PhD. Thanks **Chuck** for the long chats trying to make some sense of entanglement protocols, the friendly dinners, and for being the best Boston tour guide (twice).

A very special thanks to my *vèz* **Will** for our usual beers and dinners, the late-night jamming, the lessons on *Ozzy* geography, and all the rest. They make some of the best memories of my time here, together with some recordings of vocal harmonies after too many drinks.

In QuTech, I never missed practical support and enjoyable moments when I needed them. Thanks to all the technicians and support staff who many times helped me get out of trouble or solve technical issues. Thanks to all the people who have made QuTech feel much more than just a workplace, a full list would be very long. A special thanks for all the adventures inside and outside this building to **Pablo, Hanifa, Irene, Uri, Vicky, Davide, Maia, Brennan, Alberto, Karina, Daniel. Tobì**, thanks for the massages.

Meu amigo **Luiz**, how strange is life: one random day you stop me on the street, and in no time we are partying together with **Su** in Ponta Grossa at the "*wedding*" of you and **Barbara**. That encounter was also the start of the jamming nights with **Will, Luiz** and **Su**. You folks made one of the best chapters of my time in Delft, thanks for the good times and the questionably good music. And thanks to those who passed by **Oude Langendijk** for listening to our musical shenanigans.



If you open a cupboard in a meeting room at QuTech there is a good chance that instead of books and office supplies, you find a drum kit. I had a great time playing with the **Q2**, thanks to all the musicians who passed by over the years: **Will, Hans, Chris, Gustavo, Maia, Floor, Anne-Marije, Pablo, Bart, Julia, Nic, Colin, Christina, Margriet, Zarije, Laurens, Joe, Conor, Luc, Timo, Guido, Sander**. Good luck to all the new ones who joined later. It's good to see that the weekly post-practice pizza at Peperoncino is still on. Gustavo, I know that deep down you prefer sgroppino but just wanted to tease me.

When you live abroad, you end up having more than one home and something close to a second family. My first *home* in the Netherlands was **Vero's** house, which introduced me to "Rotty" even before I moved here and marked the start of our Italian-style Sunday lunches.

You don't choose your second family, you just find it. But if you're lucky you can find an **Ale**, always ready with a bottle of wine and a guitar to drag you to the park at the first ray of sun, or a **Ciro** who will try to teach you Neapolitan songs (luckily I have a **B1** now). There might be two **Claudias** already planning the next house party. For sure **Leo** will arrive late, but he will bring Aperol and prosecco, so **Giacomo**: *fame un spriss!*

There would be so much to write about everyone and everything, that it would take two books. I will keep it as a good stash of fun stories to tell and, for now, just throw a big THANKS for making my time here unforgettable to **Vero, Marcoggiú, Ale, Ciro, Leo, Pippo, Musillo, Claudia C., Claudia M., Alba, Marta, Candida, Domi, Giacomo, Claudia B., Lara, Patteo, Fabio, Jasmineen, Silvia, Marco, Gregori, Daniele, Giulia, Lily, Alessio, Davide, Mario**, and all the other **Nonnen** and **Lisippi** and **Rotterdamers** who were a part of this life chapter.

If you like the cover of this thesis, that's also thanks to the professional tips of **Lara, Claudia, and Babbo**.

Even with our busy lives, with **Colectivo Mariachi** we managed to make some good music and have fun. Thanks, folks!

There are the kind of people that you meet at a certain point in your life, and although you get separated in space, every time you see them it feels like you never parted. I am grateful for having such people, like **Giacomino, Paolo, Fabio, Iuri, Ninni, MatteoCarli**, the **Band of Physicists**, the old crew of **Casa Melanzane**. Thanks for all the occasions (with some more often, with some less) to be together like the old days.

Thanks to **i Regaz della Clips**, and all the other friends of a lifetime who make Riolo City feel like home whenever I'm back.

Se dopo oggi *la società può fare affidamento sul mio giudizio*, é in larga parte grazie all'esempio, al confronto e al supporto che **Mamma Stefania, Babbo Paolo e Michele** non mi hanno mai fatto mancare in questi 29-e-qualcosa anni. Grazie anche a **Nonna Giuliana, Nonno Elio e Nonna Emilia** che mi vogliono bene al punto da appoggiare le mie scelte anche quando significa essere meno spesso a casa.

Grazie a **Nonno Duilio**, per tutto quello che ho imparato da lui.

While approaching the end of this, I am aware that I have not written all the names I wish I had, let alone all the words everyone deserves (let's say it's to save trees, but the reality is that I'm not good at this). Some folks I met early and left, some came later, some I met only for a brief time frame. Some did a lot, and some just said a random sentence that opened me to a new perspective. Everyone, in one way or another, laid a stone to pave the way that got me here. For this, I thank you.



LIST OF PUBLICATIONS

5. *Remote-Entanglement Protocols for Stationary Qubits with Photonic Interfaces*
H.K.C. Beukers*, **M. Pasini***, H. Choi*, D. Englund, R. Hanson and J. Borregaard,
Phys. Rev. X Quantum 5, 010202 (2024),
4. *Nonlinear Quantum Photonics with a Tin-Vacancy Center Coupled to a One-Dimensional Diamond Waveguide*
M. Pasini, N. Codreanu, T. Turan, A. Riera Moral, C.F. Primavera, L. De Santis, H.K.C. Beukers, J.M. Brevoord, C. Waas, J. Borregaard and R. Hanson,
Preprint: arXiv:2311.12927 (2023),
3. *Heralded Initialization of Charge State and Optical Transition Frequency of Diamond Tin-Vacancy Centers*
J.M. Brevoord*, L. De Santis*, T. Yamamoto, **M. Pasini**, N. Codreanu, T. Turan, H.K.C. Beukers, C. Waas and R. Hanson,
Preprint: arXiv:2311.11962 (2023),
2. *Coherent Coupling of a Diamond Tin-Vacancy Center to a Tunable Open Microcavity*
Y. Herrmann*, J. Fischer*, J.M. Brevoord, C. Sauerzapf, L.G.C. Wienhoven, L.J. Feije, **M. Pasini**, M. Eschen, M. Ruf, M.J. Weaver and R. Hanson,
Preprint: arXiv:2311.08456 (2023),
1. *Bell Inequality Violation by Entangled Single Photon States Generated from a Laser, a LED or a Halogen Lamp*
M. Pasini, N. Leone, S. Mazzucchi, V. Moretti, D. Pastorello and L. Pavesi,
Phys. Rev. A 102, 063708 (2020).

*Equally contributing authors



Matteo Pasini

CURRICULUM VITAE

August 27th, 1994
Lugo (Ravenna)
Italy

2019 - 2024 **PhD in Physics**

QuTech, Delft University of Technology (The Netherlands)
Thesis: *Nanophotonics with Diamond Color Centers:
Quantum Optics and Entanglement Protocols*
Promotor: Prof. R. Hanson
Copromotor: Dr. C. Errando-Herranz

2018 - 2019 **Research Scholarship**

NanoLab, University of Trento (Italy)
Topic: Quantum Optics Experiments on Single Photon Entanglement
Advisor: Prof. L. Pavesi

2016 - 2018 **MSc in Experimental Physics**

University of Trento (Italy)
Thesis: *Experimental Test of Single Photon Entanglement*
Advisor: Prof. L. Pavesi

2013 - 2016 **BSc in Physics**

University of Bologna (Italy)
Thesis Advisor: Prof. M. Prevedelli

